UNIVERSITAT POLITÈCNICA DE VALÈNCIA

Escuela Politécnica Superior de Alcoy

ANALYSIS AND DESIGN OF A HUMAN POWERED VEHICLE

Trabajo Fin de Grado

Grado en Ingeniería Mecánica

AUTOR: Aarón Ramón Torrens

Tutor: Falk Klinge (Ostfalia Hochschule)

Cotutor: Miguel Ángel Sellés Cantó

CURSO ACADÉMICO: 2022-2023

Analysis and Design of a Human Powered Vehicle

Thesis, Fachhochschule Braunschweig/Wolfenbüttel, 15.11.2023

I.   Resumen

Desde principios del siglo XIX, en la industria del automóvil se han buscado estructuras más ligeras y diseños aerodinámicos mejorados para dar con un vehículo aerodinámicamente eficiente con un consumo energético y una estabilidad óptimos. Al principio, los prototipos presentaban perfiles cuadrados y de alta resistencia, lo que provocaba una mayor inestabilidad e ineficiencia del combustible. Por esta razón, para abordar estos desafíos, esta tesis presenta una investigación sobre el análisis aerodinámico de un chasis de vehículo de propulsión humana (HPV), cuyo objetivo principal es examinar la resistencia aerodinámica encontrada durante el viaje por carretera y posteriormente mejorar la eficiencia del vehículo a través de un rediseño del modelo anterior.

La metodología de investigación implica la realización de simulaciones y pruebas aerodinámicas utilizando software especializado para evaluar el rendimiento aerodinámico del chasis original. Luego, en base al análisis, se implementa un rediseño del chasis, incorporando modificaciones de diseño innovadoras para reducir la resistencia del aire mientras se mantiene la integridad estructural.

Palabras clave: Velomóvil; Industria automotriz; Vehículo; Aerodinámica; Eficiencia; Innovador; Rediseño; Análisis; CFD; CAD

II.   Abstract

Since the beginning of the 19th century, lighter structures and improved aerodynamic designs have been pursued in the automotive industry to stumble upon an aerodynamically efficient vehicle with optimal energy consumption and stability. At the beginning, prototypes featured just boxy, high-resistance profiles, resulting in increased instability and fuel inefficiency. For this reason, to address these challenges, this thesis presents an investigation into the aerodynamic analysis of a Human Powered Vehicle (HPV) chassis, whose primary objective is to examine the aerodynamic resistance encountered during road travel and subsequently enhance vehicle efficiency through a redesign of the previous model.

The research methodology involves conducting aerodynamic simulations and tests using specialised software to evaluate the aerodynamic performance of the original HPV chassis. Then, based on the analysis, a redesign of the chassis is implemented, incorporating innovative design modifications to reduce air resistance while maintaining structural integrity.

Keywords: Velomobile; Automotive Industry; Vehicle; Aerodynamics; Efficiency; Innovative; Redesign; Analysis; CFD; CAD

Contents

Contents

Contents

III.   Figures Index

Contents

Contents

Contents

IV.   Tables Index

V.   Acknowledgments

I am profoundly grateful to my mother and sister for their unwavering support, encouragement, and sacrifices throughout my academic journey. Their boundless love and understanding have been my pillars of strength, motivating me to persevere and excel in my endeavours.

To my girlfriend Raquel, your empathy, understanding, and unwavering belief in me have been a constant source of inspiration. Your support has made this academic pursuit not only a solo endeavour, but a shared journey filled with shared triumphs.

I extend my heartfelt appreciation to my friends for their camaraderie, laughter, and shared moments of stress and celebration. Your friendship has been a vital component of my academic experience, making the challenges more bearable and the successes more meaningful.

I would like to express my sincere gratitude to my professors at the Ostfalia Universität für angewandte Wissenschaften and at the Universitat Politècnica de Valencia for their guidance, expertise, and commitment to my academic excellence. Your mentorship and support have played a pivotal role in shaping my knowledge and skills, and I am fortunate to have had the opportunity to learn from such distinguished educators.

Last, but not least, I want to acknowledge myself for the dedication, perseverance and hard work invested in completing this Bachelor Thesis. This journey has been a test of my capabilities and endurance, and I am proud to have reached this milestone with determination and resilience.

To all those mentioned and many others who have contributed to my academic journey, thank you for being integral parts of this chapter of my life.

VI. Symbology and Abbreviations

Symbol	Meaning
P_W	Wheel Power
F_W	Wheel Force
v	Velocity
F_D	Drag Force
ρ	Density (air)
C_D	Drag Coefficient
A	Projected Area
Re	Reynolds Number
L	Characteristic Length
μ	Dynamic Viscosity
F_L	Lift Force
S	Projected Surface Area
C_L	Lift Coefficient
L/D	Lift to Drag Ratio
M	Mach Number
M^*	Maximum Airflow Mach Number
v_{max}/v %	Velocity Increment Percentage
HPV	Human Powered Vehicle
CAD	Computer Aided Design
CFD	Computer Fluid Dynamics
DRS	Drag Reduction System
LSR	Land Speed Record

1. Introduction

The improvement of the aerodynamics in a vehicle can increment the top speed as well as reduce the consumption overall, due to the decrease of the drag created by the vehicle. That's why aerodynamics is really important in the transport sector, since a more aerodynamic car or plane results in a more efficient driving either from a fuel consumption point of view or from a comfort point of view. For example, a small change in the rear of a trailer can become a significant fuel consumption reduction for a truck that is hours in service. In this example (Fig. 1.1 and Fig. 1.2), a Drag Reduction System (DRS) is being used to reduce the amount of Karman vortices on the tail of the vehicle. This helps decrease the drag resistance and at the same time improve the fuel efficiency.
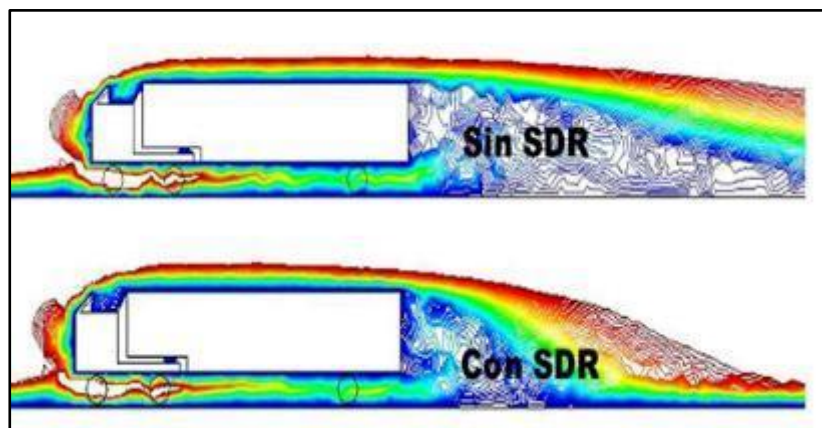
*Figure 3: **Drag Reduction System**: Flow Simulation of a lorry with DRS(bottom) and without a DRS(top) [ICIL].*

*Figure 2: **Drag Reduction System**: Lorry on road with DRS implemented [ICIL].*

In the case of an HPV as the Velo, a device like this cannot be added, but for this reason a research on the aerodynamics of it must be carried out. The study will have as its main objective to find the biggest flaws of the design, analyse them and then propose some useful changes that can improve the air drag and the drivability of the vehicle as well. There are many different types of driving resistances such as the rolling resistance or the climbing resistance, but these

are not as influential as the aerodynamic resistance once it comes to increasing the velocity or the drivability on a highway during hours. Since those are most of the time approximately the same on a normal drive due to the variables in their equations, and the aerodynamic drag increases the faster the vehicle travels, it is evident that the air drag will have a much bigger influence on the driving efficiency than other driving resistances.

In a Human Powered Vehicle, it is essential to keep the driving resistances as low as possible, because it doesn't have an engine to power the vehicle until the fuel tank is empty. Instead, a person pedals with its own energy and force against the mentioned resistances. The Velo in question already has an enhanced torque transmission and a lightweight chassis, apart from the general aerodynamic lines. However, the design is optimised for front-wind, leaving other possible situations like side-wind aside. Even though the front-wind is in general the situation the Velo will encounter the most, the side-wind is the one that makes the vehicle more unstable and hinder the drivability of it.

Furthermore, there are several aspects, other than the energy consumption or the drivability, that the aerodynamics of a vehicle influence. The top speed is one of them, being the air drag directly connected to the maximal speed achievable, since the faster the vehicle travels, the higher is the drag force exerted on the vehicle (Fig. 1.3). Until today, the Velo has reached a top speed of 100 km/h on the plain, but since the simplified formula for the wheel power is (considering the air drag as the only resistance force):

$$P_W = F_W \cdot v ; \qquad\qquad (1.1.)$$

where F_R is the wheel force and v the driving velocity. Neglecting the other driving resistances such as the roll resistance, the wheel force is equal to the aerodynamic drag force:

$$F_D = \frac{1}{2} \cdot \rho \cdot C_D \cdot A \cdot v^2; \qquad\qquad (1.2.)$$
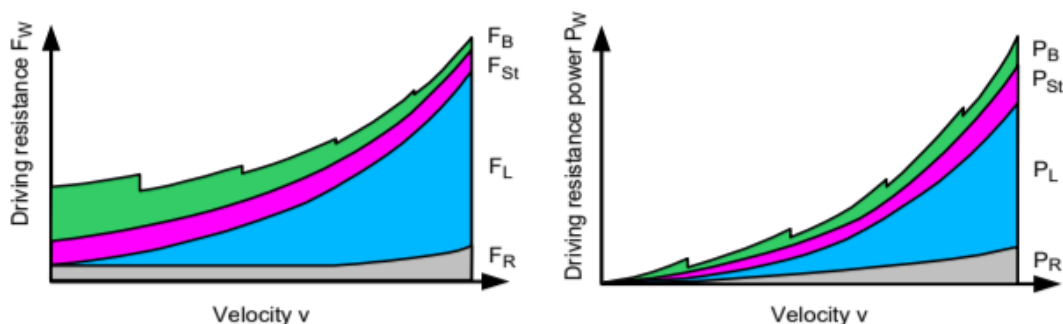
*Figure 4: **Driving Resistances**: Comparison of the Driving Resistances in a vehicle: Acceleration, Slope, Air and Rolling Resistance [Dor22].*

Therefore, the velocity is the most influential variable in the equation, and to increase 1 km/h starting from the 100 km/h (top speed achieved until now) requires at least 3% more power every time it accelerates one unit. The only way of dropping the amount of energy loss is by smoothing the vehicle form and reducing the repercussions of the drag such as the vortices at the tail of the vehicle.

2. Problem definition and objective

2.1 Problem definition

Until today, the fastest terrestrial HPV world record is held by a Canadian organisation named *Aerovelo* with a front drive Streamlined Supine Bicycle, and this vehicle reached the top speed of 144.17 km/h on a 200 m road. This makes the actual top speed of the Velo to be 44.17 km/h away from being the fastest in the world, which is a big difference to surpass. As mentioned before, aerodynamics is a big barrier to exceed its own top speed record, and that is why the main problem to solve is going to be the aerodynamic design of the chassis.

On the other hand, it is necessary to improve the lateral aerodynamics of the Velo to secure the stability of it during the ride in case of transversal wind, because that could lead to a bad handle and therefore to an inefficient driving.

2.2 Objective

The main objective of this project is to carry out an aerodynamic analysis of the Ostfalia Velo Racing Team Human Powered Vehicle to find the main parts where the drag has a potential influence on the aerodynamic efficiency. Due to the great importance of the vehicle aerodynamics on the road, it is essential to perform this type of analysis every time a design of a vehicle is made, since one of the biggest sources of energy waste in transport, whatever it is its power source, it's the drag. In this case, the major drag is provoked by the pass through the air, which through pressure drag or viscous drag (among other types of drag) makes the vehicle lose its energy.

With the Ansys Fluent software, the chassis will be analysed at 60 km/h, 100 km/h and also 130 km/h with front-wind, side-wind and wind coming with an angle of 22.5º and 45º from the diagonal. This program will show how the wind behaves when passing through the HPV and therefore help identify the main problems to be solved. From the results obtained, pressure and velocity diagrams can be examined to look for the physical reason behind the problem, and then get conclusions and some possible solutions to these problems. Then, the solutions found will be compared to the design characteristics of the *Aerovelo* to see the differences between the competitors and the Velo Racing Team design, so that further improvements can be made in the future.

3.   State of the art

3.1 History of aerodynamics in ground vehicles

Human Powered Vehicles are a type of vehicles powered by human means, but despite this difference with the normal automobiles, the aerodynamic theory still applies to them. Therefore, to be aware of where HPVs come from, it is necessary to review the automobile history and its aerodynamic advances, as well as the beginnings of the Velomobile.

3.1.1 History of aerodynamics in cars

Due to the influence of the aeronautical industry, most of the automobiles were designed replicating the form of a plane or a water drop, being the latter the common denominator in every design from the early 19s. The main objective of some prototypes like the *La Jamais Contente* (Fig. 3.1) or the *Stanley Steamer Rocket (Fig. 3.2),* which again resembled elongated water droplets with four wheels, was to copy nature in a way that the end result of the experiment was profitable, so they could break the Land Speed Record (LSR) [Nie13]. However, they still ignored most of the important principles of the aerodynamics of a car. On one hand, the wheels were on the outside and not hidden in the chassis, as later on would occur with the spats that reduced to some extent the drag created by the wheels.

On the other side, they were also so tall and let so much airflow under the car, that it made those vehicles incredibly unsteady. A lot of characteristics were still imperfect, and in the following decades the ambition to design the fastest car originated a craze where companies competed against each other, patenting prototypes and investigating thoroughly the physics behind these phenomena.

*Figure 5: **Stanley Steamer Rocket (1906)**: Prototype of the* Stanley Steamer Rocket.

*Figure 6: **La Jamais Contente (1899)**: Prototype of* La Jamais Contente *car.*

The implementation of the wind tunnels in the analysis of the Drag Coefficient of the cars, improved to a large extent the capability the companies had to gather information from the tests they carried out. This supposed a big leap for the industry and on the market started to appear more adventurous models, where the projected frontal section was reduced to a minimum, and the car was practically scraping against the road.

3. State of the Art
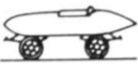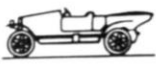
*Figure 7: **Evolution of Car Design**: Evolution of the car desigs over time in the 20th century [Huc87].*

Overall, the history of automobile aerodynamics can be divided into four different phases (Fig. 3.3): Basic shapes, streamlined cars, detail optimisation and shape optimisation.

As already told, at the beginning of the century the shapes of the car concepts were extremely clumsy and ill-designed. It wasn't until the 1921 that started appearing more streamlined designs, which were tested out in wind tunnels, coast-down tests or by measuring the top speed. Although, the latter two methods led to uncountable errors due to the inaccuracy of the process. One prominent example is the 1934 Chrysler Airflow, which introduced a streamlined body design to reduce drag. Despite its innovative features, the Airflow faced initial resistance due to its unconventional appearance. Nevertheless, it laid the foundation for subsequent aerodynamic advancements in the automotive industry.

3.1.2 History of aerodynamics in Velomobiles

The evolution of velomobiles and their aerodynamic design can be traced back to the early 20th century, with significant advancements occurring over the decades. This historical analysis explores key milestones in the development of velomobile aerodynamics, highlighting major breakthroughs and their impact on the design and performance of these human-powered vehicles. The concept of utilising streamlined enclosures for human-powered vehicles can be

traced back to the 1930s, when the French engineer Charles Mochet introduced the *Velocar* (Fig. 3.4), a low-profile vehicle with a recumbent seating position and an aerodynamic shell.

This early example laid the foundation for the development of velomobiles, inspiring subsequent innovations [Kal18].

*Figure 8: **Charles Mochet Velocar** (**1945**): Velocar from the French engineer Charles Mochet [Kal18].*

Nonetheless, following World War II, velomobile aerodynamics took a backseat as the focus shifted towards automobile development. However, this period witnessed significant advancements in bicycle design, including the introduction of lightweight materials and improved components. These innovations indirectly influenced velomobile development, as lighter bicycles allowed for greater speeds and manoeuvrability.

In the 1980s, velomobiles experienced a resurgence, driven by a renewed interest in human-powered transportation and alternative mobility solutions. Thus, innovations in materials, such as the increased use of fibreglass and carbon fibre composites, played a crucial role in reducing weight and enhancing the aerodynamic efficiency of velomobiles. During this period, velomobile designers began incorporating fully enclosed fairings and streamlined shapes. On the other hand, the adoption of teardrop profiles inspired by aviation and automotive design principles became prevalent, since these shapes minimised air resistance, allowing velomobiles to achieve higher speeds with the same amount of human power.

Furthermore, wheel fairings played a crucial role in minimising drag by reducing turbulence caused by rotating wheels. Historically, velomobiles have employed partial or fully enclosed wheel fairings, covering both on front and rear wheels. These fairings smooth out the airflow around the wheels, minimising drag and improving overall aerodynamic efficiency.

3.2 Technical knowledge

Every vehicle accelerating to high velocities is affected by significant aerodynamic forces which will influence the final design of it depending on the distinct final purposes it has. For instance, one of the most known aerodynamic forces in automobiles is the ground force, originated by the

3.2.1 Bernoulli

The Bernoulli effect is based on Bernoulli's principle, which states that as the speed of a fluid (such as air) increases, its pressure decreases. This principle can be applied to the airflow around a velomobile and helps explain the forces at play.

3. State of the Art
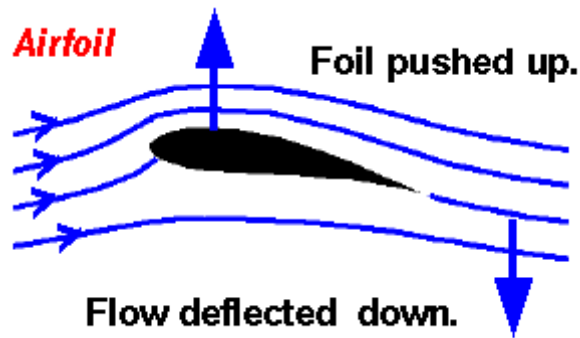
*Figure 9: **Airfoil with streamlines**: Visual representation of forces actuating on an airfoil [NASA]*

When a velomobile is in motion, airflows around its streamlined body and the air passing over the top of the body encounters a longer distance to travel compared to the air passing underneath (Fig. 3.5). According to Bernoulli's principle, the air over the top of the velomobile, which is forced to travel a longer distance at the same time as the flow from under the vehicle, accelerates and its pressure decreases.

At once, the air passing underneath the velomobile moves at a relatively slower speed and exerts a higher pressure. This pressure difference between the top and bottom surfaces of the velomobile body creates an upward lift force, which helps to counteract the weight of the velomobile and reduces the rolling resistance, allowing for greater speed and efficiency.

Additionally, the Bernoulli effect also influences the airflow around the wheels of a velomobile, given the fact that when the wheels rotate, they create regions of high and low pressure due to the acceleration and deceleration of the surrounding air. Consequently, this pressure difference contributes to the overall aerodynamic forces acting on the velomobile.

It is important to note that the Bernoulli effect is just one aspect of the aerodynamics of velomobiles. Other factors such as vehicle shape, frontal area, and the interaction of airflow with the rider (among others) also play an important role. Designing a velomobile to take advantage of the Bernoulli effect involves careful consideration of the body shape, angle of attack, and overall aerodynamic profile to maximise the lift force and minimise drag, having in
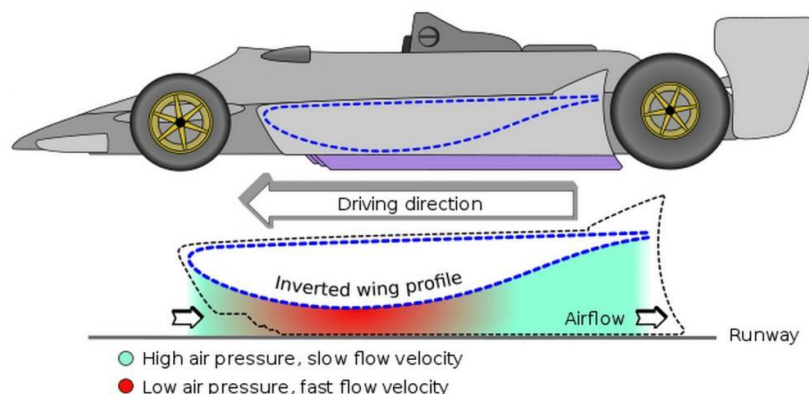
*Figure 10: **Formula 1 wing profile view**: Profile view of the Bernoulli phenomenon at the wing of a Formula 1 (Venturi Tube).*

mind also that a minimum of down force is essential to keep the transmission of the torque from the wheels to the road [Kat96]. By understanding and utilising the Bernoulli effect, velomobile aerodynamic designs can be optimised, allowing for improved speed, efficiency, and overall

performance. In most of the Formula 1 cars, like the one in Figure 3.6, an applied concept of the Bernoulli effect is used by implementing a Venturi tube adapted to the aerodynamic line of the vehicle.

A Venturi tube is a device that consists of a tapered tube with a narrow throat in the middle, which allows fluid to flow through the tube, increasing its velocity as it passes through the narrow section, and then decreasing it as it widens out again. As shown in the image above, the Bernoulli effect can be used to maximise both speed and downforce, at the same time, without adding up much weight to the vehicle.

3.2.2 Ground Effect

The ground effect refers to the phenomenon in aerodynamics where a vehicle experiences increased lift (or downforce) and reduced drag when it is travelling close to the ground or any other surface. In the context of cars, ground effect is used to improve performance and stability, for instance; sport cars and racing cars often incorporate ground effect principles into their design by utilising underbody aerodynamics, side skirts, and diffusers, which are designed to manage the airflow beneath the car, creating a low-pressure zone and effectively pulling the vehicle down towards the ground [Kat96].

By optimising the ground effect, cars can achieve better stability at high speeds, increased traction, and improved cornering capabilities. The ground effect allows the vehicle to maintain better contact with the road surface, enhancing handling and reducing the risk of losing control. Nonetheless, ground effect can be a double-edged sword in some cases if the downforce exerted leads to a loss of speed and reduced acceleration.

3.2.3 Reynolds Number (Re)

The Reynolds Number is a dimensionless parameter, named after Osborne Reynolds, used to characterise the flow of a fluid, such as air, around an object or through a conduit. The Reynolds Number helps determine the type of flow (laminar or turbulent) and provides valuable information about the aerodynamics of a vehicle.

The Reynolds Number (Re) is defined as the ratio of inertial forces to viscous forces in a fluid flow. Mathematically, it is expressed as:

$$Re = \frac{\rho \cdot v \cdot L}{\mu} \tag{3.1.}$$

Where Re is the Reynolds Number, ρ is the density of the fluid, v is the velocity of the fluid relative to the object, L is a characteristic length of the object (i.e., diameter for a pipe, chord length for an airfoil) and μ is the dynamic viscosity of the fluid.

3. State of the Art

Now, depending on the value of the Reynolds Number, different flow types can be observed [Hoe65] (Fig. 3.7):
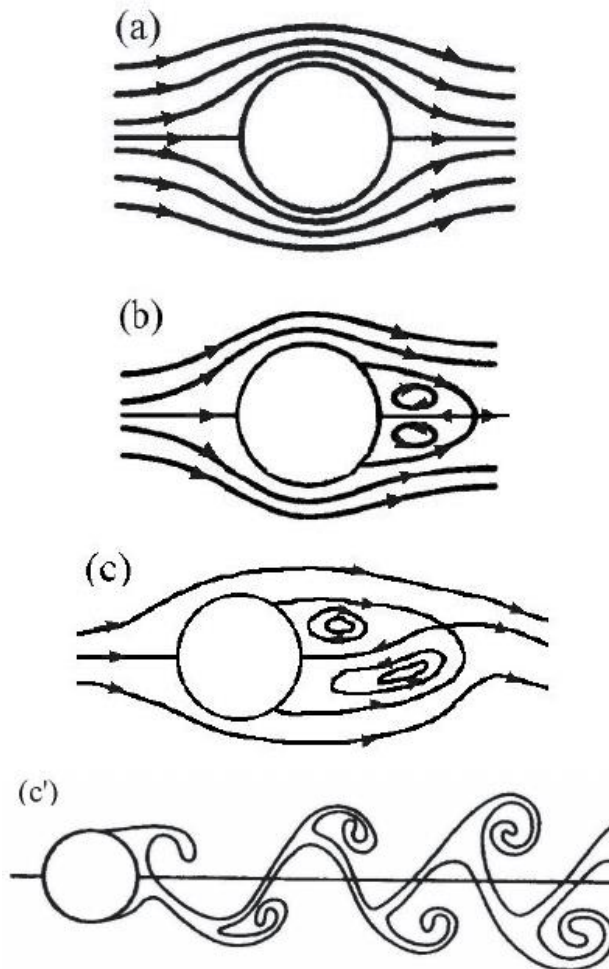
*Figure 11: **Reynolds Number Flow Types**: Different flow types around a sphere depending on the Reynolds Number range.*

1. Laminar Flow (a): This occurs at low Reynolds Number values when the flow is smooth, well-ordered, and exhibits straight, parallel streamlines. It is characterised by low turbulence and little mixing between fluid layers. Laminar flow is generally observed below a Reynolds Number of about 2300.
2. Transitional Flow (b, c): As the Reynolds Number increases, the flow can transition from laminar to turbulent. In this transitional region ($2300 < Re < 4000$), the flow behaviour can be a combination of laminar and turbulent characteristics.
3. Turbulent Flow (d): At high Reynolds Numbers, the flow becomes turbulent, which is chaotic and characterised by irregular fluid motion, vortices, and mixing between fluid layers. It exhibits higher energy losses due to increased friction drag and is typically observed above a Reynolds Number of around 4,000.

The influence of the Reynolds Number on the aerodynamics of a vehicle is significant, affecting various aspects, such as:

1. Drag: At low Reynolds Numbers, the flow tends to be laminar, resulting in lower skin friction drag. Nonetheless, at higher Reynolds Numbers the flow becomes turbulent,

leading to increased form drag. Therefore, the aerodynamic design of a vehicle must consider the expected Reynolds Number to optimise its shape and minimise drag.

2. <u>Boundary Layer</u>: The Reynolds Number affects the thickness and behaviour of the boundary layer, which is the thin layer of fluid adjacent to the surface of the object. At low Reynolds Numbers, the boundary layer remains thin and laminar, but as the Reynolds Number increases, the boundary layer can transition to turbulent flow, becoming thicker and altering the flow characteristics.

3. <u>Separation and Lift</u>: The Reynolds Number influences the flow separation behaviour and lift generation of an airfoil or wing. At low Reynolds Numbers, laminar flow separation can occur earlier, reducing lift and potentially causing stall (in aeroplanes). Higher Reynolds Numbers promote delayed separation, allowing for increased lift generation and better overall aerodynamic performance.

Overall, the Reynolds Number is a crucial parameter for understanding and analysing fluid flow characteristics and their impact on vehicle aerodynamics. It helps determine flow types (laminar, transitional, or turbulent) and guides the design process to optimise aerodynamic performance based on the expected Reynolds Number.

3.2.4 Drag Force (F_D)

Aerodynamic drag refers to the resistance encountered by an object moving through a fluid, typically air, due to the interaction between the object's shape and the surrounding fluid. It is a force that acts opposite to the direction of motion and can significantly affect the performance and energy efficiency of various objects, such as vehicles, aircraft, and sports equipment.

There are several types of drag that contribute to the overall aerodynamic drag experienced by an object [Hoe65]:

1. <u>Form Drag (Pressure Drag)</u>: Form drag arises from the pressure difference between the front and rear surfaces of the object. When the fluid flows around the object, it exerts a higher pressure on the front surface and a lower pressure on the rear surface. This pressure difference creates a resistance force that opposes the object's motion. The next equation represents the drag force for a certain drag coefficient:

$$F_D = \frac{1}{2} \cdot \rho \cdot C_D \cdot A \cdot v^2 \qquad (3.2.)$$

Where ρ is the density of the fluid (namely, air), C_d the drag coefficient, A the projected frontal area and v the velocity of the body.

2. <u>Skin Friction Drag</u>: Skin friction drag is caused by the frictional resistance between the fluid and the object's surface within the boundary layer. As the fluid flows over the object's surface, it experiences shear stress due to the viscosity of the fluid. This shear stress leads to drag force along the surface, which adds up to the overall drag.

3. <u>Lift-Induced Drag</u>: Lift-induced drag occurs when an object generates lift, such as an aircraft wing, and is accompanied by a drag force that acts perpendicular to the lift force. This drag component is a result of the production of vortices and the creation of downwash, which increases the overall drag experienced by the object.

3. State of the Art

(A) FLOW PATTERN OF CIRCULAR CYLINDER IN NON-VISCOUS FLOW; NO DRAG. (D) PLATE WITH "SPLITTER" DEVICE IN WAKE; C_{D_o} = 1.6.

(B) CYLINDER AT REYNOLDS NUMBERS IN THE ORDER OF 40; $C_{D_o} \approx$ 1.2. (E) CYLINDER ABOVE CRITICAL REYNOLDS NUMBER WITH C_{D_o} = 0.3.

(C) CYLINDER BETWEEN R_d = 10^4 and 10^5; VORTEX STREET WITH C_{D_o} = 1.2 (F) STREAMLINE SECTION WITH C_{D_o} IN THE ORDER OF 0.06.
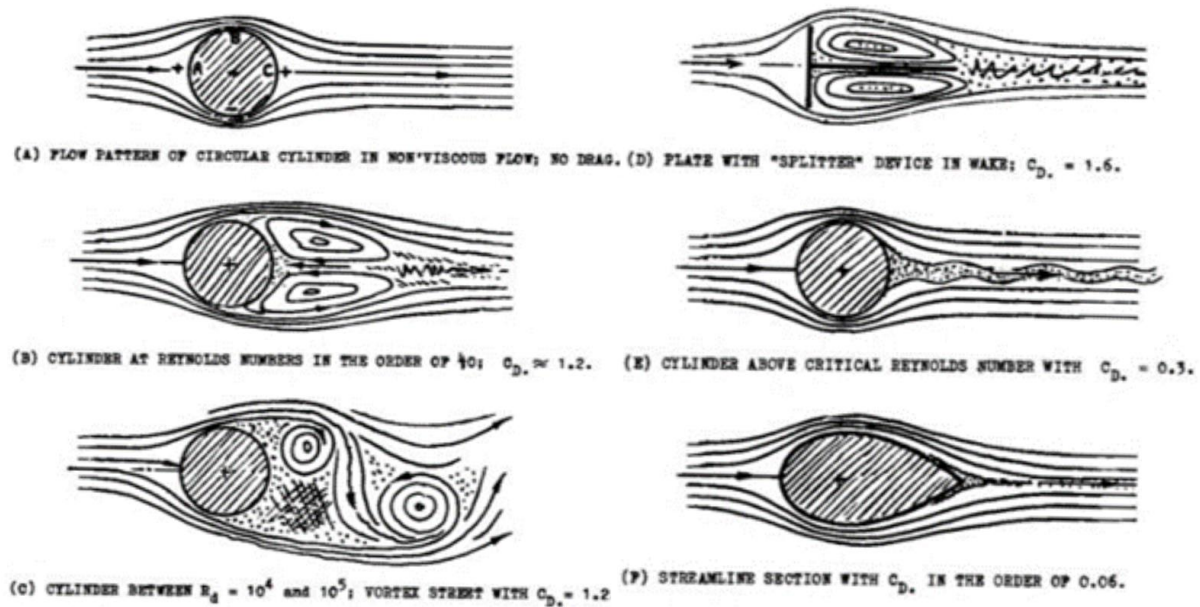
*Figure 12: **Drag Coefficient Effects**: Effects of different shapes on the Drag Coefficient and the wake originated [Hoe65].*

4. <u>Interference Drag</u>: Interference drag appears when two or more objects interact in a flow field. The presence of one object can disturb the flow around another object, leading to increased drag for both objects. This type of drag is particularly significant in multi-component systems like vehicles with exposed wheels or aircraft with external stores.

5. <u>Wave Drag</u>: Wave drag occurs when an object moves at high speeds, close to or above the speed of sound. At these speeds, shock waves are generated due to the compression of the fluid, resulting in a sudden increase in drag. This type of drag is prominent in supersonic and hypersonic flows.

When an object moves through a fluid, it needs to overcome the drag force, requiring an expenditure of energy. This power required to overcome drag is proportional to the cube of the object's velocity (P $\propto v^3$), according to the power equation seen in the introduction. Therefore, increasing the velocity results in a significant increase in energy loss due to the higher power requirement to overcome the drag. Thus, reducing aerodynamic drag is crucial for improving energy efficiency.

By designing objects with streamlined shapes, minimising surface roughness, and optimising flow patterns, the drag can be reduced, allowing for lower energy consumption and improved performance, particularly in transportation systems where energy efficiency is a key consideration.

In the image above (Fig. 3.8), the effect on the wake of the object is caused by the difference between distinct body forms and its consequent drag coefficient. Depending on the Reynolds Number and the form of the object, a different type of flow (laminar, transitional or turbulent) can be found at the wake of the object. With the implementation of more streamlined designs, the drag coefficient (C_D) can be reduced enormously, improving the overall performance.

3.2.5 Lift Force (F_L)

The lift force is a physical phenomenon that occurs when an object moves through a fluid medium, such as air or water. It is defined as the force that acts perpendicular to the direction of the object's motion, and it is responsible for keeping the object in the air or afloat in the water. This force is generated by the pressure difference between the top and bottom surfaces of the object (*Bernoulli effect*) when the fluid is forced to flow around it, creating areas of high and low pressure. The pressure on the top surface of the object is lower than that on the bottom surface, which creates a perpendicular net force in the upward direction. This can be calculated using the following equation:

$$F_L = \frac{1}{2} \cdot \rho \cdot S \cdot C_L \cdot v^2 \qquad\qquad (3.3.)$$

where L is the lift force, ρ is the density of the fluid, S is the surface area of the object, Cl is the lift coefficient, and v is the velocity of the object relative to the fluid.

The lift force is closely related to drag, which is also generated by the pressure difference between the front and rear surfaces of the object, but it acts in the opposite direction to the lift force.

In the context of vehicles, such as planes or cars, the lift force is crucial for their operation. For instance, in a plane the wings are designed to generate lift to keep the plane in the air, which must be greater than the weight of the plane to achieve lift-off and maintain a stable flight. The design of the wings, including their shape, size, and orientation, is optimised to achieve the required lift force while minimising drag. In cars, the lift force is less significant, but it can still play a role in reducing drag and improving fuel efficiency by using aerodynamic features such as spoilers or diffusers to manipulate the flow of air around the car and generate lift or reduce drag as needed to improve the performance.

3.2.6 Boundary Layer

The boundary layer is a thin layer of fluid that forms on the surface of an object as it moves through a fluid medium, such as air or water. It is characterised by a gradual transition of the flow velocity from zero at the surface of the object to the free-stream velocity of the fluid away from the surface (Fig. 3.9).

The boundary layer plays a crucial role in determining the drag experienced by the object, as it significantly influences the drag through two main mechanisms already mentioned in the Drag Force section: skin friction drag and pressure drag.

On the other hand, the characteristics of the boundary layer and its effect on drag are influenced by the Reynolds Number, which determines the type of flow within the boundary layer (laminar or turbulent). At low Reynolds Numbers, the flow tends to be laminar, characterised by smooth and organised layers of fluid. In laminar flow, the boundary layer is thin and remains attached to the object's surface. However, as the Reynolds Number increases, the flow becomes more turbulent, with chaotic and irregular fluid motion. Turbulent flow creates a thicker boundary layer and is associated with higher skin friction drag but potentially lower pressure drag compared to laminar flow.

3. State of the Art

Turbulent flow in the boundary layer offers advantages that include reduced skin friction drag, increased heat and mass transfer, and delayed boundary layer separation. This type of flow exhibits a higher level of fluid mixing, leading to decreased contact area between the fluid and the object's surface. The resulting turbulent vortices disrupt the smooth flow and contribute to lower drag forces. Additionally, the enhanced mixing within the boundary layer enables more efficient heat exchange and facilitates faster diffusion and transport of mass, making it beneficial for chemical reactions or mass transfer processes.

Moreover, turbulent flow shows greater resistance to boundary layer separation compared to laminar flow. The chaotic motion of turbulent vortices forces the flow to attach further to the surface, preventing early separation of the boundary layer from the object's surface, and maintaining lift on airfoils and reducing drag on vehicles, thus enhancing overall aerodynamic performance.

However, there are also disadvantages associated with turbulent flow in the boundary layer. One such drawback is the higher pressure drag compared to laminar flow. The irregular and fluctuating motion leads to increased pressure fluctuations and greater energy losses. This higher pressure drag can be problematic in applications where minimising drag is crucial, such as in vehicles or aerodynamic designs.
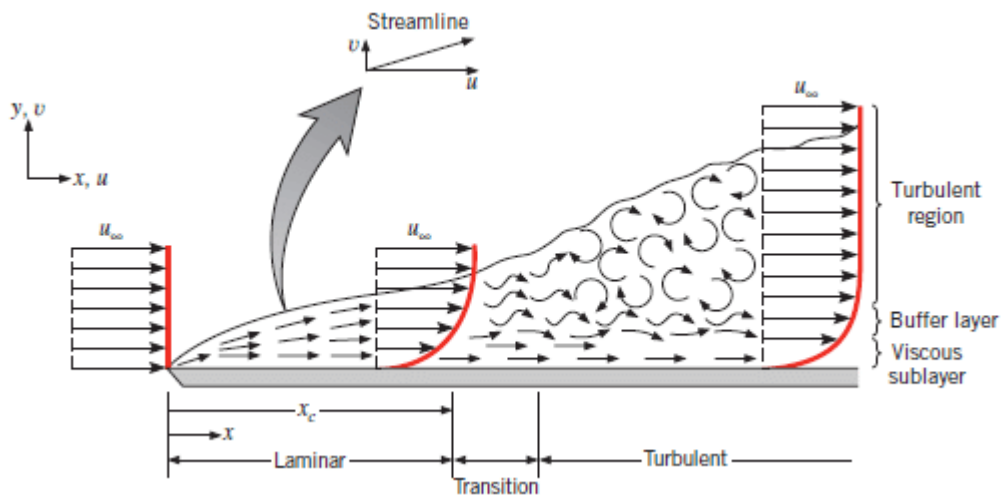
Figure 13: ***Boundary Layer States****: Transition of the states of the Boundary Layer from Laminar to Turbulent.*

Furthermore, turbulent flow requires more energy to maintain than laminar flow, since the chaotic nature of turbulent motion results in increased fluid mixing and greater energy dissipation within the boundary layer. Additionally, turbulent flow in the boundary layer presents great sensitivity to surface roughness effects (irregularities or roughness on the object's surface), which can amplify turbulence and disrupt the flow behaviour, leading to increased drag. In turbulent flow situations, maintaining a smooth surface design becomes crucial to minimise the impact of surface roughness and optimise overall performance.

3.2.7 Aerodynamic Efficiency

Aerodynamic efficiency refers to the ability of an object to minimise drag while generating lift or achieving forward motion. It represents the effectiveness of an object's design in reducing the resistance encountered during its movement through a fluid, namely air. The primary goal

3.   State of the Art

of aerodynamic efficiency is to maximise the ratio of lift to drag, as this indicates how effectively the object can generate lift while minimising the resistance it encounters.

The lift-to-drag ratio (L/D ratio) is a dimensionless quantity that compares the magnitude of the lift force to the drag force experienced by an object. It quantifies the efficiency of an object's aerodynamic design by expressing the amount of lift generated relative to the drag it creates. A higher L/D ratio indicates a more efficient design, as it means that the object can generate a greater amount of lift while experiencing minimal drag.

$$\frac{L}{D} = \frac{F_L}{F_D} = \frac{C_L}{C_D}$$

(3.4.)

3.2.8 Mach Number (M)

The Mach Number is a dimensionless value named after Ernst Mach, just like the Reynolds Number, used to describe the speed of an object in relation with the speed of sound of the same medium (343 m/s). The formula for the Mach Number is as follows:

$$M = \frac{v}{c}$$

(3.5.)

being M the Mach Number, v the object velocity and c the sound velocity of the medium.

4. CFD analysis of the previous Velomobile model

The aerodynamic analysis of the vehicle was undertaken with the Ansys Fluent extension, which allowed to simulate the airflow and the plotting of useful charts for the subsequent diagnostics.

Additionally, the utilisation of the Fluent k-omega GEKO model over the previously used Spalart-Allmaras model was motivated by its superior ability to capture complex turbulent flow phenomena more accurately [Szu22]. The k-omega GEKO model leverages the advantages of combining the two equations, k-omega and the k-epsilon turbulence models, offering enhanced predictions for a wide range of turbulent flows. It exhibits better performance in regions of adverse pressure gradients and separated flow, making it well-suited for aerodynamic analysis in cases where flow separation and complex boundary layer behaviours are prevalent [San22]. The transition to the k-omega GEKO model promises improved fidelity and reliability in capturing intricate flow patterns and boundary layer dynamics of velomobile analysis. However, this model is also dependant on the experimental data extracted to tune the values used for the equations. That's why in the following analysis the principal values to modify the behaviour of the results were $C_{SEP} = 1,75$, $C_{NW} = 0,5$ and $C_{JET} = 0,9$, since it can be later compared with the wind tunnel values and be better adapted in another Thesis. For the aerodynamic analysis of the redesigned Velomobile, the use of Spalart-Allmaras will be more adequate, given the fact that the mode has not been built yet.

Case	Angle	Velocity Range [km/h]	Projected Area [m^2]
Front	0º	60-100-130	0,3272
Diagonal	22.5º	171,57	0,7046
Diagonal	45º	161,82	1,1920
Side	90º	16-30-45	1,6128

*Table 4.1:**Analysis's Initial Conditions**: Initial Conditions set for the CFD Analysis*

On the other hand, for the software to be able to process the Velo's contour in an environment (Fig. 4.1), a mesh was generated with the following general configuration:

Therefore, the following fluid domain and mesh distribution were chosen for the trials (front-wind, side-wind and diagonal-wind). For the three cases, the considerations of the Table 4.1 were taken.

Due to the amount of calculus necessary to analyse the whole model, only the half of it was completely analysed during the front-wind analysis (Fig. 4.2), in order to reduce the computational effort and rendering time. Furthermore, for the other analyses, the chosen enclosure measures were specific for every one of them, and can be seen in the *SpaceClaim* geometry preparation files attached to the researched conducted [Tor23]. In the case of the front-wind analysis, the Average Orthogonal Quality of the mesh was 0,9338 and the Minimum Orthogonal Quality was 0,2432, staying above the acceptable minimum of 0,1 (Ansys12). In this research, the lowest Minimum Orthogonal Quality was 0,13, coming from the diagonal-wind analysis. However, even this result was above the minimum acceptable value.

4. CFD Analysis of Previous Model

Regarding the simulation configuration, given the fact that the environment conditions do not change, the fixed parameters for both tests were as follows:

$$\text{Temperature: } T = 288,16 \; K$$

$$\text{Pressure: } p = 101325 \; Pa$$

$$\text{Density: } \rho = 1,225 \frac{kg}{m^3}$$

$$\text{Dynamic viscosity: } \mu = 1,7894 * 10^{-5} \frac{kg}{m \cdot s}$$
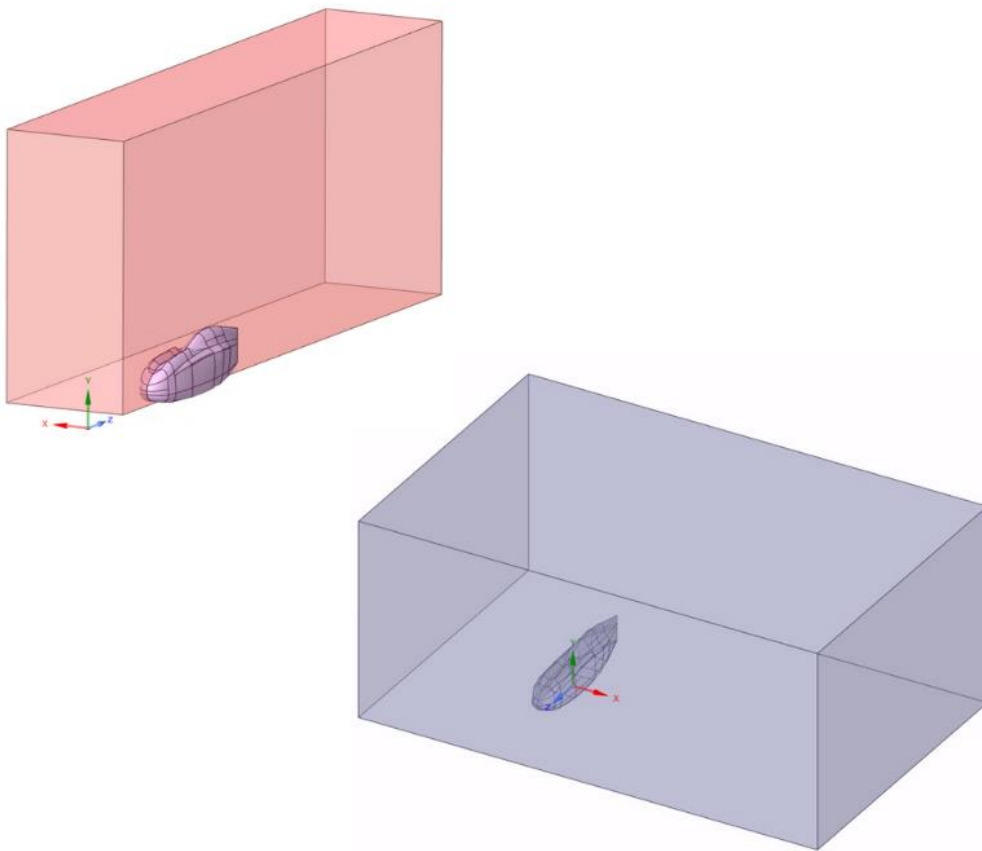
Figure 15: **Fluid Domains**: Fluid Domains designed for the front-wind (top) and for the side- & diagonal-wind (bottom).
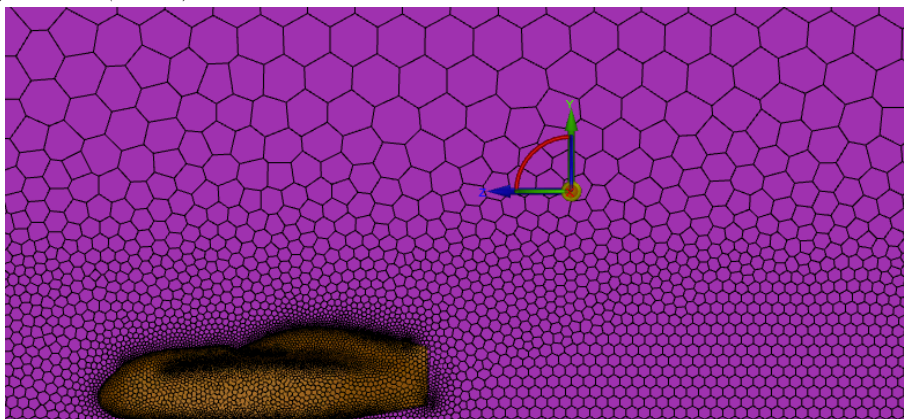
Figure 14: **Front-wind Mesh**: Mesh generated for the front-wind analysis.

4. CFD Analysis of Previous Model

4.1 Front-wind analysis

In this chapter, the front-wind analysis results at three different speeds (Table 4.2) are shown:

Cases	m/s	km/h	M
v_1	16,67	60	0,0486
v_2	27,77	100	0,0810
v_3	36,11	130	0,1053

*Table 4.2: **Velocities and Mach Number**: Set of velocities and Mach Number for the first-wind analysis.*

Due to the fact that the previous version of the Velomobile was optimised mainly for front-wind performance, the charts exposed aren't showing noticeable alarming results, but more discrete outcomes. For this reason, these results were the main point of discussion in this first part.

4.1.1 Analysis outcomes

Velocity

The most basic plot is usually the velocity magnitude, where the changes in the velocity over the length of the vehicle can be seen, and the consequences of the shape of it affect the manoeuvrability of the Velomobile. In this case, as shown in the Figure 4.3, for the worst case scenario the initial or entry velocity of the airflow is 36,11 m/s (130 km/h), which climbs to a maximum velocity of 49,02 m/s (176,47 km/h), being this an increment of 135% in the airflow speed.
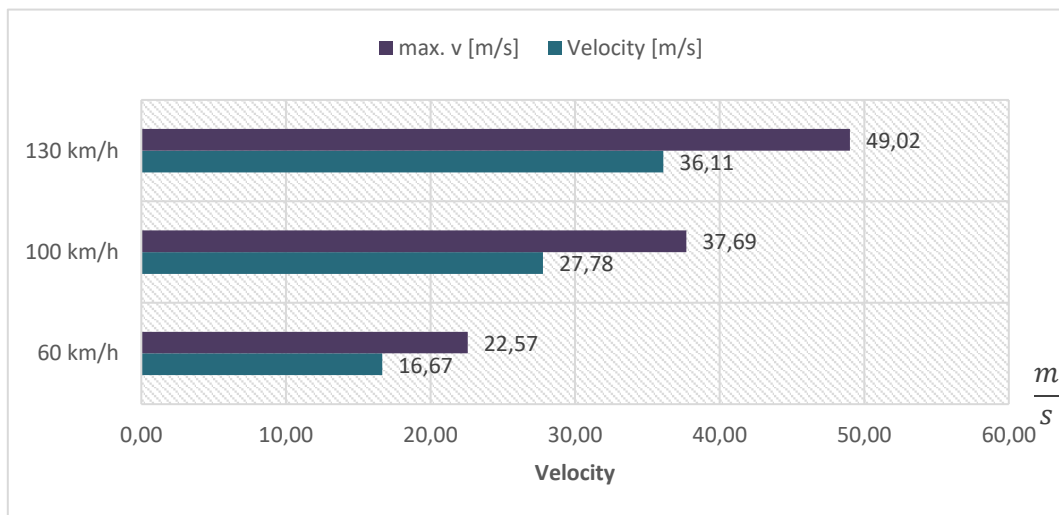
*Figure 16: **Initial and Maximum Velocity**: Comparison between the initial (blue) and the maximum velocities (purple) for the three initial velocities in the front-wind analysis.*

4. CFD Analysis of Previous Model

On the other hand, the speed difference is recurrent and the other two speed samples also have an increase of the 135%. Below, the images illustrate the zones where these maximum speeds take place. Analysing the Figure 4.4, it can be seen that the main reason why the air is slowing down at the nose is because the air molecules encounter the fairing, and the velocity with which the Velomobile moves, comprises the air molecules reducing the flow speed.
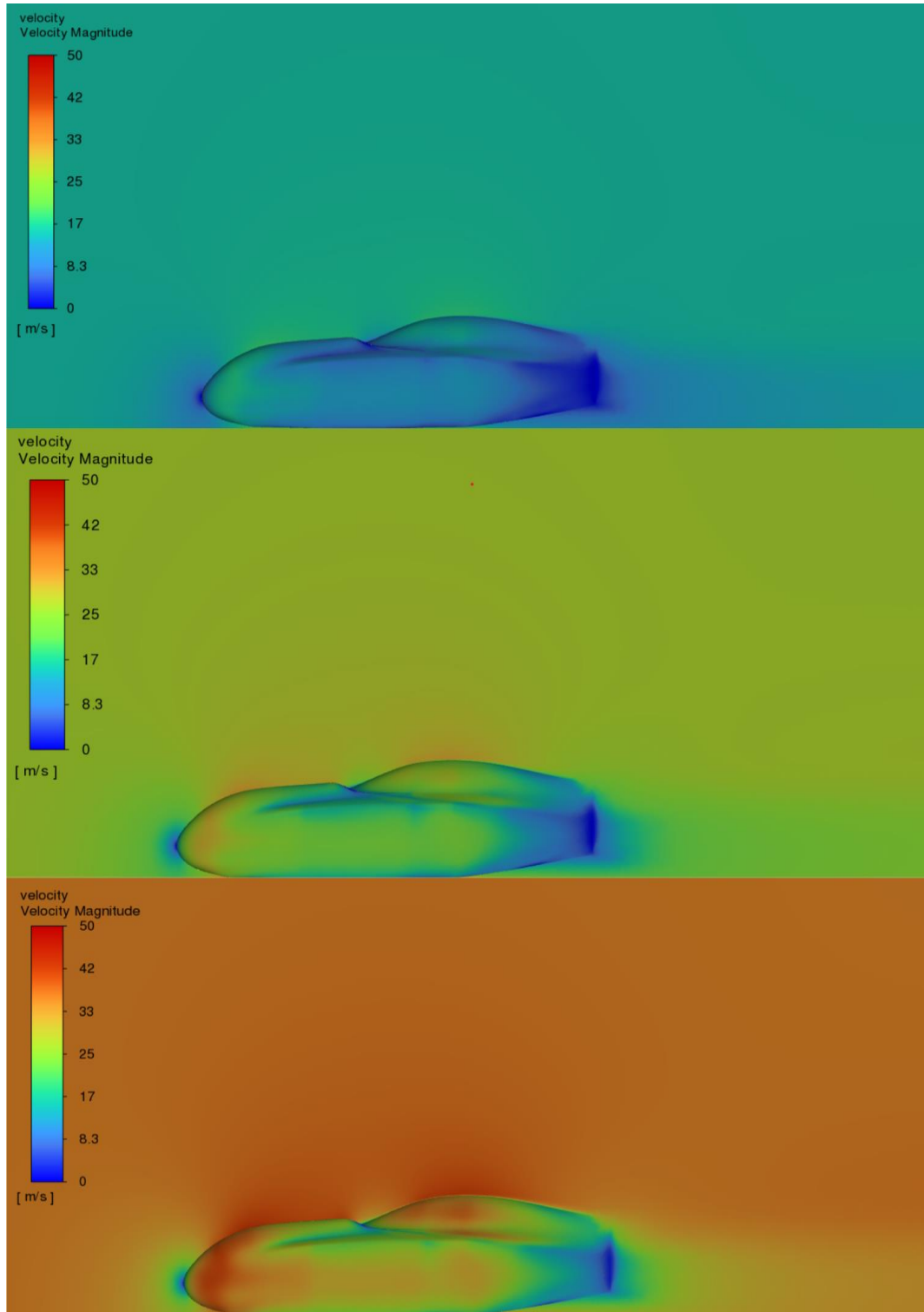
*Figure 17: **Front-wind analysis velocity Contours**: Velocity comparison between the three cases of the front-wind anlaysis with normalised values: 60 km/h (top), 100 km/h (middle) and 130 km/h (bottom).*

4. CFD Analysis of Previous Model

However, as the flow passes through the body, due to the skin friction drag, the velocity decreases until the boundary layer detaches from the chassis, as explained in the *Boundary layer* chapter. At the tail, the flow mixes itself with the eddies formed in the wake and that provokes a deceleration of the air, which at the same time also decelerate the vehicle.
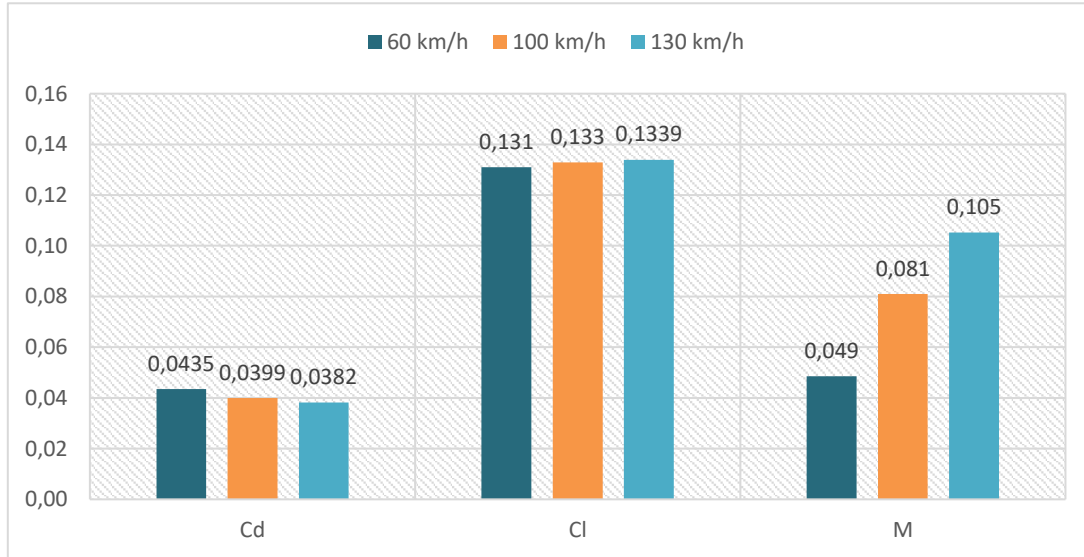
*Figure 18: **Drag and Lift Coefficients with Mach Number**: Comparison between Drag and Lift Coefficients and Mach Number of the front-wind analysis.*

Regarding the high-speed zones, due to the rounded shape of the front part, the air particles need to accelerate in order to surround the body. Then, the airflow continues its path around the Velomobile until it hits the windscreen, comprising itself and increasing its velocity.
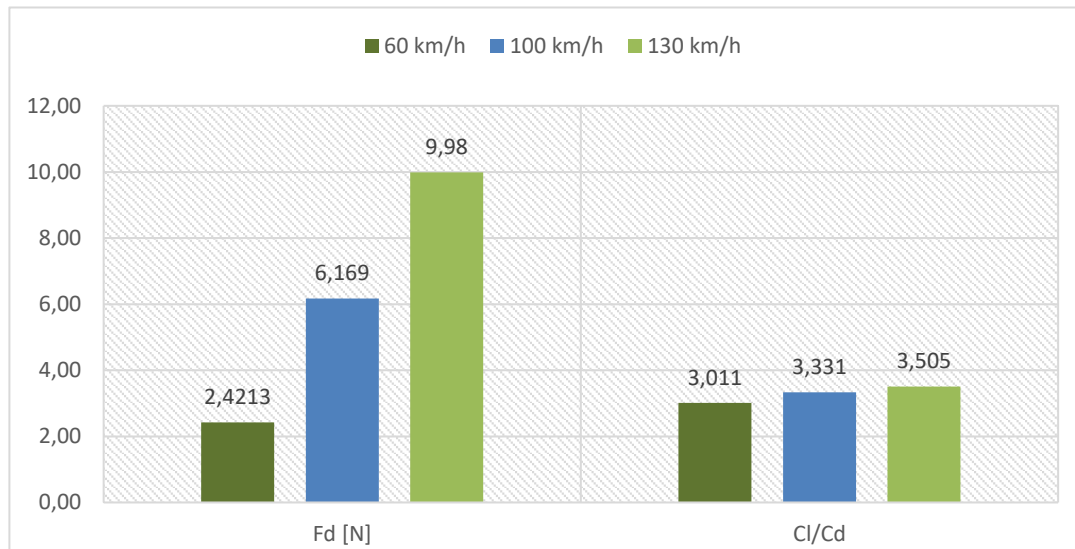
*Figure 19: **Drag Force and Aerodynamic Efficiency**: Comparison between the Drag Force generated and the Aerodynamic Efficiency of the vehicle.*

This phenomenon has both advantages and disadvantages. On the one hand, the increase in velocity in the faster airflow zones helps create lift force in those areas, reducing the weight of the vehicle and, consequently, improving the top speed. However, opposite to this benefit, the pressure at the front reduces the velocity, rises the resistance of the Velomobile to travel through

the air. Furthermore, having additional lift force is not beneficial if what is sought is to have a better road grip to enhance the tire torque transmission.

Regarding the efficiency of the design (Fig. 4.5), the *Aerodynamic Efficiency* value is very helpful to see in which aspects is the Velomobile aerodynamic enough to create more lift than drag by its pass through the airflow. For this specific case, the faster the vehicle travels, the better the frontal aerodynamic efficiency becomes. According to Figure 4.6, the Drag Coefficient sinks as the velocity increases, opposite to the Lift Coefficient, which grows slightly at the same rate. However, the maximum Drag Force exerted on the Velomobile is approximately five times bigger with just double the velocity (*Drag Force*).

Pressure

As far as pressure is concerned, the pressure contours (Fig. 4.7) follow closely the results of the velocity plot. The relation between both magnitudes comes from the effect mentioned in the *Bernoulli chapter*. The faster the airflow travels around a curved body, the lower the pressure becomes on that side. Hence, as the air molecules pass around the rounded nose, the velocity increases, creating the already mentioned additional lift force at the nose and the windscreen.

The high pressure zone originated at the tail, due to the gathering of eddies and low speed, results in a suction effect exacerbating the suction force in the opposite direction.
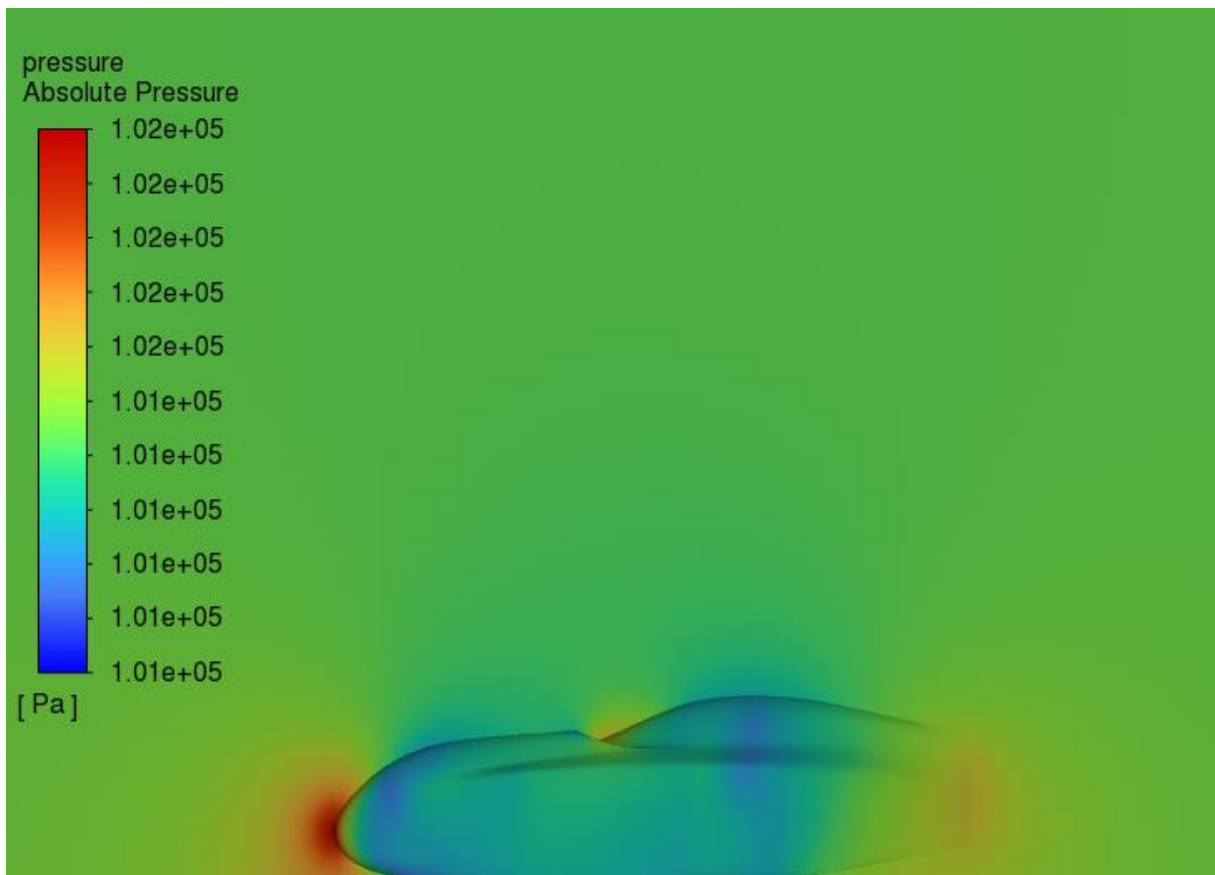
*Figure 20: **Pressure Contours**: Side-view of the front-wind case Pressure Contours.*

On the other hand, the bottom of the Velomobile is also affected by a change of pressure, where the airflow is rapidly sucked in under the vehicle showing slightly what in the *Bernoulli* and *Ground effect* chapters is demonstrated. The chassis works as an irregular Venturi tube, where the air goes under the tight space between the vehicle underbody and the road, and as a result of the acceleration and deceleration of the airflow, the vehicle acquires a ground effect.

Another aspect to consider is the middle zone between the knee bulges and the windscreen, where the airflow stalls, creating a zone of higher pressure hampering the pass of the flow at that place. In the *side-wind analysis* can be seen why this is happening (Fig. 4.14).

Wall Shear Stress

The Wall Shear Stress is a term used in fluid dynamics to describe the frictional force exerted by a fluid flowing over a solid surface. When a vehicle is moving through the air, the air molecules in contact with the vehicle's surface experience a velocity gradient, provoking to slow down its velocity, while the molecules further away from the surface have higher velocities. This velocity gradient creates a difference in momentum between the fluid layers, resulting in a shearing effect along the surface. These shear phenomena can cause the boundary layer to detach, creating eddies along the wake and stalling the vehicle.

As shown in the Figure 4.8, the rear part of the Velomobile has almost no shear stress, possibly due to the deceleration of the airflow at that zone. That develops into the detaching of the Boundary Layer, what, as mentioned before, slows down the vehicle and hinders the goal of surpassing the 100 km/h top speed. Furthermore, just before the windscreen, the boundary layer also detaches, creating an isolated zone of null velocity as mentioned in the pressure section. Which at the nose happens the contrary, because the flow encounters directly the fairing, being forced to bifurcate itself into different directions, and having a zone where the velocity reaches the null speed, this is called the stagnation point.
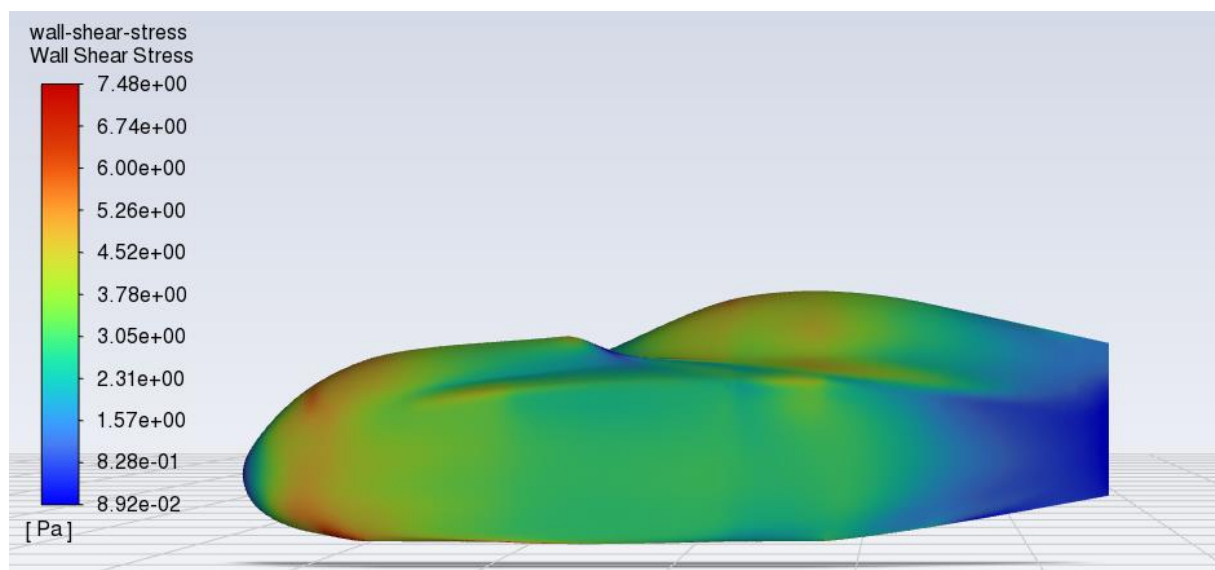
*Figure 21: **Wall Shear Stress Contours**: Wall Shear Stress Contours of the front-wind analysis.*

Reynolds Number

4. CFD Analysis of Previous Model

As mentioned in the chapter of the *Reynolds Number*, this parameter helps determine how turbulent is a flow interacting with an object. In this case (Fig. 4.9), the Velomobile is analysed with an airflow passing through the longitudinal axis, which, because of the streamlined longitudinal shape of it, doesn't generate great turbulences over the length of the chassis.

However, one of the most important parts of a vehicle is also the tail, where the flow leaves the
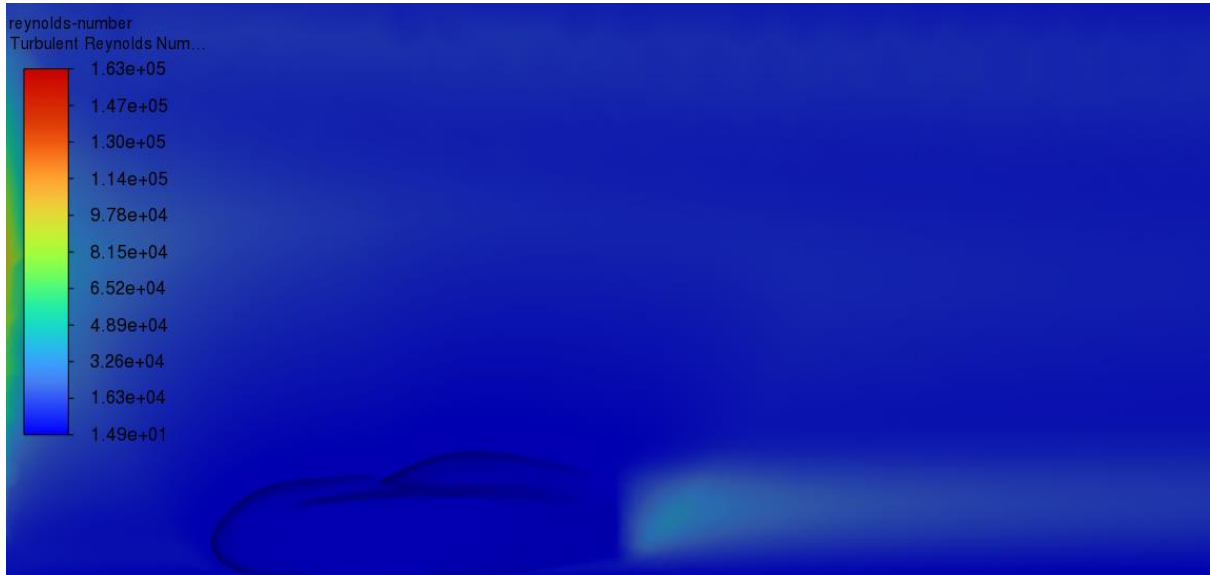
*Figure 22: **Reynolds Number Plot**: Side-view of the change of Reynolds Number at the end of the tail, where the wake starts to be turbulent.*

body, and it starts forming eddies in the wake, which creates the difference of pressure already remarked. This suction zone becomes turbulent, impoverishing the wake flow quality, which simultaneously reduces the maximum top speed achievable. The impact of this flaw could be reduced by improving the exit of the flow at the rear of the vehicle, keeping in mind that it has to generate as few vortices as possible. Also, it must be considered the fact that the changes on the longitudinal axis must not interfere in the performance of the vehicle on the transversal axis.
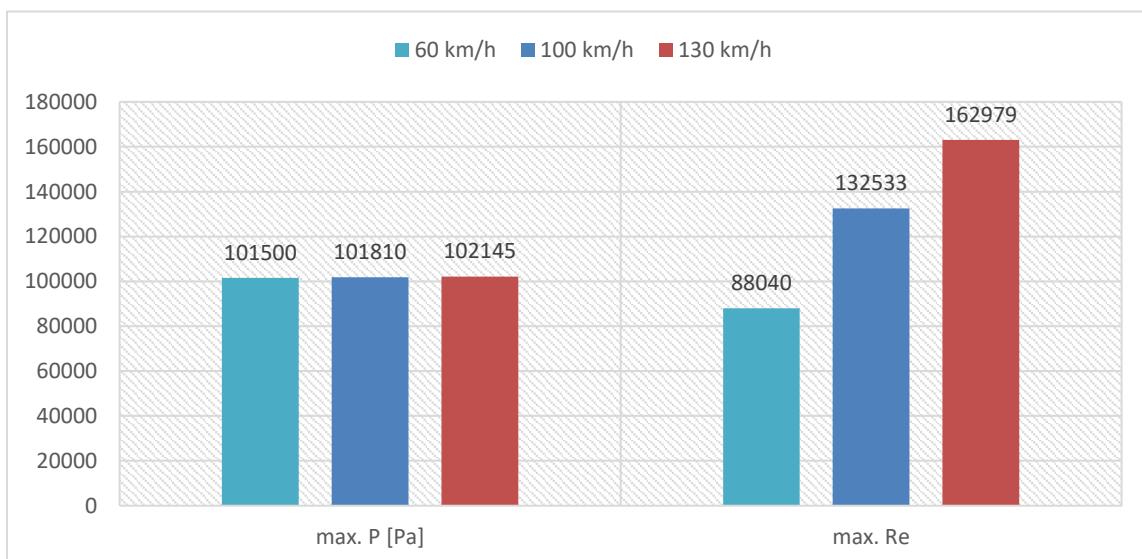
*Figure 23: **Pressure and Reynolds Number values**: Pressure and Reynolds Number values for the three front-wind cases: 60 km/h (cyan), 100 km/h (blue) and 130 km/h (red).*

4. CFD Analysis of Previous Model

One possible solution for improving the wake flow quality would be to reduce the size of the tail, provoking to stretch the trail left behind. Furthermore, knowing that the flow speed slows down at the bottom of the tail, causing the boundary layer to detach prematurely, a set of tiny vortex generators could be designed at the rear bottom of the Velomobile, ensuring that the boundary layer sticks to the body until the end. As seen in the chart (Fig. 4.10), the Reynolds Number increases proportionally to the velocity reaching a maximum of Re = 162979, which translates into a relatively turbulent wake.

4.2 Side-wind analysis

This second part is the main focus of the analysis, together with the diagonal wind analysis, where the wind comes perpendicularly to the side face with a certain velocity. Its main purpose is to find the zones of the Velomobile where the flow destabilises it even more, and then propose solutions based on these results to avoid the detriment of the manoeuvrability. The velocity range with which the Velomobile has been analysed is the following:

	m/s	km/h	M
v_1	4,17	15	0,0121
v_2	8,33	30	0,0243
v_3	12,50	45	0,0364

*Table 4.3: **Velocity ranges with Mach Number**: Velocity of the three cases for front-wind analysis and its Mach Number.*

4.2.1 Analysis outcomes

Velocity

As mentioned in the velocity plot from the front-wind analysis, the velocity magnitude results show how the flow behaves along the vehicle body. In this case in particular, the chassis is receiving the airflow from the side, which increases the difficulty of the manoeuvrability of the Velomobile. The contours displayed in Figure 4.11, show the most critical velocity range (v_3) present in the airflow, this going from the lowest speed of 0,0168 m/s (0,0605 km/h, which can be approximated to 0 km/h) to the highest speed of 32,52 m/s (117,7 km/h, being this value almost thrice the initial wind condition of 45 km/h).

The wind hits the 1,61 m^2 of the vehicle's side area, diverging the stream up- and downwards, generating an almost null velocity zone at the centre of the side face. This will create afterwards a transversal drag force of nearly 168,29 N (32 N at 15 km/h and 76 N at 30 km/h), which destabilises and worsen the driving comfortability. Additionally, the canopy turns into a great speed-up zone for the wind to accelerate and eventually detach from the body creating huge converging eddies, which, added to the bottom airflow, create a turbulent energy-wasting wake (Fig. 4.13).

4. CFD Analysis of Previous Model
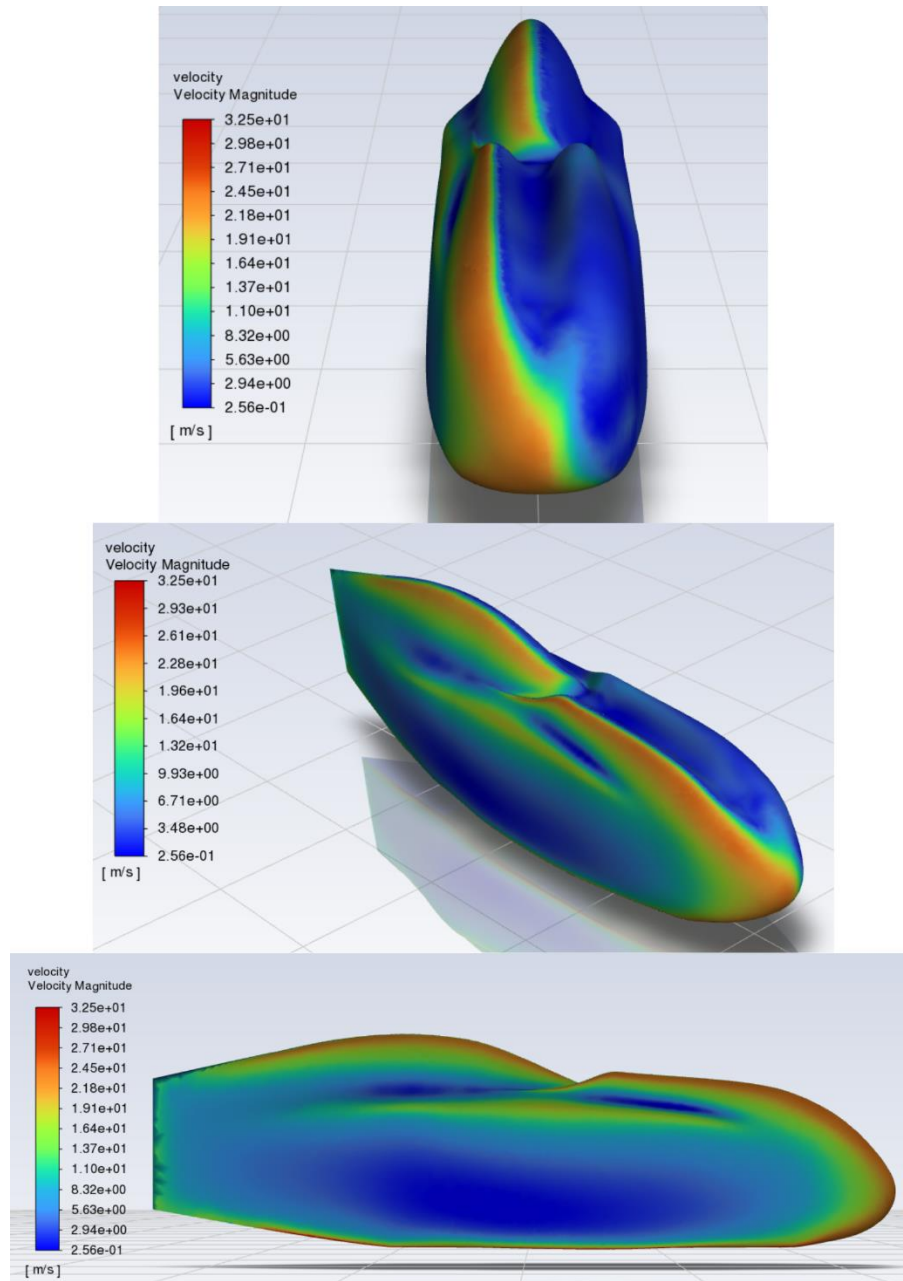
*Figure 24: **Velocity Contours**: Different views of the Velocity Contours for the side-wind analysis.*

Velocity streamlines

For this part, the streamlines help see the turbulences originated in the wake after the wind passes around the body, where the upper zone of the wake becomes the most turbulent due to the velocity it acquires, since the Reynolds Number is directly proportional to the velocity(3.1.). The airflow accelerates at the windscreen surface increasing the value of Re, which together with the eddies formed by the bottom airflow, it becomes a great turbulent wake, where a lot of energy is wasted trying to straighten the vehicle to not drift sideways.

In the Figure 4.12 the difference between the velocities on the Velomobile can be seen, where the most drastic difference between samples can be found in the $v_1 = 15\ km/h$, which has an increment of the speed of 405% in relation to the maximum speed, having the other two samples, v_2 and v_3, an increase of 254% and 260% respectively.

4. CFD Analysis of Previous Model
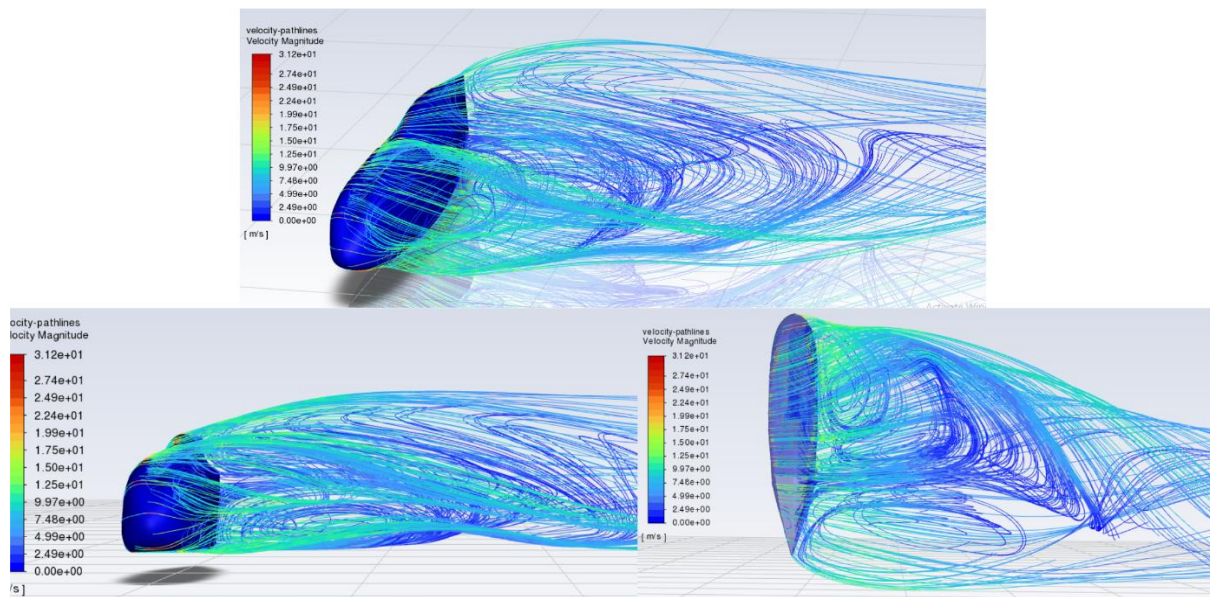
*Figure 25: **Velocity Streamlines**: Different views of the Velocity Streamlines for the side-wind analysis.*

Regarding the turbulences generated in the wake, the Figure 4.13 illustrates how the wake is prone to go backwards even though there is no wind coming from the front side. This is due to the difference of velocities between the nose and the tail, since at the nose, thanks to its round shape, the air is capable of accelerate while surrounding the fairing. Instead, at the tail, the air comprises and slows down, creating this difference of momentum, which consequently, the imparity of speeds creates big eddies within the wake.
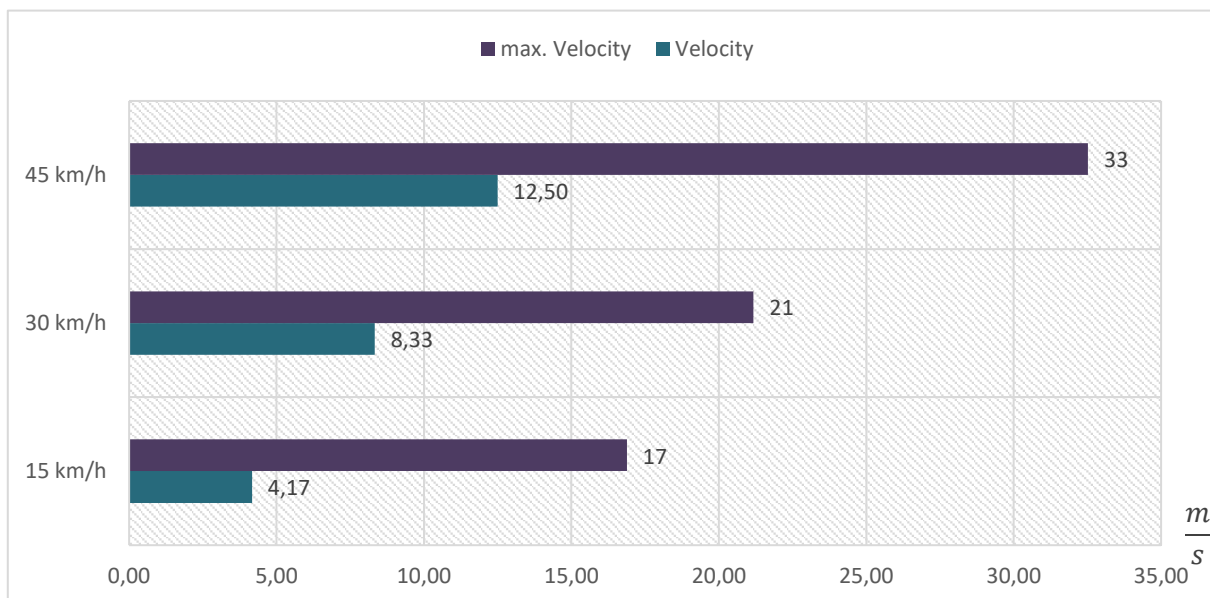
*Figure 26: **Initial and Maximum Velocity**: Comparison between the Initial Velocity values and the Maximum Velocity values achieved in certain zones of the fairing.*

The same phenomenon happens between the top and the lower part, where each of the airflows travels with a different velocity, being the upper flow faster due to the speed-up mentioned

before. Furthermore, as stated before, a bubble of stalled air is generated between knee bulges and windscreen, which can be seen with higher detail in the Figure 4.14. This null velocity bubble also takes part into increasing the wake turbulences, since a faster airflow passes over the bubble being pulled by it, and then mixing with the rest of the eddies, intensifying the turbulences consequences.
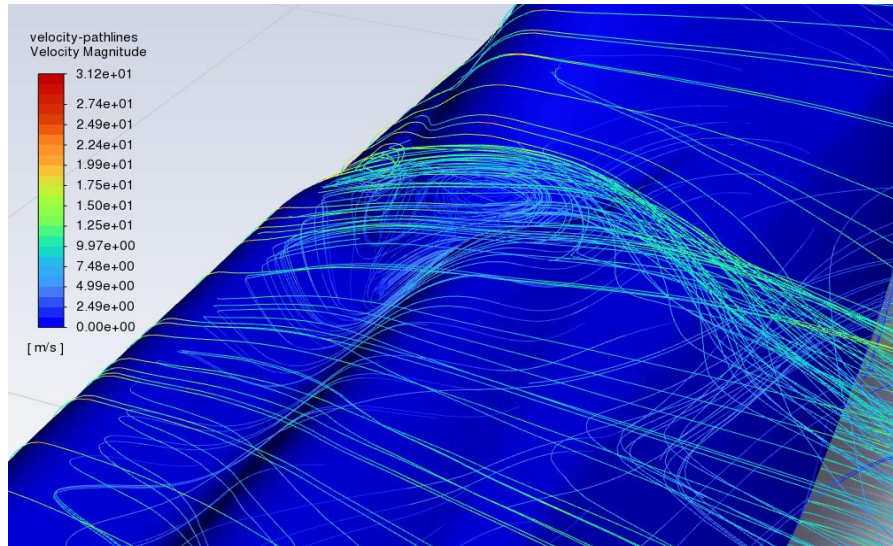
*Figure 27: **Knee bulges eddies**: Close-up view of the eddies formed between the knee bulges and the windscreen.*

Pressure

The Velomobile has two main pressure zones, being these also related to the velocity plot results. As shown in the Figure 4.15, the higher pressure is captured in the face where the wind hits directly the vehicle, leading later on to a decrease of this value due to the acceleration of the airflow at the edge of the upper part of the vehicle. Just after this pressure depletion, it comes back to normal over the whole opposite side, leaving an uneven distribution of pressures on the chassis. This change of pressure points out the line where the flow starts detaching from the boundary layer and creates the turbulent wake.

For this reason, to reduce the size of the turbulent bubble of eddies, the pressure difference between sides should be reduced to a minimum and the same for the superior zone (windscreen and knee bulges).

Despite the range difference not being as significant as in the velocity range, this unbalance of forces makes the Velomobile to continuously lean towards the opposite side while driving in a straight line. Furthermore, owing to the fact that the rear side has more area where the wind stagnates, the pressure is not symmetrically distributed and the resulting force on the side is slightly off-centre to the rear. This phenomenon does not interfere in the maximum top speed reachable, but it is not sought in a comfortable drive.

4. CFD Analysis of Previous Model
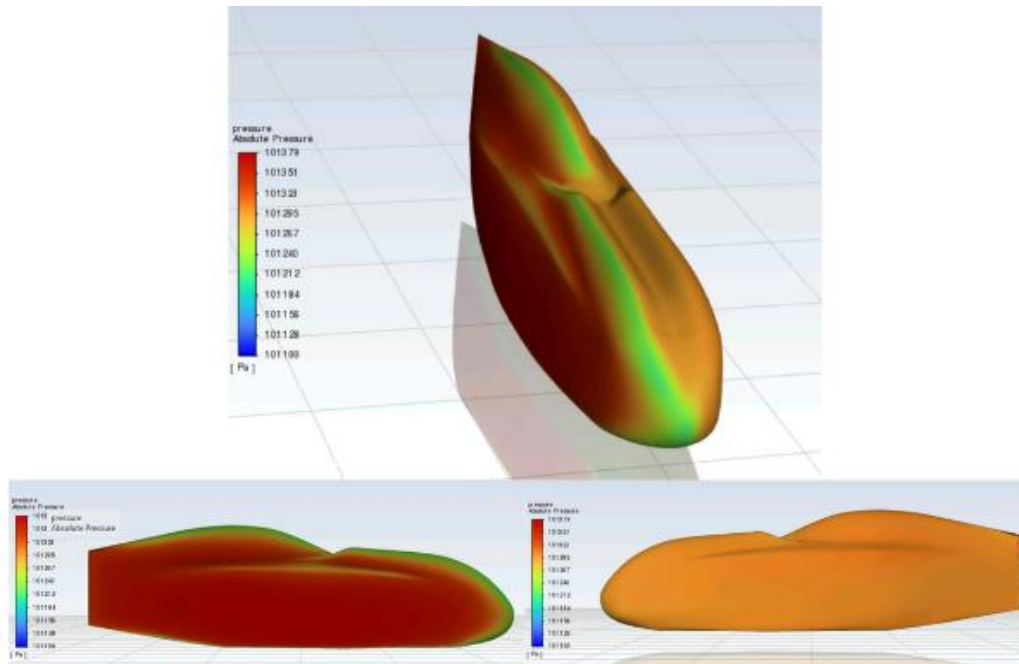
Figure 28: **Pressure Contours**: *Different perspectives of the Velomobile Pressure Contours: strong-side (left), isometric (top), weak-side (right).*

4.3 Diagonal-wind analysis

Additionally, two intermediate directions between front- and side-wind were studied. An airflow, at 22,5º and at 45º from the longitudinal axis, goes through the vehicle creating a diagonal wake as well. In this case, the velocity used is similar to the front-wind worst case scenario, where the airflow reaches a speed of 130 km/h, but with the distinctive feature that the wind blows against the Velomobile with a velocity of 45 km/h. This last analysis aims to find the Velomobile design features, which accelerate the detachment of the boundary layer and aggravate the turbulence of the flow, together with the results from the side-wind analysis. The outcomes from both analyses helped improve the design of the vehicle with several suggestions at the end of the research.

4.3.1 Analysis outcomes

Velocity

The velocity analysis aims to investigate the consequences of the interaction of the airflow with the Velomobile. The analysis involved measuring the velocity at several ranges and regions of the fairing, which provide valuable insights into the aerodynamic behaviour of the vehicle. This revealed that the airflow experiences significant changes in velocity as it interacts with the vehicle's knee bulges, where the results showed variations across different sections of the fairing, indicating the presence of areas with higher or lower velocities reaching a maximum of 119,09 m/s in the case of the wind coming from 45º (Fig. 4.16). Nevertheless, here is also the stagnation point, which is now displaced to the side. Moreover, the other bubble of stalled air is again in the zone between the knee bulges and the windscreen, now being altered by a vortex flow coming from the front of the knee bulges. This anomaly can be seen in the image of the velocity streamlines (Fig. 4.18).

4. CFD Analysis of Previous Model
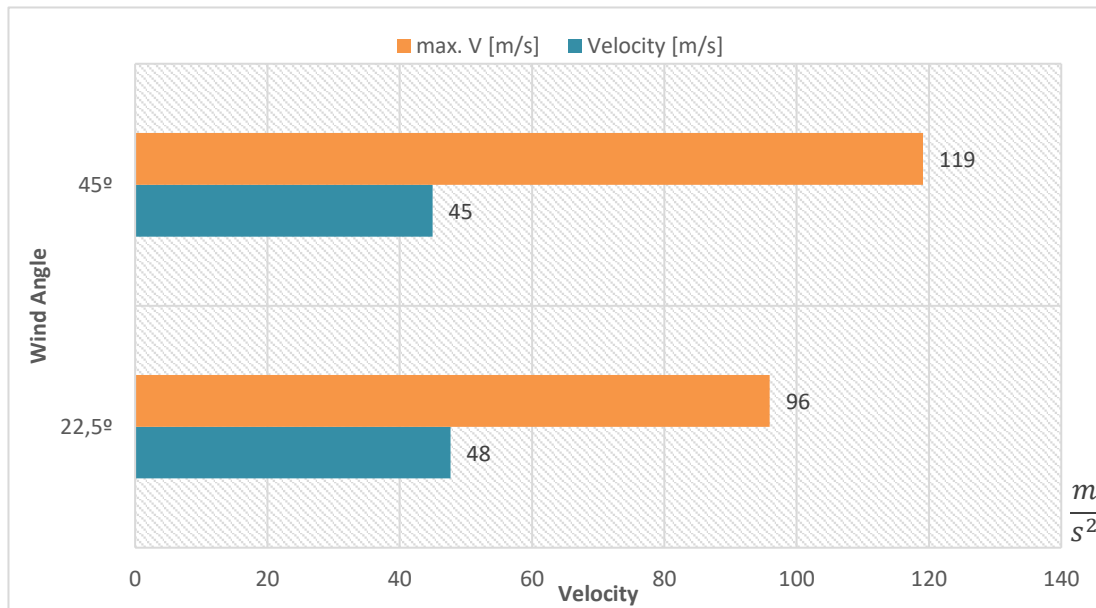
*Figure 30: **Initial and Maximum Velocities**: Initial Velocity values compared to the Maximum Velocity values for the 22.5° wind and the 45° wind cases.*
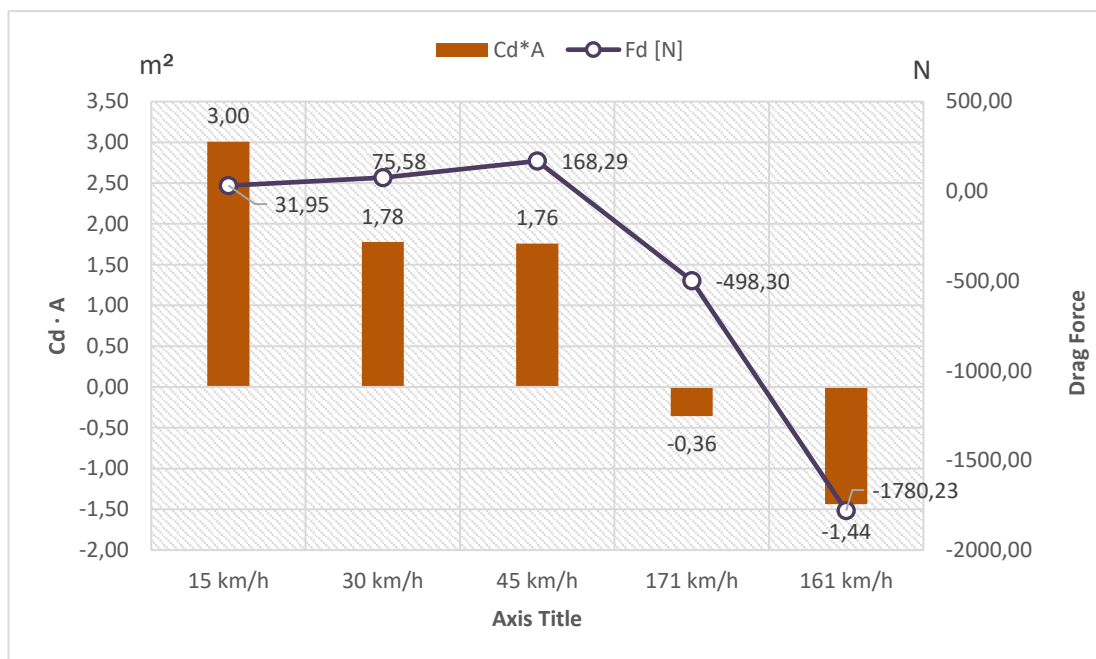
*Figure 29: **Drag Force and Effective Projected Area**: Comparison between the Effective Projected Area and the Drag Force of the diagonal-wind cases.*

Considering the outcomes in the Figure 4.17, the Velomobile shows a gradually scaling Drag Force for the three side-wind velocity cases (15 km/h, 30 km/h and 45 km/h), where this resistance duplicates from the 30 km/h to the 45 km/h due to the generated turbulences and the increment of the velocity. On the other hand, the diagonal-wind cases present an enormous leap between the 22,5° and the 45°. The vortices and eddies generated in the wake caused by the canopy and the knee bulges lead to a growth of the Drag Force to almost three times just for double the wind angle.

4. CFD Analysis of Previous Model
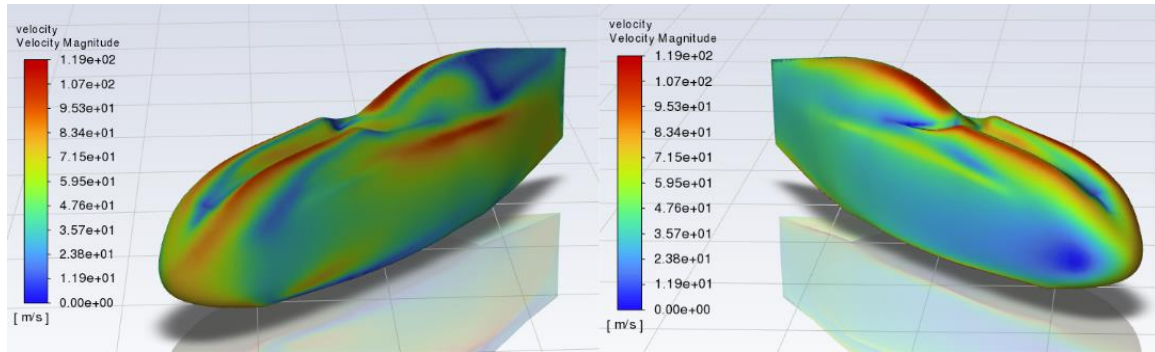
*Figure 32: **Velocity Contours**: Velocity Contours for the 45º wind case, being this the worst case scenario. Wake side (left image), airflow direction perspective (right image).*

On the other hand, other areas, such as over the windscreen and underneath the vehicle, also have an increase in speed due to the sudden change in the shape of the fairing. These regions of higher velocity can be indicative of low-pressure zones and potential aerodynamic drag, where afterwards the airflow detaches from the boundary layer creating the eddies seen in the Figure 4.18. In these results can be seen how the wake becomes extremely turbulent, generating a Drag Force of approximately 50 kg for 22,5º and over 180 kg for 45º. Furthermore, the Table 4.4 shows how the change in the angle, despite being the airflow slower at 45º (due to the bigger projected area), the airflow is forced to accelerate further over the surface of the vehicle, thus acquiring a higher maximal velocity.

Angle	Projected Area [m^2]	Velocity [km/h]	Fd [N]	max. V [km/h]	M	M*	v_{max}/v %
22,5º	0,7046	171,57	-498,30	345,38	0,1389	0,2797	201,30
45º	1,192	161,82	-1780,23	428,72	0,1310	0,3472	264,94

*Table 4.4: **Diagonal Analysis Results**: Diagon Analysis Results for the 22.5º wind and 45º wind cases.*
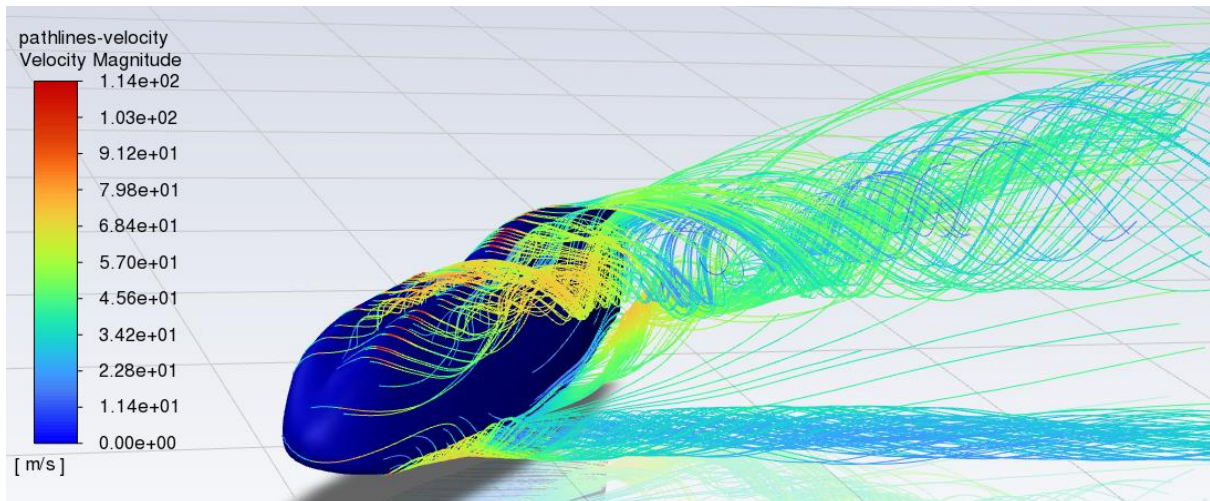
*Figure 31: **Velocity Streamlines**: Velocity Streamlines for the 45º wind case.*

The relationship between both Mach Numbers is also interesting, since it shows how much the airflow changes from its initial state of 0.131 times the sound velocity to 0,3472 of the sound velocity at the maximal velocity at 45º in the red zones of the Figure 4.19. This variation supposes an increment of almost the 265%, what is not a desirable feature for the design of the Velomobile.

4. CFD Analysis of Previous Model

In the Figure 4.19, the velocity contours show the drastic changes in the airflow velocity over the fairing of the Velomobile, which in some cases, such as at the stagnation point, the flow goes from being stopped to travel at a third of the speed of the sound barrier. This phenomenon is completely undesirable, since these extreme differences between different zones of the vehicle at high velocities can make the Velomobile drift away or overturn instantly. That is why a proper solution like smoothing, rounding or lengthening the shape of the vehicle, in order to reduce the abrupt change of velocity, needs to be considered.

Pressure and Reynolds Number

The pressure analysis aims to examine the distribution and characteristics of pressure throughout the flow surrounding the Velomobile and understanding the pressure patterns is crucial for comprehending the aerodynamic behaviour and its impact on the vehicle's performance.

The analysis revealed the presence of varying pressure regions around the vehicle (Fig. 4.20), where, for instance, at the nose of the vehicle, a high-pressure region was observed due to the airflow deceleration caused by the presence of a stagnation point. This high-pressure zone normally contributes also to the overall resistance that hinders the velomobile to reach higher velocities and to destabilise it. Additionally, the airflow moves along the vehicle's surfaces, where the pressure gradually decreases (windscreen, knee bulges and underbody), indicating the generation of lower pressure regions, which at the same time denote a possible detachment of the boundary layer. This kind of interaction can make the wake to eventually become turbulent, and consequently increase the total drag.
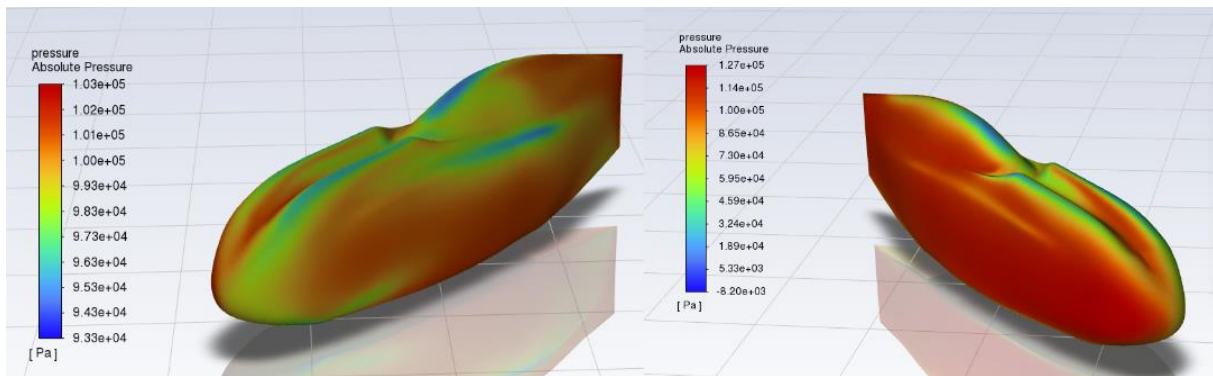
*Figure 33: **Pressure Contours**: Pressure Contours of the 45º wind case, being this the worst case scenario. Wake side (left image), airflow direction perspective (right image).*

Furthermore, the pressure analysis provides insights into the force exerted on specific zones, such as the nose (between bulges), the side face or the tail. These parts exhibit pressure variations, indicating where exactly are the wind forces applied, giving a slight idea of where a change in design must be implemented to reduce the instability of the Velomobile.

4. CFD Analysis of Previous Model
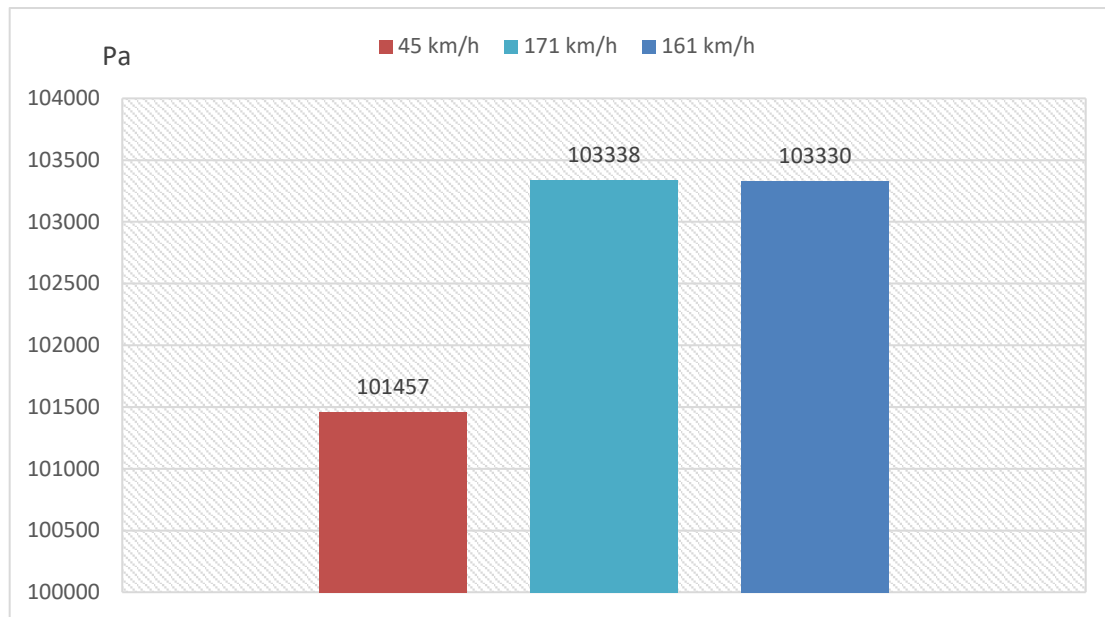
*Figure 35: **Maximum Pressure Values**: Maximum Pressure Values for 45 km/h side-wind (red), 22.5º wind (cyan) and 45º wind (blue).*
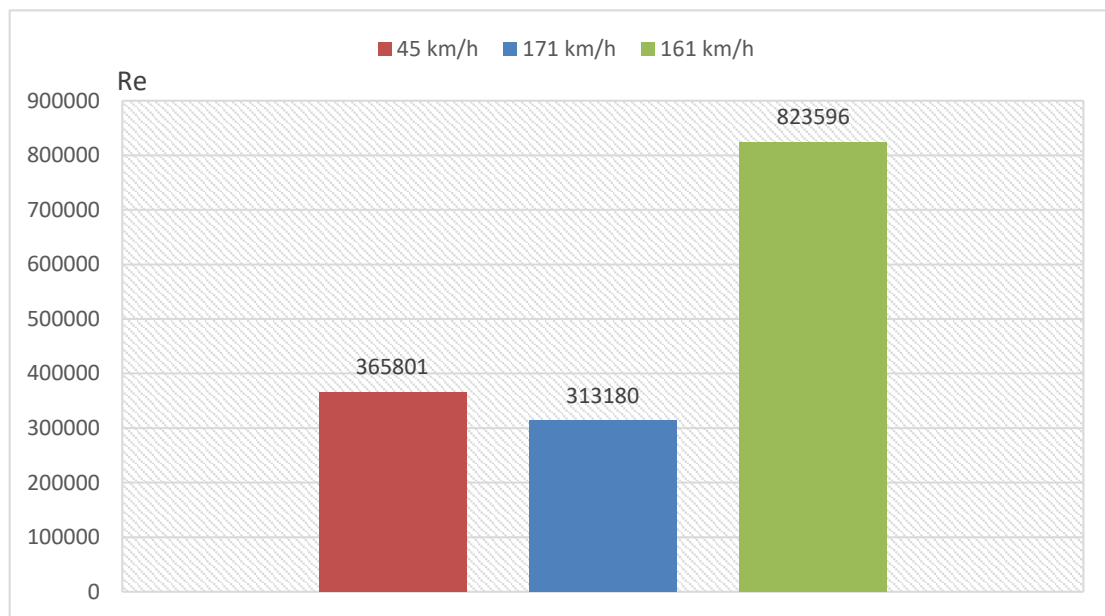
*Figure 34: **Reynolds Number Comparison**: Comparison of the Reynolds Number for the side-wind (red), the 22.5º wind (blue) and the 45º wind (green).*

Looking the comparison chart above (Fig. 4.22), a noticeable difference between the Reynolds Number values can be seen, where the red column belongs to the side-wind analysis at only 45 km/h, the blue column represents the value from the diagonal-wind analysis at 22,5º and 171,57 km/h, and the green column is the value for what appears to be the worst case scenario, where the wind comes from 45º at 161,82 km/h. This last value is approximately 2,25 times more than the value from the side-wind analysis, meaning also that the wake left behind from the diagonal-wind analysis is also twice as turbulent as in the side-wind case. This is provoked by the increment of the velocity, since the vector of the diagonal wind coming from the front adds up to the vector of the airflow already travelling through the vehicle, increasing the overall airflow velocity to the mentioned 161,82 km/h. What is also unusual, is that the maximal Reynolds

Number for the 22,5° case is even lower than for the side-wind case. This could be due to the decrease in the projected area, what consequently reduces the drag coefficient.

As opposed to this, the comparison between pressures does not show such a drastic contrast between the variations in the diagonal-wind case (Fig. 4.21), but there still exists a perceptible leap from the side-wind analysis (red column) to the diagonal-wind analysis (cyan and blue columns).

Wall shear stress

This analysis part's purpose is to comprehensively investigate the distribution and characteristics of wall shear stress along the surfaces of the vehicle, holding paramount importance in evaluating the frictional forces exerted by the airflow on the vehicle's surfaces and their consequent impact on the vehicle's aerodynamic performance. The results obtained from this wall shear stress analysis provide invaluable insights into the magnitude and direction of the tangential forces that act on the vehicle due to the airflow.

The Figure 4.23 presents a representative visualisation of the wall shear stress distribution obtained from the worst case scenario (45° diagonal-wind). It offers a visual depiction of the complex wall shear stress patterns along the vehicle's surface, aiding in a more intuitive understanding of the analysis results, which expose significant variations in wall shear stress levels across distinct regions of the vehicle's surfaces, such as the top, the knee bulges or even the transition zone between the side face and the windscreen. Notably, elevated wall shear stress is observed at the leading edges of the underbody and areas proximal to flow separation points, suggesting intensified frictional forces and potential drag generation, underscoring the criticality of these regions in the overall aerodynamic behaviour of the vehicle.
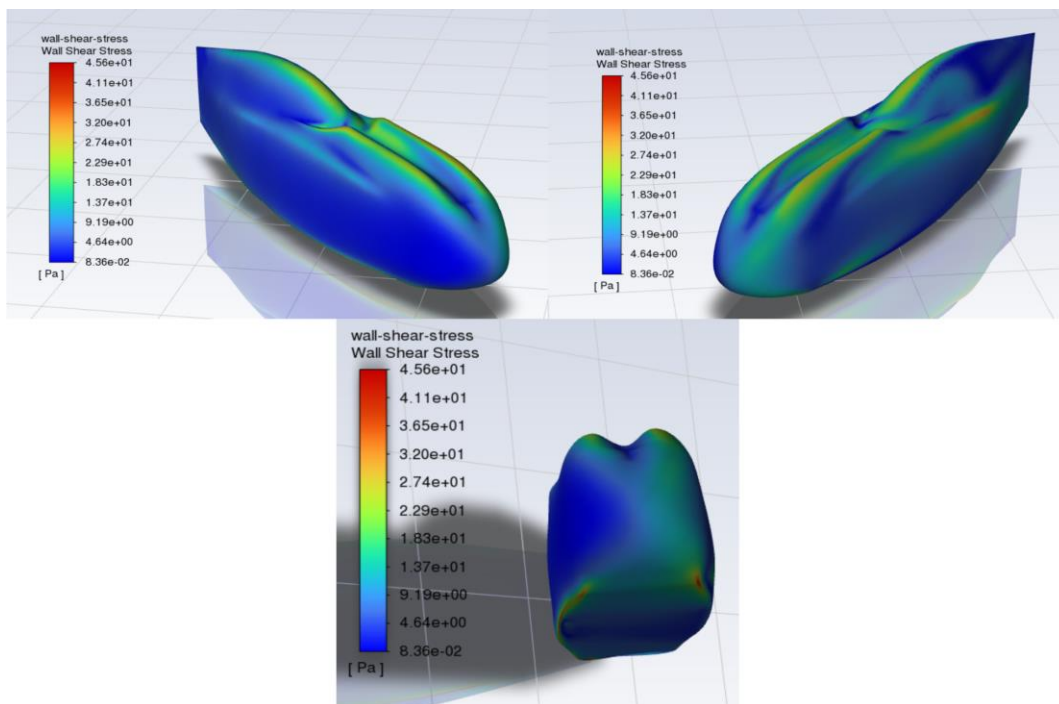
*Figure 36: **Wall Shear Stress Contours**: Wall Shear Stress Contours of the Velomobile from different points of view. Airflow direction perspective (top left), wake side (top right) and bottom view (bottom).*

5. Redesign suggestions

Taking into account the considerations made in the research carried out on the original Velomobile design [RaT23], there were several zones where a redesign was indispensable for the improvement of the Velomobile performance. At the front, the nose was under big pressure due to the size of the projected surface and the shape of it, which made the airflow bend around the top of the nose increasing the pressure. Just after it come the knee bulges, which create substantial vortices under diagonal and side wind conditions. Furthermore, the space between these bulges and the windscreen makes the airflow stagnate, forming a low-pressure zone developing even more drag.

On the other hand, the flat shape of the sides and the tail forces the wind to bifurcate creating a big stagnation zone and a side force that hinders the manoeuvrability of the vehicle. It is clear, that the original version was optimised for front wind, what implies the overall shape of the Velomobile to be focused on being aerodynamic from the front view only. The main purpose of this thesis is to redesign the Velomobile to improve its aerodynamic performance.

Below there is a design evolution diagram (Fig.5.1) made to gather several possible design implementations, in order to get a general overview of the changes and decisions made to reach to the final design. In this image is shown the path followed from an original design through several change propositions and then, reaching a final point with the most valuable and relevant change ideas.
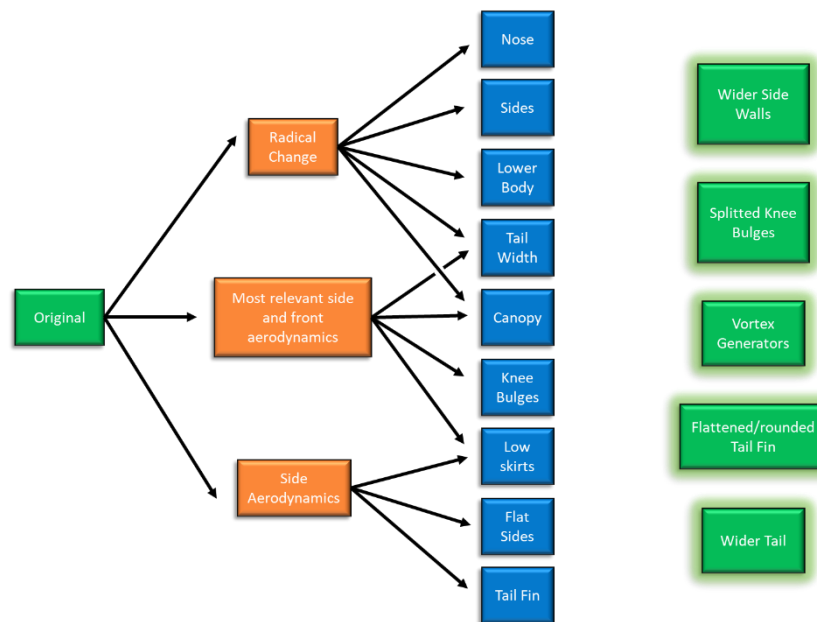
Figure 5.1: **Velomobile Design Evolution Diagram**: Diagram showing the choice evolution in the design process of the Velomobile.

As seen in the picture above, the main parts that are going to be affected by the changes are the following:

- Nose
- Knee bulges
- Side walls
- Canopy
- Tail

5. Redesign Suggestions

Considering the aerodynamic analysis and the diagram above, the more reasonable change to implement to the front part of the vehicle is to round off the nose, giving it a smaller projected area and a slightly smoother profile, which leads to a pair of less prominent knee bulges. The overall shape is planned to be lower in height and more streamlined, leaving a gap in the middle of the knee bulges at the front to let the side wind flow pass through without creating more unnecessary drag. A suitable variation to enhance the side walls contour is to widen the fairing giving it a curvier form instead of the flatness it has. This will allow the flow to surround the fairing with ease, creating a smaller stagnation zone on the side.

In what the rear part of the Velomobile concerns, as already mentioned, the canopy height is also being reduced, diminishing the side projected area, but concurrently decreasing the space for the driver, what must be also considered for ergonomic and visibility reasons. Moreover, since the width difference between the middle and the rear is the cause of the boundary layer detachment, the tail width is going to be enlarged to reduce this consequence.

In overall, the design change plan of the vehicle is to obtain a smaller projected area with a smoother streamlined shape for diagonal- and side-wind conditions in order to achieve a lesser drag force.

These choices were taken following a basic product development method, which is based in defining the problem, gathering information to solve it, propose possible solutions and then implement them to see if they work and how can then these solutions be further improved.
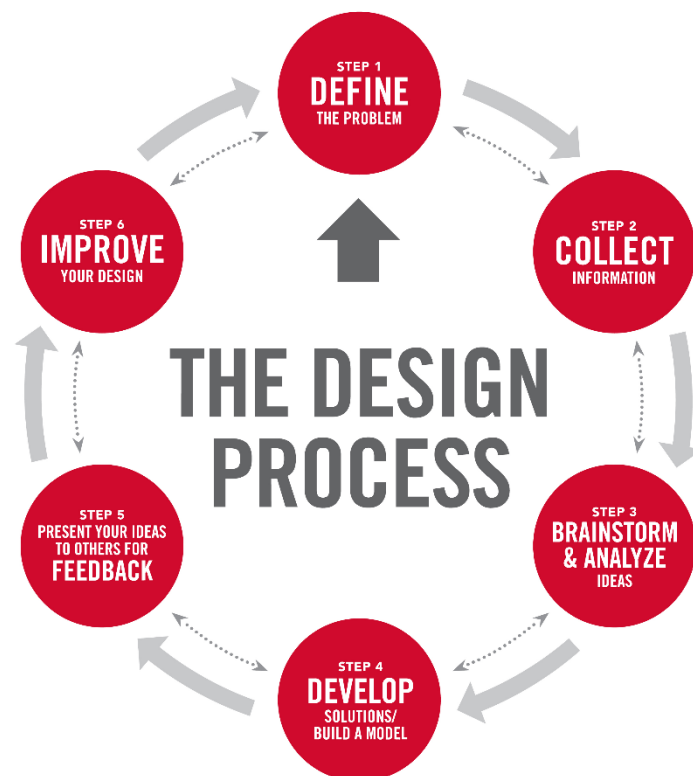
Figure 5.2: **Design Process Method**: Design Process Method Cycle. [Chi19]

6. CAD Modelling

6.1 Driver Space Necessity

When embarking upon the design of a velomobile, meticulous considerations of various critical measurements are essential to ensure optimal performance, ergonomic fit, and aerodynamic efficiency. These key dimensions encompass the wheelbase, defined as the distance between the front and rear axles, which profoundly influences stability and manoeuvrability. The track width, denoting the lateral separation between the vehicle's wheels, is pivotal for lateral stability and handling characteristics.

Furthermore, the overall length and width of the velomobile play a crucial role in determining its spatial footprint and, consequently, its aerodynamic profile. The rider's anthropometric measurements, including height and inseam length, are paramount for configuring an ergonomic seating position that aligns with biomechanical principles. The ground clearance, quantifying the vertical distance between the lowest point of the vehicle and the ground, influences the velomobile's adaptability to varying terrains.

Additionally, considerations of the frontal area, denoting the frontal projected area exposed to oncoming air, directly impact aerodynamic drag. The cockpit dimensions, encompassing the width and height of the enclosed rider compartment, contribute to both aerodynamic efficiency and rider comfort. The weight distribution across the velomobile, particularly between the front and rear wheels, significantly affects stability during acceleration, deceleration, and turns.

The *Saeta* body's geometry is not solely contingent upon a design optimized for fluid dynamics. A pivotal factor in configuring the driver's anthropometric dimensions involves the desired seating position. This consideration encompasses various parameters, notably the individual height of the drivers earmarked for the development of the forthcoming velomobile. Broadly speaking, the design caters to individuals of middle to high stature, with broad shoulders. The following seat measures (Fig. 6.1), which are derived from the existing Milan GT Velomobile, serve as the foundational element for determining these spatial requisites.
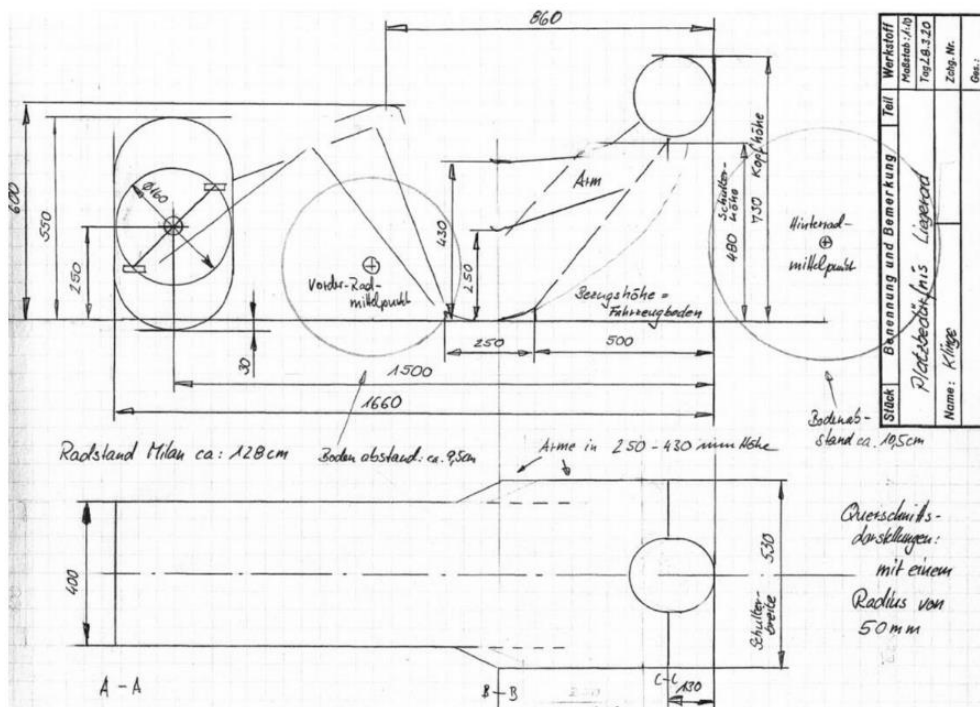
*Figure 37.1: **Velomobile Rider's Anthropometric Dimensions**: Image of the driver's seat measures (in cm) leaned back in the velomobile. [Klinge, 2020]*

6. CAD Modelling

The inception of the vehicle's modelling traces back to a student's project design of a *Wingvelo*. The scrutiny of the model revealed a hindrance in the view field of the driver and a rough dimensioning of the vehicle regarding aerodynamic aspects of the velomobile. To pre-empt such issues in subsequent development phases, a strategic decision was made to devise a model aligning with the specific spatial requirements of the driver.

In the process of designing the fairing for a velomobile using a CAD program, a methodical approach is employed to ensure accuracy and effectiveness. Initially, the contours of the fairing are established, considering aerodynamic principles and ergonomic factors. This involves outlining the general sections and proportions of the front, mid, and rear sections of the fairing (Fig 6.2).

Following this, the fairing design is subdivided into distinct sections to facilitate detailed modelling. Each section is carefully defined, taking into account specific aerodynamic requirements and geometric intricacies. For this method tools like spline curves and NURBS (Non-Uniform Rational B-Splines) are used to articulate the smooth, continuous surfaces characteristic of the fairing sections. An emphasis has been placed on achieving seamless transitions between adjacent sections, minimizing drag, and optimizing aerodynamic efficiency, involving in the process iterative refinement, where the curvature and surface continuity are scrutinized, and necessary adjustments are made to achieve a coherent and streamlined form.
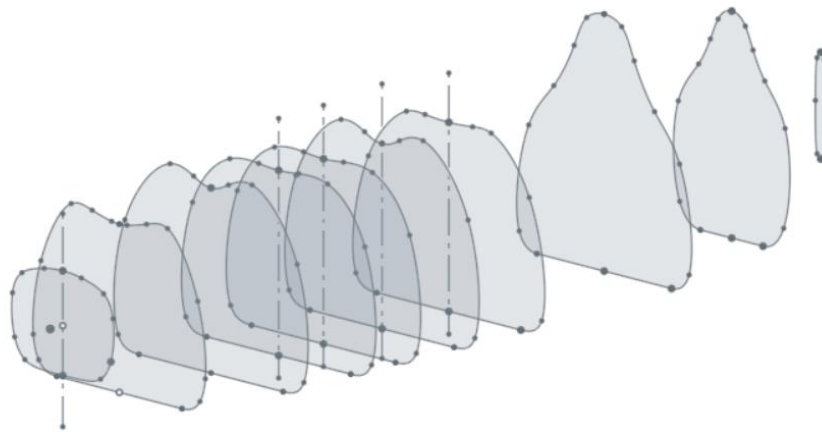
*Figure 6.2: **Fairing Model Sections**: Image of the sections made to the fairing for the design of it in 3D.*

Then a general consideration for structural integrity is incorporated into the refinement of fairing sections to accommodate mounting points, access panels, and other functional features. This involves striking a balance between aerodynamic performance and practical considerations, such as ease of manufacturing and maintenance. Throughout this intricate process, the parametric capabilities of the CAD program [Onshape] are utilized to maintain flexibility and facilitate modifications as needed.

6. CAD Modelling
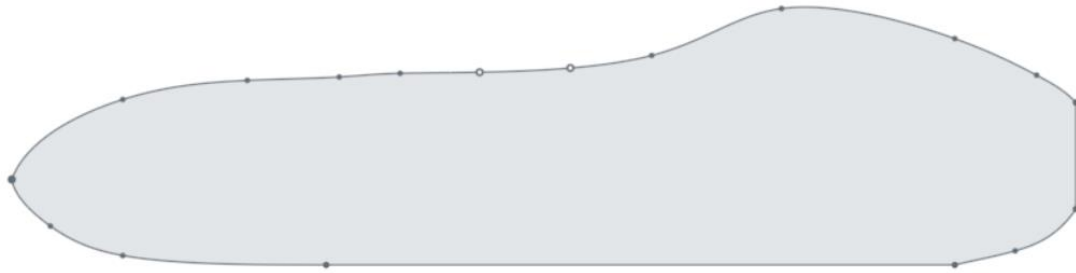
*Figure 6.3: **Centre Profile Section View**: Image of the Centre Profile Section made to design the Velomobile.*

This profile section is afterwards used to perform a compound loft using front and profile section, with several guide curves to adapt the form to be more aerodynamic, and then meticulously connect the section points to secure the streamlines of the vehicle. This process is thoroughly explained in the Section *6.2 Model Construction*, which shows the basic tools used to design the 3D model of the *Saeta* Velomobile, the redesigned version of the *Wingvelo*.

6.2 3D Model Design Tools

In the CAD program Onshape, 3D modelling tools operate based on mathematical representations of geometric entities to define and manipulate complex surfaces. Operations such as spline curves (like Bézier or NURBS) serve as fundamental tools for shaping curves and surfaces, which are defined by control points and mathematical algorithms, allowing to create smooth and continuous shapes.

On the other hand, the lofting tool enables the creation of surfaces by interpolating between cross-sectional profiles (Fig. 6.2) generating a smooth transition between these sections and facilitating the design of complex shapes with varying contours. This method is particularly useful for creating aerodynamic profiles, ensuring a streamlined and cohesive form. Moreover, 3D spline curves extend the concept of 2D splines into three dimensions, providing greater flexibility in shaping intricate curves and surfaces in a three-dimensional space. These are usually created to precisely guide the curvature and orientation of the surface intended to create, just like the one seen in the Figure 6.4.

Additionally, the CAD program's parametric modelling capabilities allow to establish relationships between different elements of the model, enabling dynamic modifications and providing the flexibility to adapt the design efficiently. This is crucial in the iterative refinement process, where its parameters can easily be adjusted to optimize the model for various criteria, such as aerodynamics, aesthetics, or structural integrity.

In overall, the synergy of spline curves, lofting, 3D spline curves, and parametric modelling within a CAD program provide the opportunity to create sophisticated and precise 3D models, particularly valuable in applications like velomobile design where aerodynamics and form intricacies are critical considerations.

6. CAD Modelling
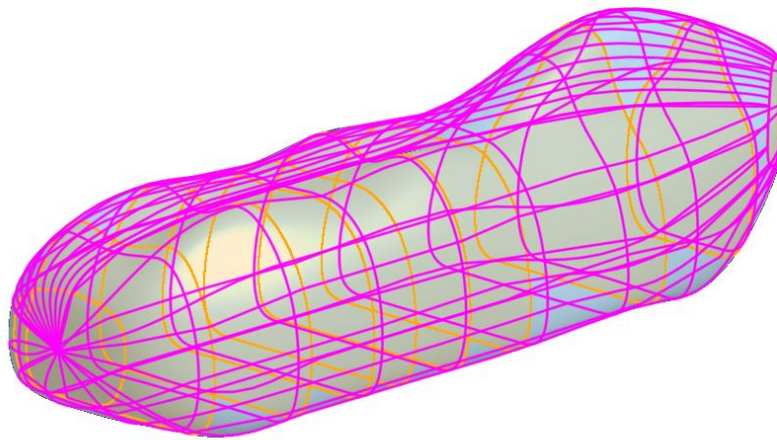
*Figure 6.4: **Lofted body with isocurves**: Image of the Saeta design pre-lofted body.*

6.3 Model Construction

For the final design of the *Saeta* Velomobile, several adjustments have been performed to adapt the form of the vehicle to an aerodynamic and efficient shape, which afterwards will be tested under CFD analyses with Ansys Fluent, and it will be compared with its former version obtained from the *Wingvelo*.

Using the lofting tool, the sections showed in Figure 6.2 have been unified into a solid lofted body, while the ideal shape has been secured by connecting the section points meant to be the guide curve to contour the vehicle body. These connections, shown in Figure 6.5 as fuchsia lines, outline the vehicle shape and allow the loft to create a solid aerodynamic body, which can be reiteratedly modified with ease changing the parameters of each section of the *Saeta* design [ART23].
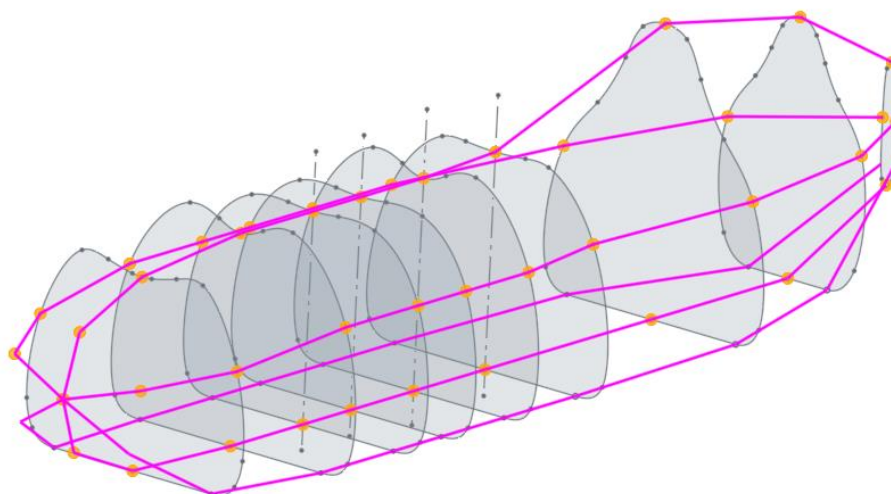
*Figure 6.5: **Pre-lofted vehicle view**: Image of the pre-lofted vehicle with connection points unified by lines.*

6.4 Models Comparison

Once the model is already designed, several differences can be seen at first sight. In the image below (Fig. 6.6) the two models, the original *Wingvelo*'s fairing on the left and the *Saeta* on the right, have a long body with a similar canopy height of 0,78 m for the *Wingvelo* and 0,72 for the *Saeta*, which measure affects the side wind the most other than the front wind.

On the other side, the *Saeta* has been widened approximately 10 cm on each side (from 0,54 m to 0,75 m) with a smooth round form to help the airflow go around the fairing easily and reducing the stagnation zone created on the side of the vehicle. This change would also imply an increment of the frontal projected area, what consequently increases the frontal force exerted by the wind. Since the addition of the total 21 cm of width is a significant change, the outcome in the CFD analysis probably going to reflect a small decline in efficiency for front wind aerodynamics.
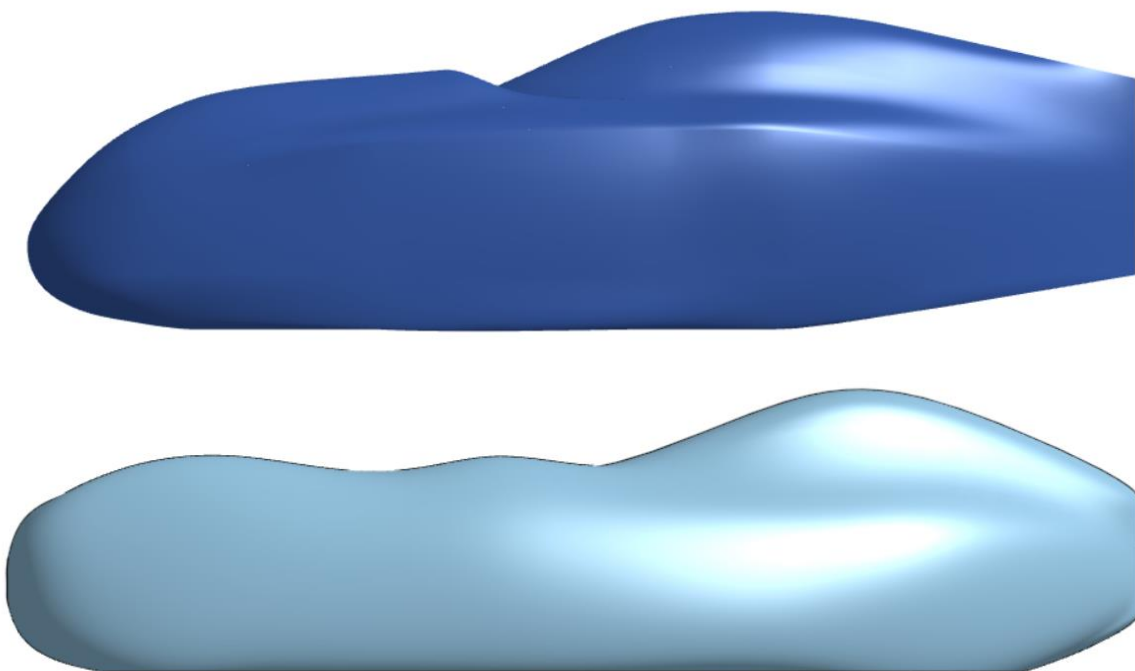
*Figure 6.6: **Velomobile models comparison (profile view)**: Image of the Wingvelo (top) and the Saeta (bottom) models compared.*

Apart from the general measures of the velomobiles, a noticeable restyling has been made to the nose, knee bulges, canopy and tail, rounding and smoothing the surface details to allow a better pass of the flow in every direction. In the previous CFD analysis of the *Wingvelo* fairing, the detachment of the boundary layer has been detected happening slowly at the middle of the canopy, leaving the rest of the vehicle (almost the half of it) with a dirty airflow, hence the shift of the canopy position backwards and the smoothening to the tail end seen in Figure 6.7. Regarding the eddies generated by the valley between the knee bulges, a design change has been applied removing the unneeded space in the middle of the knee bulges and lifting the height of the valley between them, creating the shape seen in Figure 6.6, and accordingly lengthening the *Saeta* to match the available pedalling space.

Additionally, under the tail, where the tire should be placed, there has been a slight modification reducing the tail length, in order to avoid the detachment of the flow right after the tire.

6. CAD Modelling
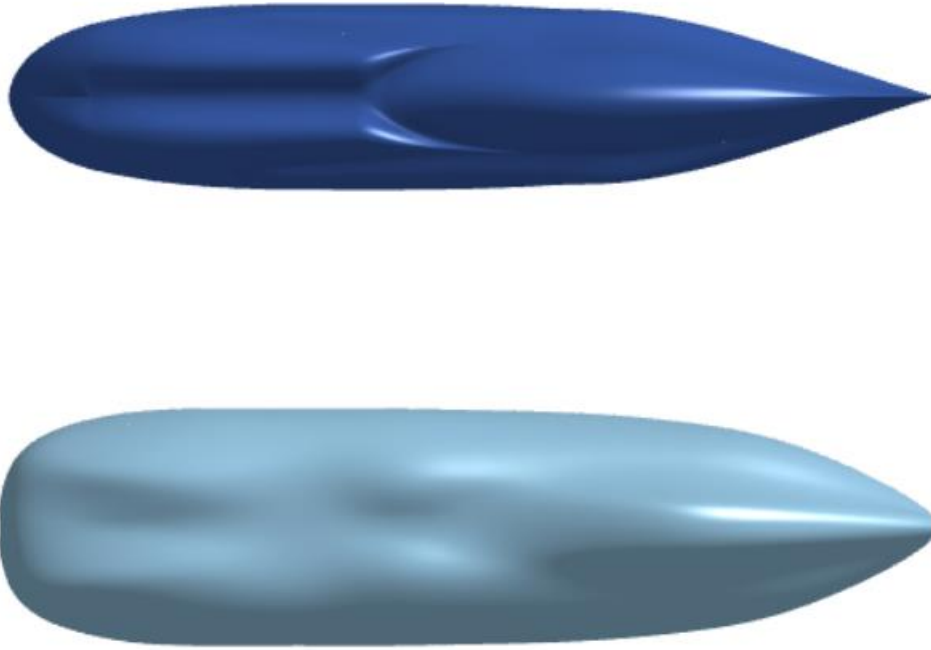
*Figure 6.7: **Velomobile models comparison (top view):** Image of the Wingvelo (top) and the Saeta (bottom) models compared.*

7. CFD Analysis of the Final Design

As previously mentioned in chapter *4. CFD analysis of the previous velomobile model*, for the following simulation the Spalart-Allmaras (SA) model is more appropriate, since the model is not yet built, and the values obtained cannot be adapted depending on the data gathered from the wind tunnel. Furthermore, the Spalart-Allmaras model exhibits a smoother behaviour near walls, which is advantageous in simulations involving boundary layer flows. This characteristic also helps avoid numerical issues and provides more stable solutions in scenarios where the flow near the wall is critical to the overall aerodynamic performance.

For this part of the Thesis, the results regarding the aerodynamic analysis of the *Saeta* are going to be exposed and compared with the past results obtained from the analysis of the *Wingvelo*. On one hand, the *Saeta* is going to be subjected to front-, diagonal- and side-wind scenarios at 100 km/h, 121 km/h and 30 km/h respectively. These situational speeds are chosen to observe how the vehicle behaves at the maximum speed reached until the date with the last prototype of velomobile in order to improve the design and implement the favourable features of this design to the current velomobile prototype.

On the other hand, the results comparison between designs will be used to see how the modifications made have affected the overall aerodynamic performance of the vehicle, and to consider the implementation of them to future prototypes.

The simulation for the *Saeta* velomobile uses a mesh with almost 1,5 million cells and an Orthogonal Quality of around 0,12, which demonstrate that the results obtained are more accurate and reliable.

Regarding the simulation configuration, the environment conditions are going to be the same as the last simulation, and the parameters will be kept the same for all following tests as follows:

$$\text{Temperature: } T = 288,16 \ K$$

$$\text{Pressure: } p = 101325 \ Pa$$

$$\text{Density: } \rho = 1,225 \ \frac{kg}{m^3}$$

$$\text{Dynamic viscosity: } \mu = 1,7894 * 10^{-5} \frac{kg}{m \cdot s}$$
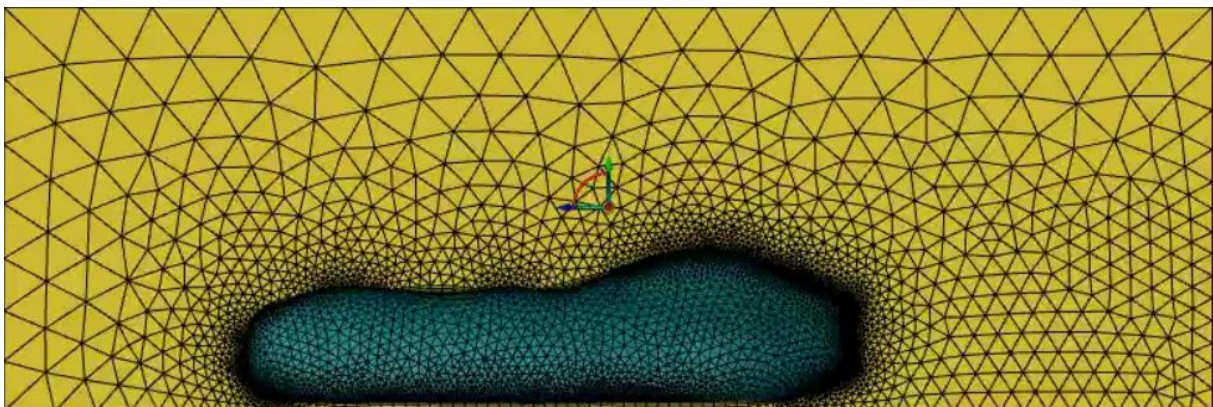
*Figure 7.1: **Saeta Mesh**: Image of the Saeta's Mesh generated in Ansys Fluent.*

7. CFD Analysis of the Final Design

7.1 Front-wind analysis

To begin with, the front-wind analysis will be conducted in order to get the data of the aerodynamical behaviour of the *Saeta* at 100 km/h (27,78 m/s), then some illustrations to scrutinise the causes and consequences of several phenomena will follow.

Since the previous version of the Velomobile was optimised mainly for front-wind performance, and this redesign is made to have a more stable front and side performance, the results obtained can actually exhibit an efficiency decrease in some parameters.

7.1.1 Analysis outcomes

Velocity

To see exactly how the airflow behaves around the new shape, the most standard values must be observed. In this case, the information about velocity of the wind flowing near the surface of the velomobile is paramount. As the chart in Figure 7.2 shows, there is a noticeable difference of 5 m/s in the peak velocity reached by the airflow between the *Wingvelo* and the *Saeta*, being the *Saeta* the one with a lower airflow peak velocity. This difference supposes a decrease of a 13,68% on the maximum velocity reached by the airflow, which translates in a reduction of skin drag and shear stress consequently. An increment of the velocity can also induce more lift depending on the shape of the vehicle and cause the fairing to be lighter the faster it travels. However, since the drag value has far more influence in the energy needed to drive the velomobile, is this data, compared to the other side- and diagonal-wind data, what is going to shape the way the redesign is evaluated.

On the other hand, the fact that the initial velocity does not differ much from the maximum velocity is a good indicate that there is not a zone reaching extreme velocities, where the boundary layer gets detached immediately and therefore creates a turbulent, energy-wasting wake.
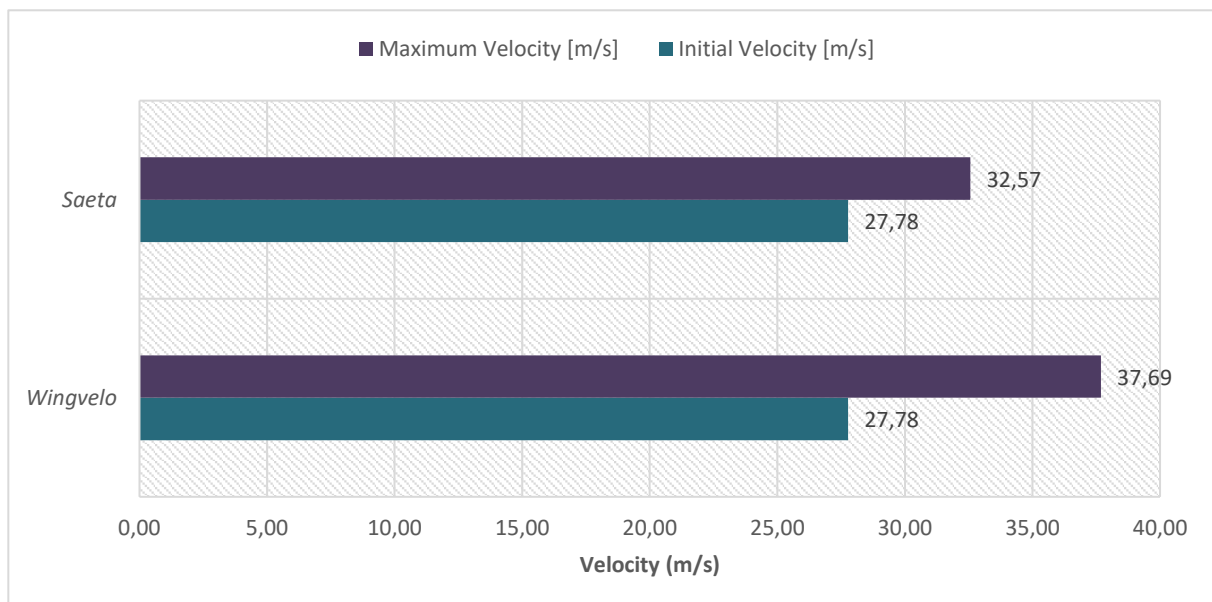
*Figure 7.2: **Peak Velocities Comparison**: Comparison between the initial and maximum velocities of the Wingvelo and the Saeta.*

7. CFD Analysis of the Final Design

Additionally, as can be seen in the Figure 7.3, where both velocity contours of the *Wingvelo* and the *Saeta* are being compared, the maximum more noticeable zones of high-speed flow are in both cases the nose, the knee bulges and the canopy, whereas the zones of low-speed flow seen below are the nose and the tail. All those are the parts of the velomobile intended to be redesigned according to Figure 5.1, together with the rest of the velomobile parts shown in that diagram.
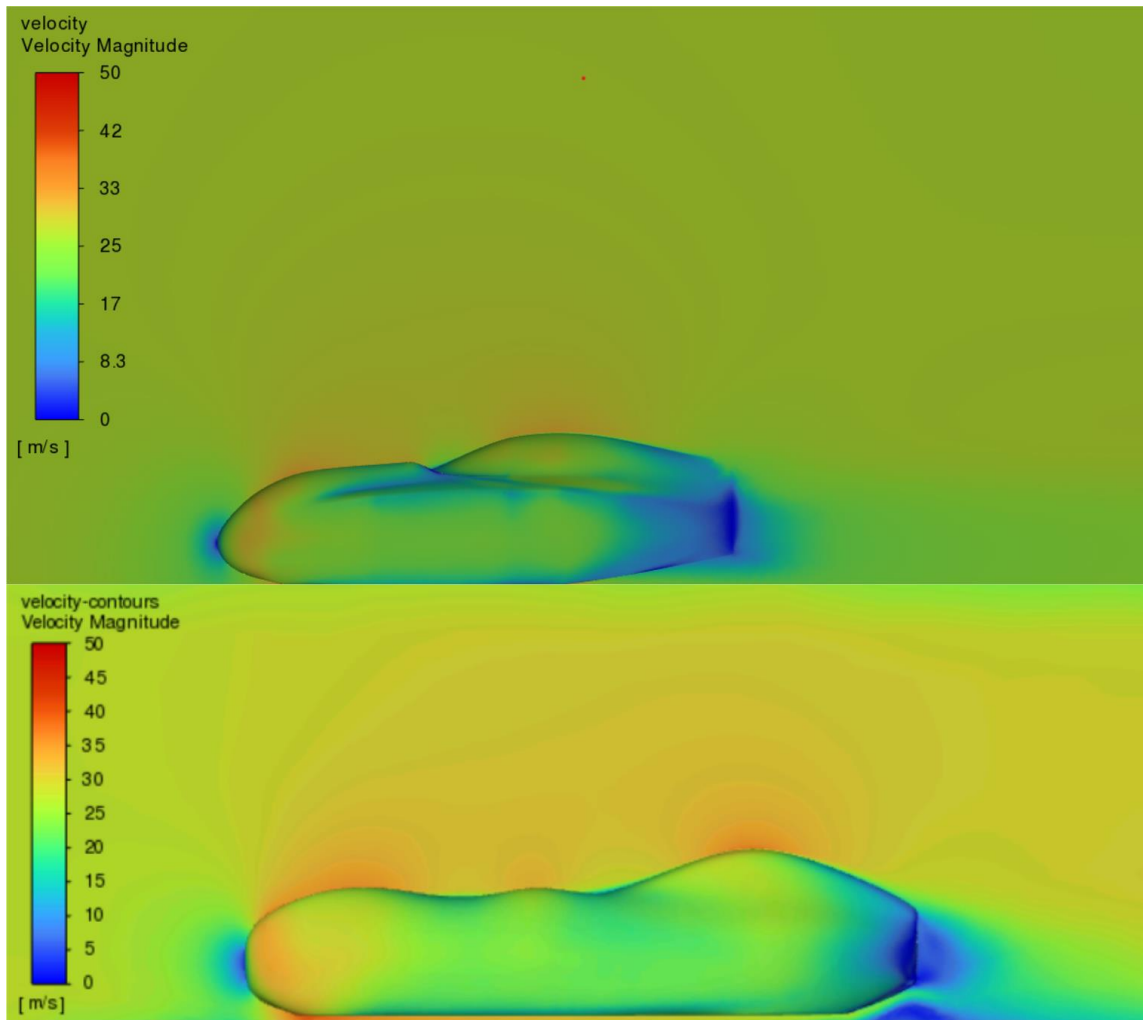
*Figure 7.3: **Velocity Contours Comparison**: Comparison between the velocity contours of the Wingvelo (top) and the Saeta (bottom).*

In the image above, as already mentioned, can be seen the main differences between both designs regarding the velocity of the flow. Whilst the *Wingvelo* has a more concentrated stagnation point at the nose, intensifying at the same time the forces on the same point, the *Saeta* distributes more the stagnation point, spreading the resistance forces around the nose surface. This can be beneficial on one side, since it spreads the pressure forces over more surface, but also counterproductive for the projected area of the nose, which has been increased for the *Saeta* design. Furthermore, between nose and feet bulges, the flow accelerates more in the *Saeta* design than in the *Wingvelo* due to the curviness of the surface, which makes the wind acquire a higher velocity. Nevertheless, according to the data shown in the chart from Figure 7.4, the lift obtained by the *Wingvelo* is substantially higher than the one from the *Saeta*. This outcome can be result of the larger quantity of surface from the *Wingvelo* compared to the *Saeta* where the velocity spikes and generates that extra amount of lift. Apart from that, another reason could be, that since the surface from the *Saeta* is smother and more streamlined, the lift generated by it is not as much as in the *Wingvelo*.

Moreover, the stagnation zone between the knee bulges and the windscreen mentioned in Chapter 4.1, is not there anymore for the *Saeta* design, which benefits the new design allowing the airflow to pass without stalling and creating more drag. At the same level, on the sides of the fairing, the *Wingvelo* has a flat, edgy design, where the airflow gets slowed down and creates an unwanted variation of the flow speed right in the middle of the vehicle. This changes in speeds disturb the flow and later on, at the tail, the boundary layer starts a slow detachment caused by the narrow shape of the tail and the airflow disturbances.
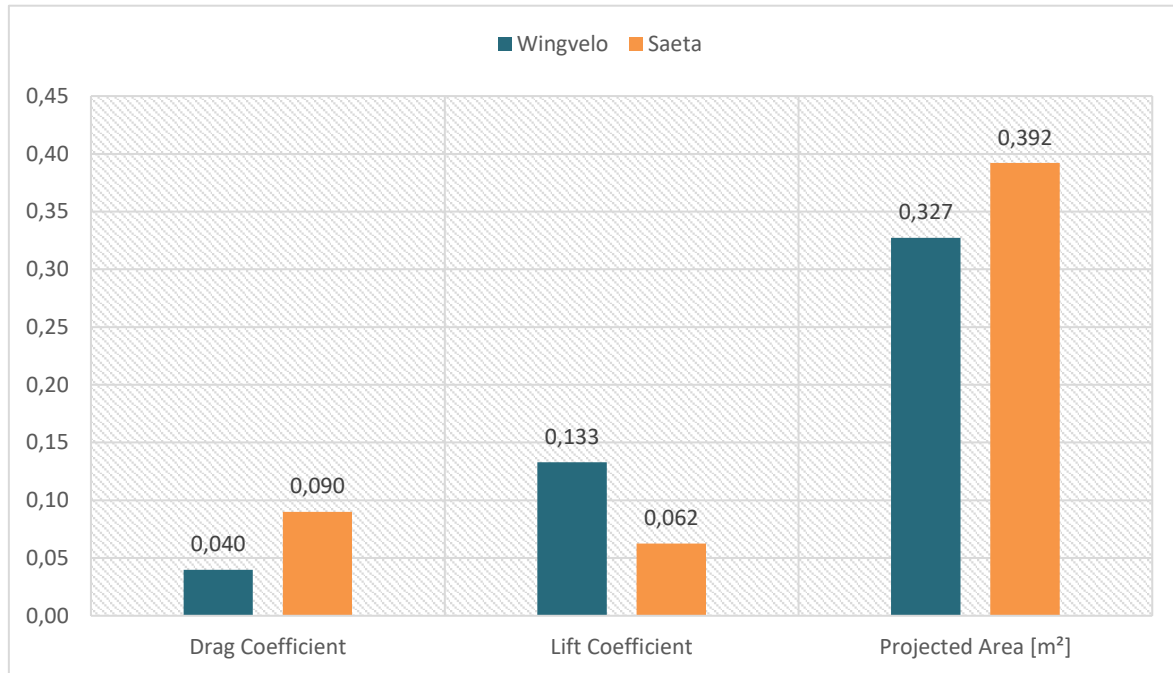
*Figure 7.4: **Drag and Lift Coefficients and Projected Area**: Comparison between Drag and Lift Coefficients and the Frontal Projected Area of both Wingvelo and Saeta designs.*

Conversely, the *Saeta* has a round, smooth shape, which benefits from having a regular, mostly unperturbed flow and a late detachment of the boundary layer. This is also accomplished by shifting the canopy position backwards and rounding the tail, making the flow stay further attached to the body and creating less drag. This blue area at the rear of the *Wingvelo* will also be noticeable in the shear stress contours from Figure 7.7. Moreover, in Chapter 8, a device to improve the boundary layer at the end of the vehicle will be introduced and explained.

Above, the Figure 7.4 shows the aforementioned trade-offs made to accomplish the side-wind improvements, sacrificing some of the beneficial characteristics from the front-wind aerodynamics of the *Wingvelo*. First, the Drag Coefficient (*Cd*) from the *Wingvelo* in front-wind conditions is half the *Cd* from the *Saeta*, due to the increase mainly of the Projected Area. Another modification that has probably influenced this parameter is the change of the shape of the tail, which can apparently be seen in Figure 7.3, since it has a more sudden curve at the end, creates a slightly bigger bubble of stagnant air at the rear, consequently provoking a larger drag. On the other hand, the lift generated is below the one generated by the *Wingvelo* as before mentioned, what will consequently make the velomobile lightly heavier.

The main advantage of having less lift generated is that the force transmitted from the wheels is going to be also higher. In overall, the Drag and Lift Coefficients have been affected by the change in the Projected Area, which the higher it gets, the worse it is for the overall performance. Since the current modifications are forcing the design to have a wider front

projected area to allow the airflow to have a smoother transit around the surface, it is unavoidable to finalise the design with the same or even lower Projected Area.

These outcomes do not only affect the Drag and Lift Coefficients, but also the general parameters of the vehicle such as the Drag Force, the Aerodynamic Efficiency, the Pressure values, etc. To be able to design an adequate velomobile, all these features must be considered. In this case, since the Thesis focuses mainly in achieving a better side-wind performance, the drawbacks now mentioned are meaningless compared to the possible improvements that can be done for side-wind conditions.
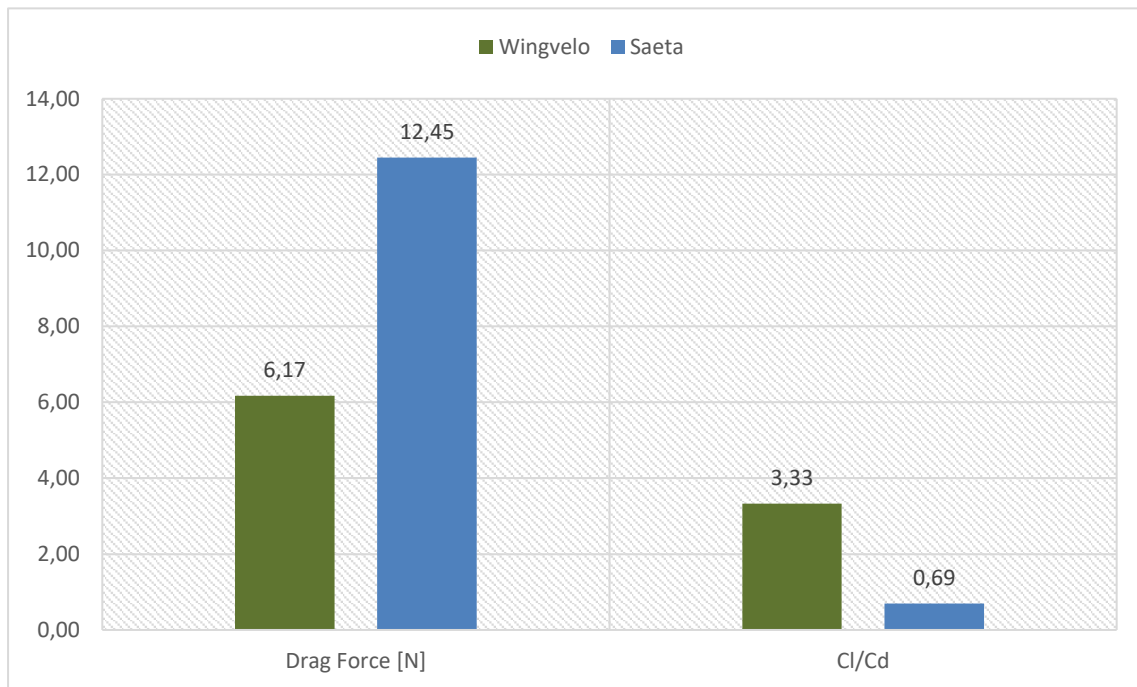
*Figure 7.5: **Comparison of Drag Force and Aerodynamic Efficiency**: Comparison of Drag Force to Aerodynamic Efficiency in both Wingvelo and Saeta designs.*

In the chart above (Fig. 7.5), the notorious difference between both Drag Force and Aerodynamic Efficiency of the *Wingvelo* and the *Saeta* is shown. Given the fact that the *Saeta* obtained a higher Drag and Lift values, is normal for the Drag Force to be affected by this outcome, meaning that the immediate changes in the Projected Area affect directly the Drag Force exerted on the vehicle, which in this case is doubled for the *Saeta* design. Even though the Drag Force becomes higher, the Aerodynamic Efficiency of the vehicle keeps being positive, which means the velomobile still is aerodynamic efficient in terms of drag and lift generated.

Pressure

For the pressure analysis, the pressure contour (Fig. 7.6) is used to observe how the different parts of the vehicle behave with the interaction of the airflow. Since the velocity and the pressure repercuss in similar ways on the airflow around the vehicle, the contours obtained for velocity and pressure share also a similar aspect. Below can be seen how the pressure gathers at the nose of both vehicles, as this point is the stagnation point, which most of the times is found in front of the vehicle that is opposing the air direction. As already mentioned, the air stalled at the nose of the *Saeta* occupies a larger space, since the curvature of the nose is more pronounced than the *Wingvelo*. That forces the *Saeta* to have a bigger pressure zone at the nose than the *Wingvelo*, thus creating bigger opposing forces, as it has been shown in Figure 7.5. What is also noticeable is that the values of the pressure on the bulges and the canopy are lower

for the *Saeta* design, where the surface shape is smoother and more streamlined. That is provoked by the decrease in velocity over those zones and for that reason is also the Lift Coefficient lower in the *Saeta*.
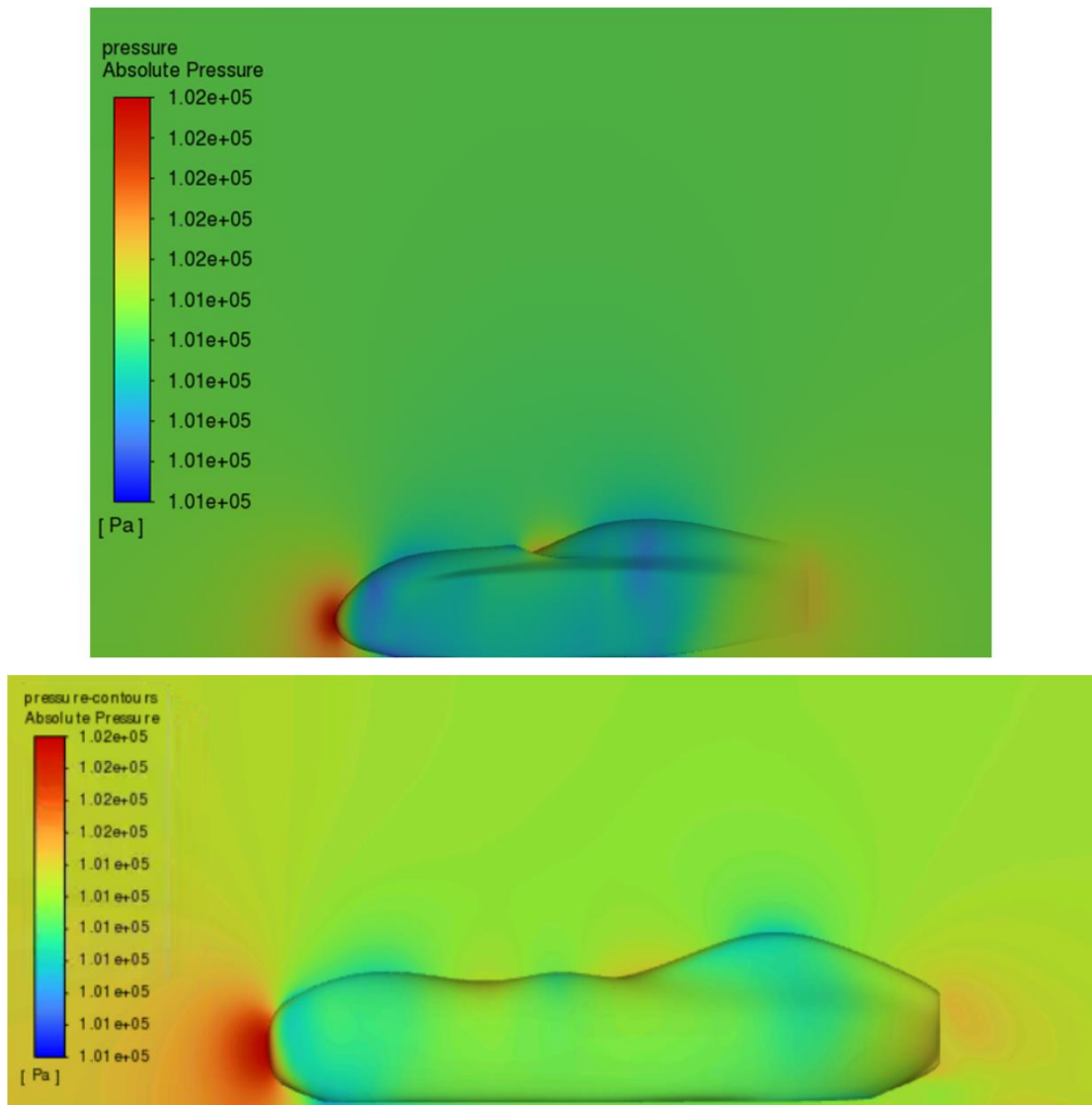
*Figure 7.6: **Comparison of Pressure Contours**: Comparison of the Pressure Contours between the Wingvelo and the Saeta.*

Additionally, since the bulges and canopy have been modified, there is a decrease in the pressure applied to those zones too. Furthermore, the smoothness of the design allows the vehicle to get rid of the stagnant air between the knee bulges and the windscreen, being this way more aerodynamic.

On the other hand, the same case applies for both versions of the velomobile, where the air is rapidly sucked in under the vehicle, which works as an unconventional *Ground Effect*. Also, at the rear of the velomobile, a slightly increased pressure zone can be seen in both cases, which is a representation of the turbulent wake being generated right at the end of the tail.

An important detail to consider, is that the blue zones shown in the pressure contours can be helpful to recognise the possible zones where can appear a boundary layer detachment. Even though at the nose, where there are also blue zones, there is no layer detachment, on the top of the canopy is most probably that there begins the boundary layer detachment.

7. CFD Analysis of the Final Design

Wall Shear Stress

As already explained in *Section 4.1*, the wall shear stress is a term used to describe the frictional force exerted by a fluid flowing over a solid surface. The velocity of the fluid influences directly the amount of shear stress existing on the surface and the higher is this shear force, the bigger is the velocity gradient difference between layers. This causes the boundary layer to detach when the velocity reaches a certain point at a certain part of the vehicle, where the surface has certain slope. These to facts combined provoke the boundary layer to lose energy and detach from the surface as shown in *Section 3.2.1 Bernoulli*.

In the image below, the analysis comparison of both wall shear stress contours for the *Wingvelo* and the *Saeta* illustrate how the modifications made to smooth the bulges and round the flat side surfaces, results in a lower shear stress in overall, reducing the frictional forces applied on the vehicle.
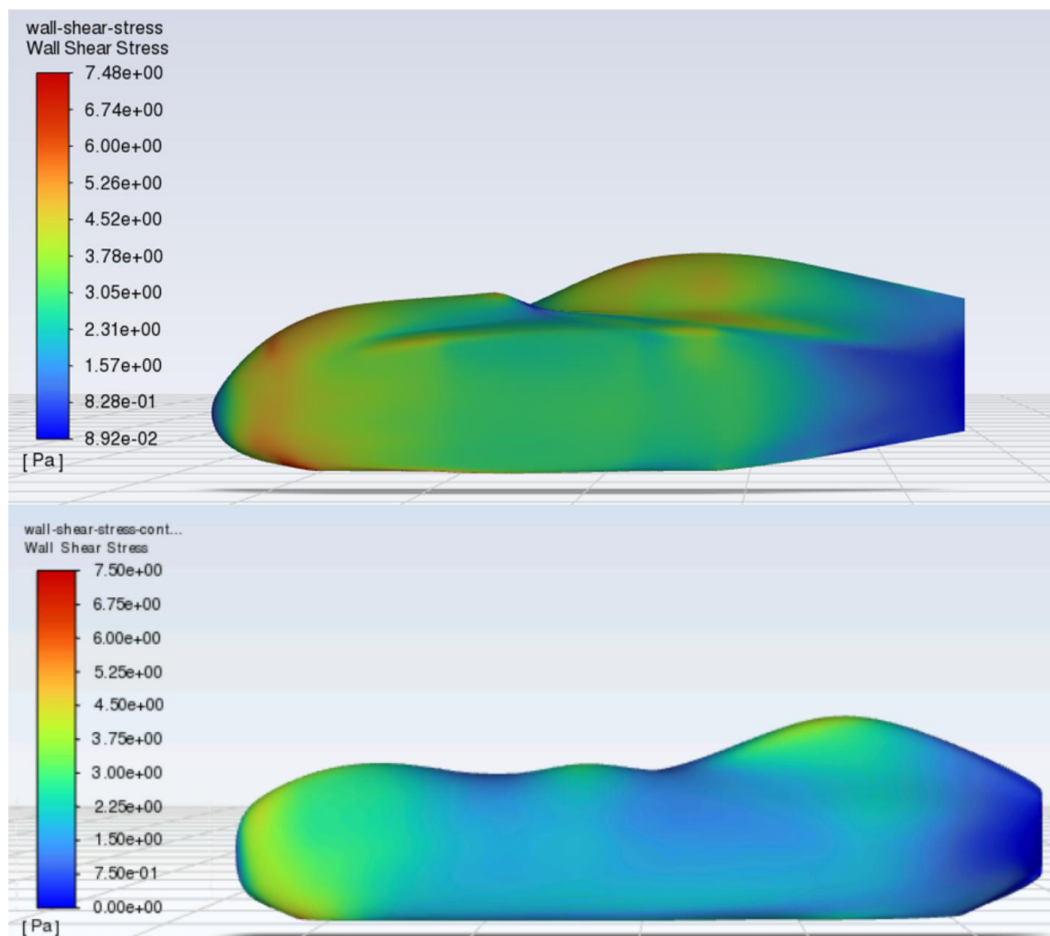
*Figure 7.7: **Wall Shear Stress Contours Comparison**: Comparison of the Wall Shear Stress Contours of both Wingvelo and Saeta models.*

Furthermore, since the canopy has been moved back and shortened, the shear stress coming from the acceleration of the airflow on the long canopy and the posterior narrowing of the tail, is now with the *Saeta* design improved, reducing the wall shear stress in most of the zones. The most worrying zone is the tail, where the flow unavoidably gets detached and, in both cases, the wall shear stress is reduced to minimums, making an allusion to the separation of the boundary layer.

Additionally, on the canopy of the *Saeta* an increment of the wall shear stress can be seen just before the slope of the surface varies, which can be also a reason of the separation of the boundary layer on top of the canopy.

7. CFD Analysis of the Final Design

7.2 Side-wind analysis

The side-wind analysis is mainly the most important analysis of this Thesis together with the diagonal-wind analysis, since the main objective of this Thesis is to optimise the new design for side- and diagonal-wind conditions in order to improve the stability and manoeuvrability of the velomobile. With the results obtained in the previous analysis made to the *Wingvelo* and the following, it will be possible to compare both designs and observe how the modifications implemented are working with the flow conditions.

Furthermore, the comparison will be also insightful enough, to see what changes can be applied to the *Saeta* design in order to further improve the aerodynamics of the vehicle. However, since the *Saeta* design has also flaws, the totality of it will not be used for future prototype implementations, but only the most useful features that can contribute more in other velomobile versions.

7.2.1 Analysis outcomes

Velocity

For this particular case, the airflow is coming from the side at 30 km/h (8.33 m/s), simulating the wind blowing at the street against the fairing of the velomobile. The picture below (Fig. 7.8) shows the velocity contours of the *Wingvelo* and the *Saeta* from the leeward and windward perspective. The first characteristic to consider is that the velocity the airflow acquires in the *Wingvelo* is lower on the knee bulges than in the *Saeta* due to the round shape of the *Saeta* side surface. The curvature of the sides allows the airflow to adapt better to the change of slope and accelerate as it travels around the fairing. At the same time, the flow sticks further to the surface, following the curvature of the knee bulges, and reattaches to the airflow that is travelling through the middle of the bulges, between feet and knee bulges. This benefits the vehicle by creating more lift on those zones, while also reducing the stagnation point over the whole side face thanks to the round shape of the side surface.
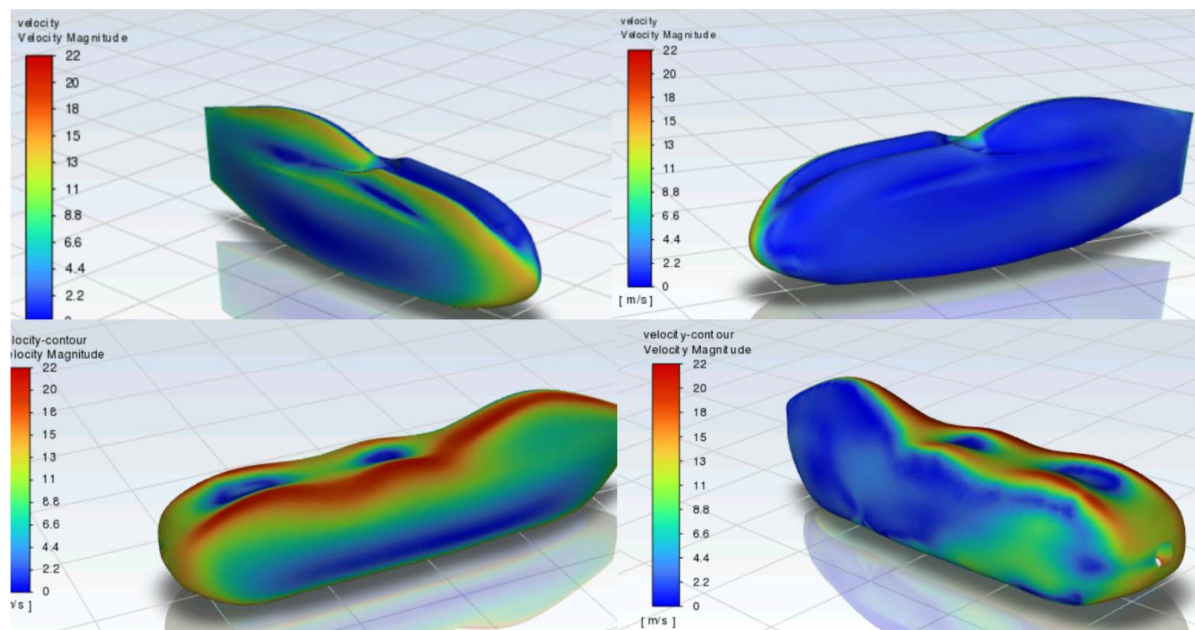
*Figure 7.8: **Velocity Contours Comparison**: Comparison of the Velocity Contours of the Wingvelo (top) and the Saeta (bottom) designs (leeward: left, windward: right).*

Another improved feature is the form of the bulges, which is now separated in two (feet bulges and knee bulges), allowing the pass of the airflow between them facilitating the flow mixing afterwards and keeping it attached, reducing the size of the turbulent wake.

7. CFD Analysis of the Final Design

On the right bottom side of the image, the S*aeta* has an irregular contour showing the surface affected by the turbulent wake. Even though it is not efficient to have a turbulent wake disturbing the flow near the surface, the difference of the side projected area in comparison to the *Wingvelo* is not influencing the overall aerodynamic parameters. Conversely, the shape of the side surface is what really reduces the forces exerted on that zone and also makes the windward side of the velomobile keep the airflow attached to the surface enough, so that the wake is considerably reduced in size.
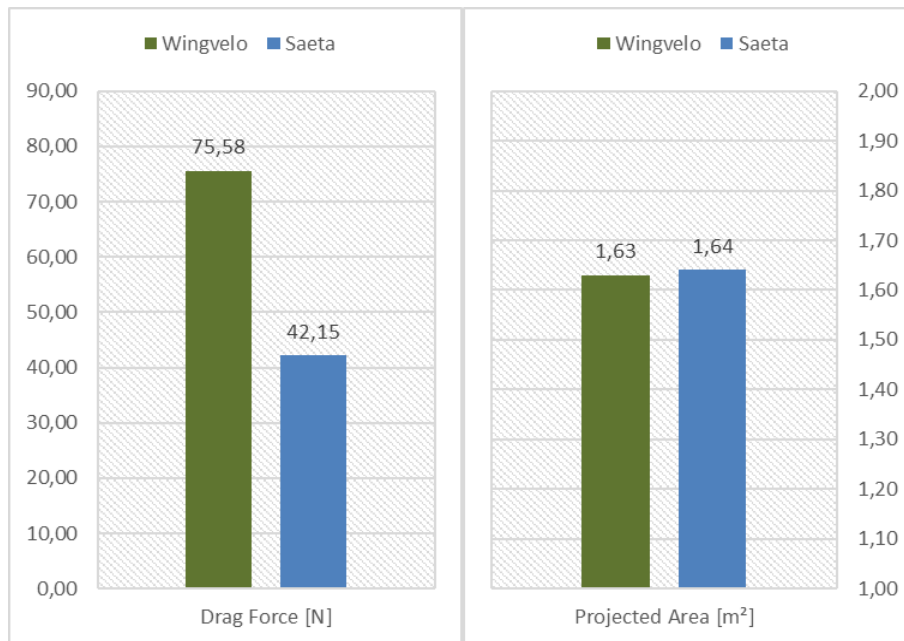
Figure 7.9: **Drag Force and Projected Area**: *Comparison of Drag Force and Projected Area of the Wingvelo and the Saeta.*

On the other hand, as already mentioned, the dimensions from the *Saeta* did increase from the front view, but they also increased for the side profile (Fig. 7.9), what normally translates into a higher pressure and force in overall. However, taking the optimisation of the side aerodynamics a step further, due to how is the side surface designed, the Drag Force on the side is almost half of the *Wingvelo*'s Drag Force, favouring this way the *Saeta* design for the side aerodynamics.

Velocity streamlines

The streamlines, or pathlines, can be very helpful to analyse how the airflow behaves after leaving the fairing. In this case, the observation of the wake is paramount, since what more energy loses creates is the wake that creates all the drag behind the vehicle. Normally, in other examples like in the Formula 1, the wake is dramatically big, since the power output of those cars is enough to overcome the amount of drag created, which also influences the cars chasing behind the others. Nevertheless, for a human powered velomobile, the power output is limited to what the person inside can generate and the transmission of the velomobile's gears. Given that fact, the wake is an important characteristic to consider when analysing the aerodynamics of a vehicle. For side-wind analysis, the wake is going to influence the manoeuvrability and the stability of the velomobile the most, which are two important features to take into account when driving on the street.

7. CFD Analysis of the Final Design

Below can be seen a comparison between the streamlines of the *Wingvelo* and the *Saeta*, where in both cases a considerable wake is developed at the windward side of the vehicle.
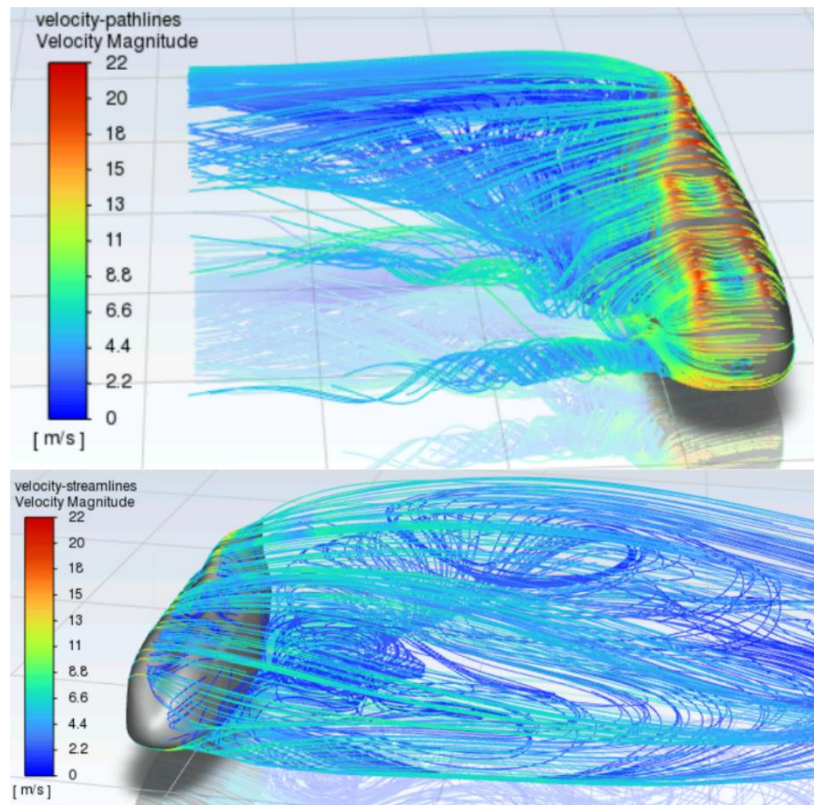
Figure 7.10: **Wake Comparison**: *Comparison of wake created in both designs with the velocity steamlines. (Top: Saeta, Bottom: Wingvelo)*

In this plot can easily be seen how the wake generated behind the *Wingvelo* design (bottom) is substantially bigger than the one created by the *Saeta*, which is in fact, adhered to the side surface until it totally detaches once it arrives to the canopy part, where most of the boundary layer is separating. Furthermore, how the wake behaves is also important and as the Figure 7.10 shows, the eddies created in the wake from the *Wingvelo* are chaotic, leading the wake backwards as explained in *Chapter 4.2* and also enlarging the wake even more. Instead, the wake from the *Saeta* stays sticked closer to the vehicle and then detaches perpendicularly from it following the direction of the coming wind, thanks to the round and smooth shape of the tail, that allows the wind to surround easily the vehicle and guide the detached boundary layer in the same direction.

One problem the *Wingvelo* had, was the stagnant air between the knee bulges and the windscreen, which made the wake be even more turbulent. In the redesign, since the knee bulges have been rounded and the space between them and the windscreen has been flattened and smoothed, the air is not stalling in that zone anymore, allowing the wake to be less turbulent.

7.   CFD Analysis of the Final Design

Pressure

The pressure contours shown in Figure 7.11 allows to visualise how the pressure is distributed along the surface, which can be very useful to know where more energy is applied on the vehicle. As already stated, the wind hits the side of the velomobile applying there the maximum pressure captured in the analysis, which then is spread around the side decreasing progressively once it arrives the bulges and canopy. The difference between the *Wingvelo* and the *Saeta* is that the pressure difference in that zone (bulges and canopy) is lower for the *Saeta*, since the airflow on that region is faster (*Bernoulli*'s *Principle*). Once the air has pass over the vehicle, travels to the other side of it, and for the *Wingvelo* the air detaches immediately without even reaching the second bulge, leaving the whole windward side of the vehicle with the same pressure magnitude. However, the pressure observed on the *Saeta* varies as it travels through the bulges, increasing between the left and right bulges. The advantage of the *Saeta* design is that, since the pressure sinks on the second bulge, the flow stays attached to the surface and gets adhered all over windward side, where the wake, as shown in the velocity streamlines (Fig. 7.10), flows to the rear until it gets dragged by the wind coming from the tail.
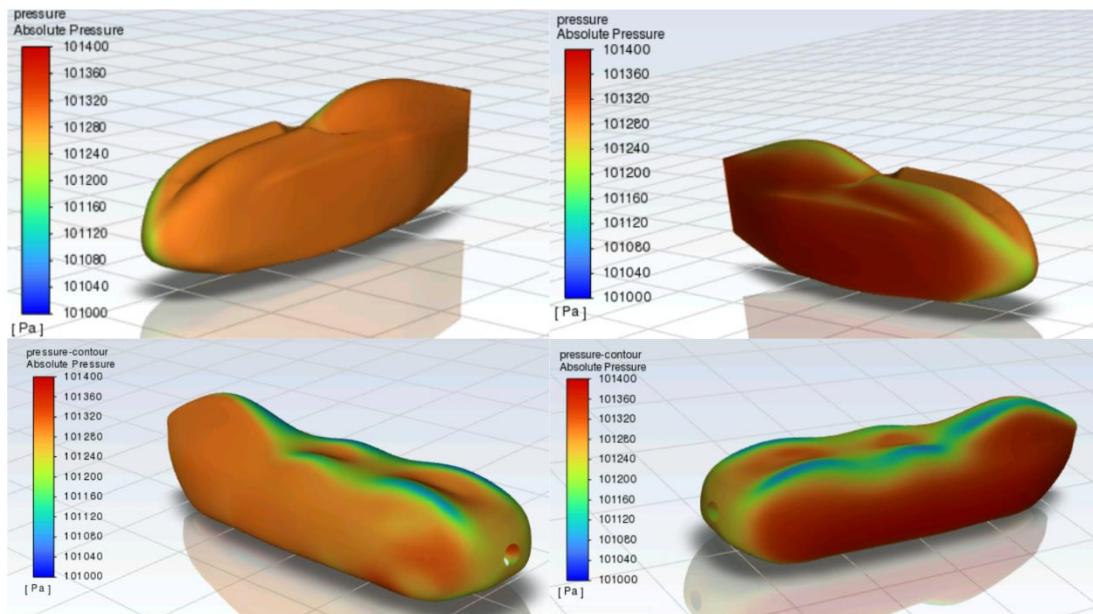
*Figure 7.11: **Pressure Contours Comparison**: Comparison of the Pressure Contours of the Wingvelo and the Saeta.*

In overall, the simple implementations made in the *Saeta* like the round side surfaces and the modifications in the bulges are enough to make a difference. Nonetheless, the rounded tail makes it easier for the flow to allow the wake to stay straight in the same direction and keep it stable and smaller than in the *Wingvelo*.

In this plot is observable how a simple change of 300 Pa in the pressure, can make the airflow separate from the surface, creating a turbulent flow and developing into a chaotic wake, which also translates into an inefficient aerodynamic design. Those considerations are necessary to narrow down modifications made that are truly beneficial for the design, since these will be later more closely analysed and brought to a new prototype with other modifications.

7. CFD Analysis of the Final Design

7.3 Diagonal-wind analysis

Finally, the diagonal-wind condition sets the velomobile in a position where the wind is blowing against the vehicle, but from an angle of 45º. This analysis will allow to see how the *Saeta* modifications help the vehicle be more stable and manoeuvrable in a situation of these characteristics. Since the vehicle will travel at 100 km/h and the wind blowing against it diagonally will reach the 30 km/h, the sum of velocities would result in 121,21 km/h (or 33,67 m/s).

7.3.1 Analysis outcomes

Velocity

For this part of the analysis, it will be measured how the vehicle behaves at the mentioned velocity, considering the different aspects of the aerodynamics and the modifications done to the original design. Comparing both models will be paramount to see the main benefits of the new prototype, as well as the drawbacks of changing features that already benefited the diagonal-wind aerodynamics. Furthermore, since the previous aerodynamic analysis made to the *Wingvelo* at 22,5º and 45º was helpful to see the key features of the original design that were failing, in this analysis will be only conducted the most unfavourable option observed in the previous test, which was the 45º, since it created more difficulties for the *Wingvelo* to overcome.

In the following chart (Fig. 7.12), the initial velocity starts as told, 33,67 m/s, scaling to an amount of 81,09 m/s for the *Saeta* and an even larger value of 84,74 m/s for the *Wingvelo*. Those values have not a big difference between them, but as commented in the pressure chapters before, the faster the air moves around the vehicle, the lower the pressure gets and the more unstable the boundary layer becomes, which in overall is not what is sought for this vehicle. Additionally, the values of velocity obtained from the airflow on the *Saeta* are lower even though the projected area is larger, just because the surface of the *Saeta* is smooth enough to allow the airflow travel through easily and not having to go around the bulges the *Wingvelo* has. However, as can be seen in Figure 7.14, the airflow on the *Wingvelo* accelerates more than on the *Saeta* endangering this way the integrity of the boundary layer at those areas.
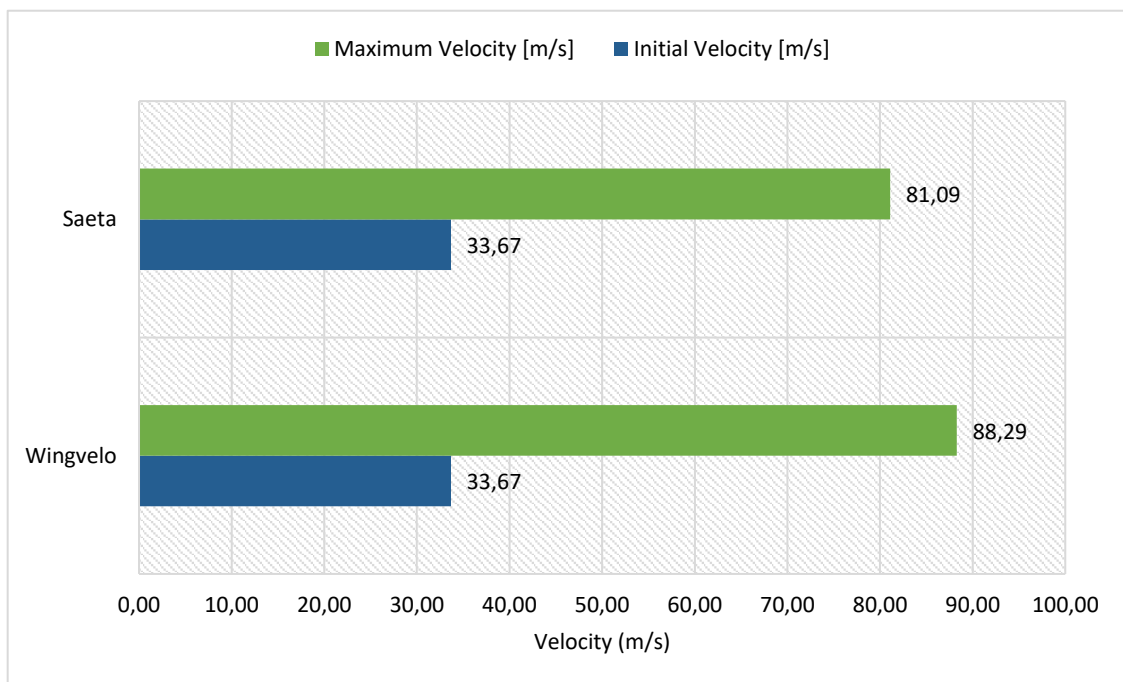
*Figure 7.12: **Initial and Maximum Velocity Comparison**: Comparison of the Initial and Maximum Velocities of the Wingvelo and the Saeta.*

7. CFD Analysis of the Final Design
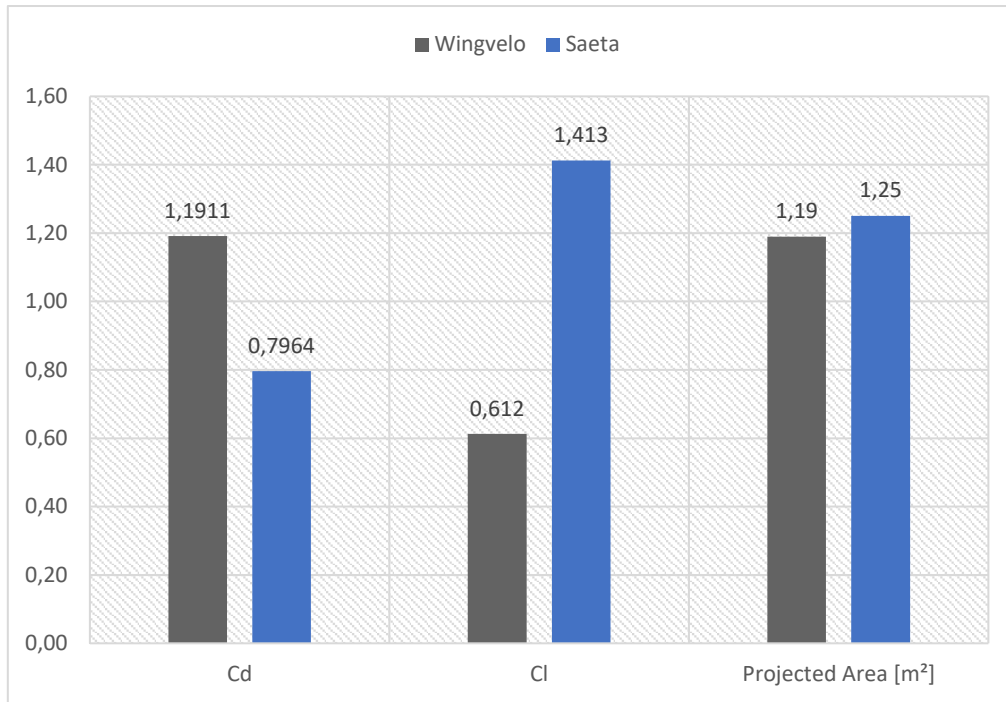
*Figure 7.13: **Drag and Lift Coefficients compared to Projected Area**: Comparison of the Drag and Lift Coefficient Values against the Projected Area of the Wingvelo and the Saeta.*

The *Wingvelo*, characterized by a drag coefficient of 1,1911, indicates a relatively higher resistance to aerodynamic forces, which is crucial in evaluating the air resistance experienced by the velomobile in motion. Additionally, the lift coefficient of 0,612 denotes the force perpendicular to the direction of motion, reflecting the aerodynamic lift generated by the vehicle.

In contrast, the *Saeta* model exhibits a markedly lower drag coefficient of 0,7964, reflecting the more streamlined shape encountering less resistance from the air. The lift coefficient of 1,413, on the other hand, signifies a higher generation of lift compared to the *Wingvelo*. This elevated lift coefficient may contribute to improved stability or handling characteristics, depending on the specific design considerations or the specific situation of the velomobile.

Furthermore, the projected area, a fundamental parameter indicating the effective cross-sectional area exposed to oncoming air, varies between the two models. On one hand, the *Wingvelo*, with a projected area of 1,19, presents a slightly smaller frontal area compared to the *Saeta*, which has a projected area of 1,25. This difference may influence the overall aerodynamic performance, since a smaller projected area generally contributes to reduced drag. However, given the fact that the *Saeta* has a smoother fairing design, the drag generated by it is lower in comparison to the *Wingvelo*.

These differences can be better seen in the next image, where the velocity contours are observed from both leeward and windward points of view. This is useful to visualise how the velocity increases in certain areas of the fairing, creating more lift or generating more drag, depending on the zone being observed. Moreover, the velocity contours are also helpful to see the how the modifications implemented in the *Saeta* solve some of the issues found in the *Wingvelo*, such as the stagnation between bulges and windscreen, the flat surface; which stalled the air and created a big pressure zone on the side destabilising the velomobile, or also the bulges themselves; which accelerated the air to a point where endangered the boundary layer integrity.

7. CFD Analysis of the Final Design

*Figure 7.14: **Velocity Contours Comparison***: *Comparison of the Velocity Contours of the Wingvelo and the Saeta.*

As mentioned before, the red painted areas on the velomobile are where the velocity value spikes and there is a possible case of boundary layer detachment due to the 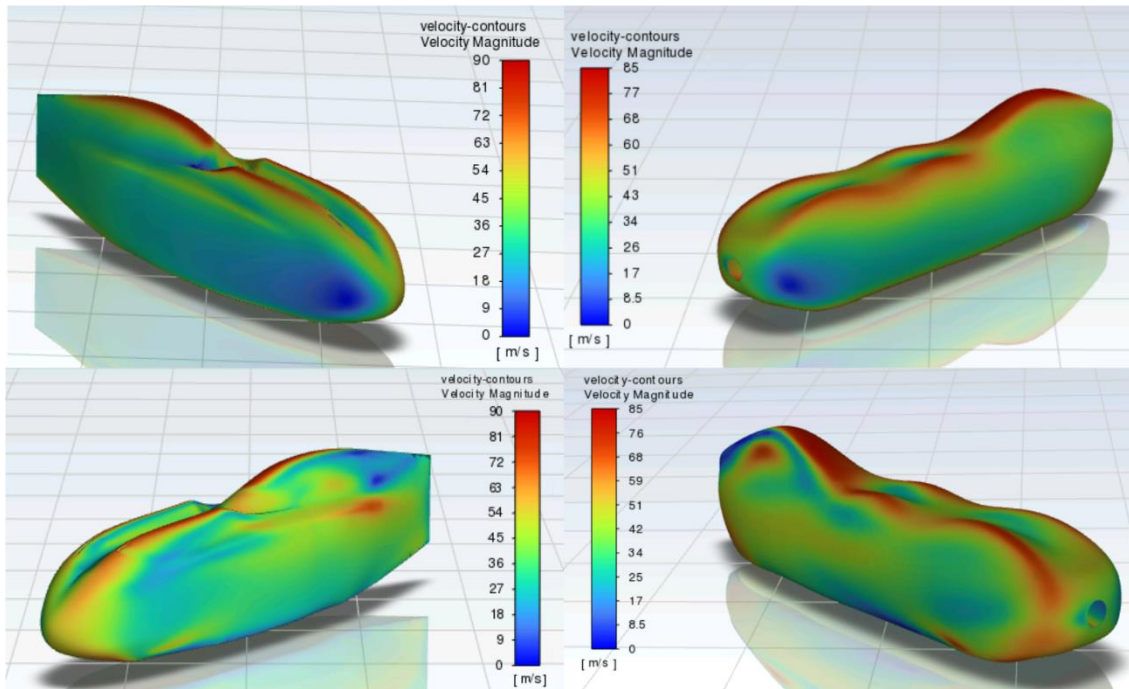difference of velocities between the outer layers and the boundary layer. In the *Wingvelo* the airflow hits the fairing creating a stagnation zone on the nose in the diagonal direction. The same case happens for the *Saeta*, but instead, the stagnation zone is decreased and less spread along the side surface of the vehicle, since the round shape of it accelerates faster the fluid avoiding its stalling. Now that the bulges have been smoothed and separated into two pairs, the airflow easily flows between bulges and doesn't struggle to surpass them like in the *Wingvelo*. As explained in the previous analysis of the *Wingvelo*. The airflow trapped between the bulges (in the valley), created a slower travelling flow that ended in the bubble of stalled air between bulges and windscreen. This made the air coming from 45° to be slowed down and generate more drag when it finally was dragged out of the low-pressure zones that where the stalled air bubbles.

Additionally, the fact that the bulges are now more rounded allows the flow to accelerate progressively and not instantly like in the *Wingvelo*, offering a better adaptation to the velocity changes and facilitating the airflow to increase its velocity without separating from the surface.

Apart from that, the flow travels further along the vehicle until it reaches the canopy, where it accelerates dangerously compromising the stability of the boundary layer and then suffers a sudden change in the slope of the surface, what consequently forces the boundary layer to detach and create a turbulent wake. This situation happens on both models, but what the changes made on *Saeta* facilitate is that the wake behind the vehicle is smaller and it stays near to the body instead of separating and travel turbulently far from the fairing. This is thanks to the modification on the bulges, where the airflow passes over them and stays attached to the surface until it arrives to the canopy part, where it gets dragged by the rest of the airflow coming from above the canopy. This phenomenon can be better observed in the velocity streamlines from Figure 7.15, where the estimated trajectory of the air particles is drawn and visualised travelling around the velomobile.

7. CFD Analysis of the Final Design

To be able to visualise how the flow behaves when entering in contact with the vehicle, the use of streamlines tracking the particle trajectory is paramount. This approximation of the path an air particle has helps observe how the airflow interacts with the bulges, for example, in order to be easier to analyse how the modifications influence the current and previous design.
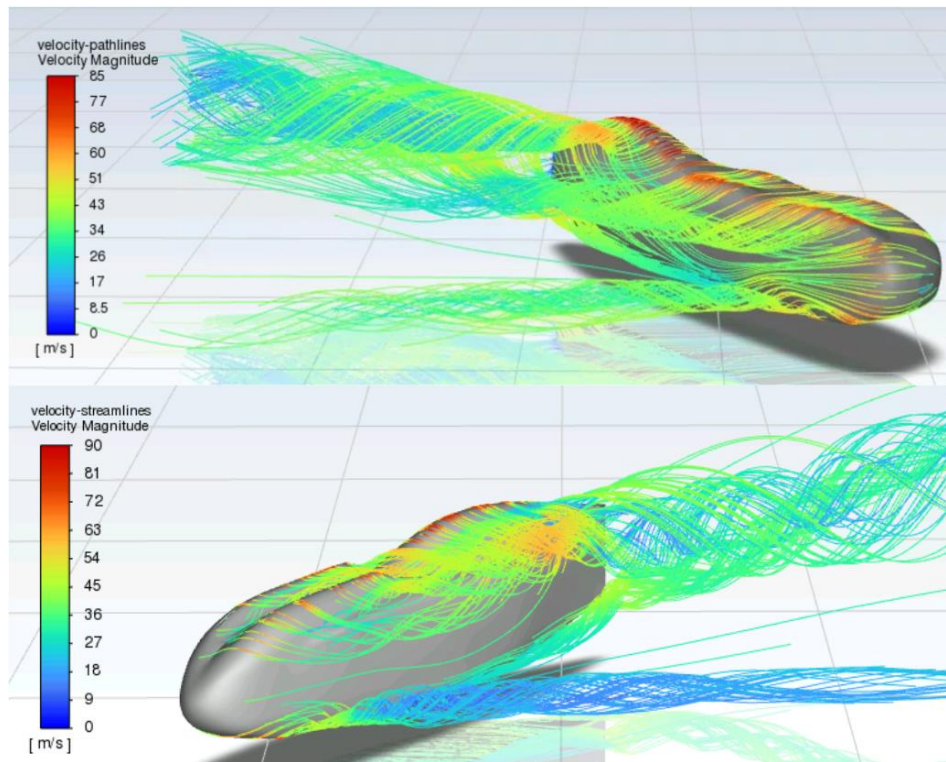
Figure 7.15: **Velocity Streamlines**: *Comparison of the Velocity Streamlines of the Wingvelo and the Saeta.*

For the past model, the *Wingvelo*, the airflow travels around the nose detaching suddenly after surpassing the bulges as mentioned previously. This phenomenon occurs due to the sudden change in the surface slope and the high velocity achieved by the fluid on that zone, reaching almost the 90 m/s. Then, the wake generated by the airflow on the bulges gets unified by the turbulent wake unavoidably created on the canopy and consequently reinforces even more the existent turbulent flow behind the velomobile. Furthermore, the fluid velocity decreases as it introduces between the bulges, slowing down and creating a turbulent zone, where the flow gets disturbed and redirected towards the windscreen (it can be seen from another perspective in Figure 4.16). This sluggish airflow then is rapidly dragged out from between the bulges and reunited to the large turbulent wake. On the other hand, since the side leeward surface is flat, the flow does not circulate around the velomobile and it creates a low-pressure zone behind the vehicle, just on the windward side of it. This forces the airflow separating from the bulges, which has a higher pressure, to go to the less pressure zone, but due to the high velocity and energy it transports, the fluid concludes transforming into eddies with the same direction the previous airflow had.

For the case of the *Saeta* model, the wind comes from the same direction, surrounding the velomobile and then exiting the vehicle creating also an unavoidable turbulent wake behind it. Each body that is traveling to a certain velocity in a fluid will always have a wake behind it. It can be either a laminar fluid wake or a turbulent fluid wake, but when a body travels to a certain velocity, the aerodynamical forces make the body lose energy and this lost energy translates into temperature and turbulences (particles movement) among other types of energy. Nevertheless, the airflow travelling around the *Saeta* is not forcing the fluid to separate from

the surface right after surpassing the bulges, but instead is forcing it to keep attached to the windward surface thanks to the round and smooth surface, which contrary to the *Wingvelo* has a progressive change of slope helping the flow readapt to the velocity changes. Since the airflow is still near the windward side, the fluid travels to the rear of the vehicle, where is afterwards dragged into the turbulent wake due to the separation of the boundary layer on the canopy of the vehicle.

In this comparison can be seen, how in both designs, whichever it is the shape of the canopy, the boundary layer is easily separated creating a turbulent wake behind. This problem could be assuaged by applying modifications with some type of aerodynamic generators like the one mentioned in *Chapter 8*.

Pressure

Another analysis is the pressure contours, which can help identify and visualise better the mentioned areas where the airflow separates from the velomobile and see how the pressure affects the surface of the vehicle. As a first instance, the pressure contours from the *Wingvelo* indicate that the red zone (higher pressure zone) is all over the leeward side of the vehicle and then suddenly changes into a green area meaning a decrease of pressure of almost 3000 Pa. This immediate transition of the pressure gradients translates into an unavoidable separation of the boundary layer as already seen in Figure 7.15, due to the fact that the flow is no longer exerting pressure on the bulges, and therefore there is a lower pressure over that area. Furthermore, since the airflow gets introduced between the bulges, it can be seen how in that zone there is a higher pressure than the observed in the *Saeta*, because the turbulent flow contains more energy per definition. However, comparing the *Wingvelo* canopy with the *Saeta*, it can be seen how the design of the *Saeta* is not properly prepared to help the airflow adapt to the change in the surface slope and gets detached prematurely than in the *Wingvelo*. That could be mitigated by reducing the slope difference between the side face and the top face and also by installing aerodynamic control devices.

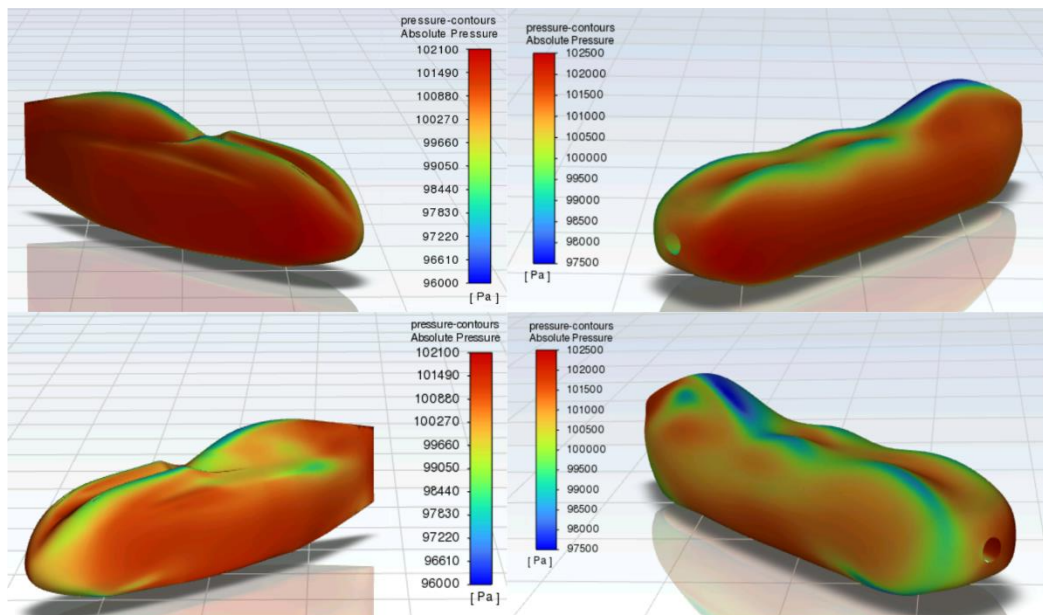*Figure 7.16: **Pressure Contours Comparison**: Comparison of the Pressure Contours from the Wingvelo and the Saeta. (Top: Leeward, Bottom: Windward)*

Another feature to mention is that thanks to the round nose of the *Saeta* at this velocity (compound velocity of front 100 km/h and diagonal 30 km/h = 121 km/h) facilitates the reattachment of the airflow surrounding it. It can be deduced by observing how the pressure on

the windward side of the nose decreases and then, along the rest of the windward side face, the pressure stabilises again, meaning that the airflow stays near the vehicle without creating a bigger wake like in the *Wingvelo*.

Wall shear stress

With this last part of the diagonal-wind analysis, the behaviour of the airflow can be reaffirmed. The wall shear stress contours will confirm the previous statements mentioned by showing the shear stress forces exerted on the surface when the velocity of the flow increments and the velocity difference of the layers increase among each other.

As Figure 7.17 shows, the top area of the bulges in both models is coloured with light green indicating an increase of shear stress, and with red colour between the bulges and the windscreen, where the velocity increases as it travels through a choke point with stalled air (Bernoulli's effect). In the *Wingvelo*, the higher shear stress area marked results to be the windward side face near the canopy, where the boundary layer starts to separate due to the turbulent airflow being unable to adapt to the sudden change in slope and the difference in velocity of the boundary layer and the outer layer of the side airflow and top airflow, among other reasons before mentioned.

On the other side, the *Saeta* higher shear stress value captured resides on the side of the canopy and on the windscreen, whereas seen in the streamlines plot, is exactly where the airflow starts to accelerate and then detaches due to the sudden surface change and previous acceleration.

In both cases, the canopy represents a great challenge to face, and is probably the biggest objective to accomplish for future prototypes of the velomobile.
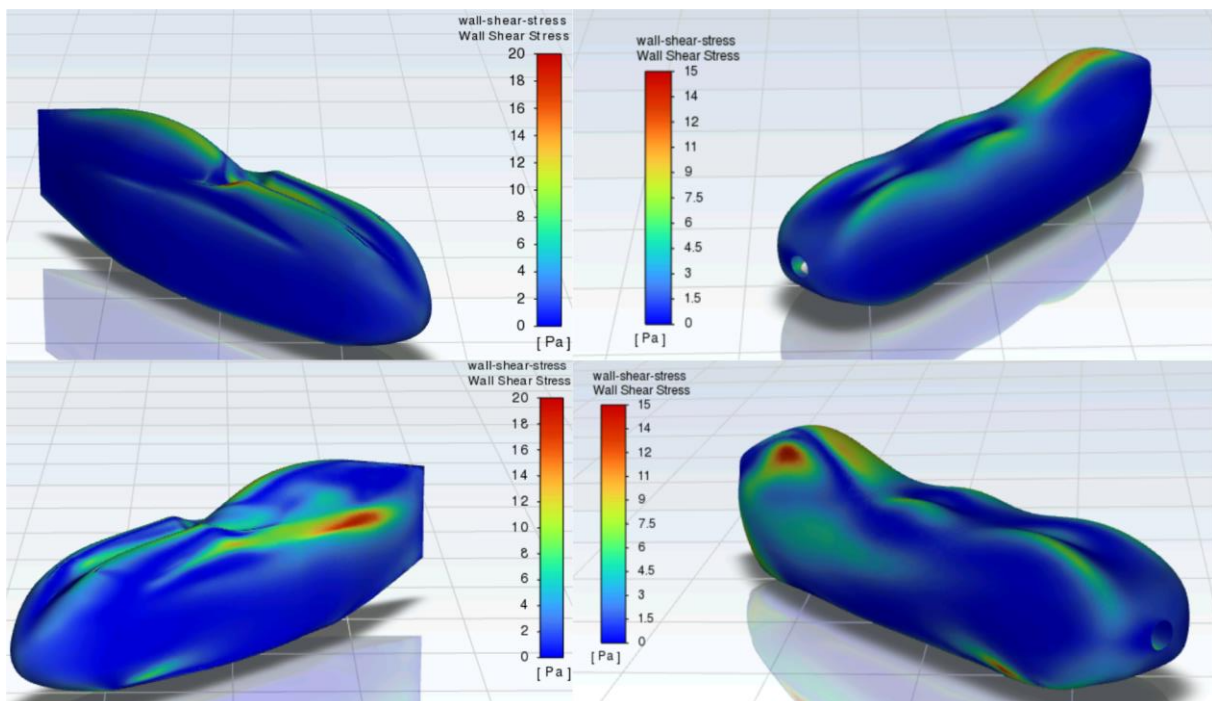

Figure 7.17: ***Wall Shear Stress Contours Comparison****: Comparison of the Wall Shear Stress Contours of the Wingvelo and the Saeta. (Top: Leeward, Bottom: Windward)*

8. Further Aerodynamic Improvements

Bearing in mind the fact that the final design does also have flaws, an improvement to avoid the flow detachment right on the canopy. This design modification has not been tested in the CFD program, since this type of implementations can be more accurately proven through an empiric wind tunnel test instead of a computer simulation.

Normally, when the boundary layer detaches itself from a body is because, inside the boundary layer, the viscous sublayer starts losing velocity caused by heat transfer or drag (among others), making the flow above travel faster than the one beneath, thus forcing the viscous sublayer to travel backwards provoking the boundary layer to detach. For this reason, below can be seen how a sphere-like texture on the canopy has been added perpendicular to the flow direction, to increase the turbulence in the boundary layer while also incrementing the energy it has. This will force the boundary layer to become turbulent in order to stay further attached to the body and increase the efficiency of the design.

Such type of aerodynamic flow control devices have also been seen in airplanes and cars as vortex generators. The device can adopt different shapes and sizes depending on the dimensions of the vehicle and the forces it is facing, meaning that each vortex generator can have a countless number of variations depending on the real shape of the vehicle, that is why the data obtained from wind tunnel with these types of designs is more reliable than the computer-generated results.

Some practical examples where the vortex generator can be used is the wing of an airplane to keep the airflow further attached on the wing, or in a front wing of a Formula 1 car to make the airflow avoid the main body and wheels.

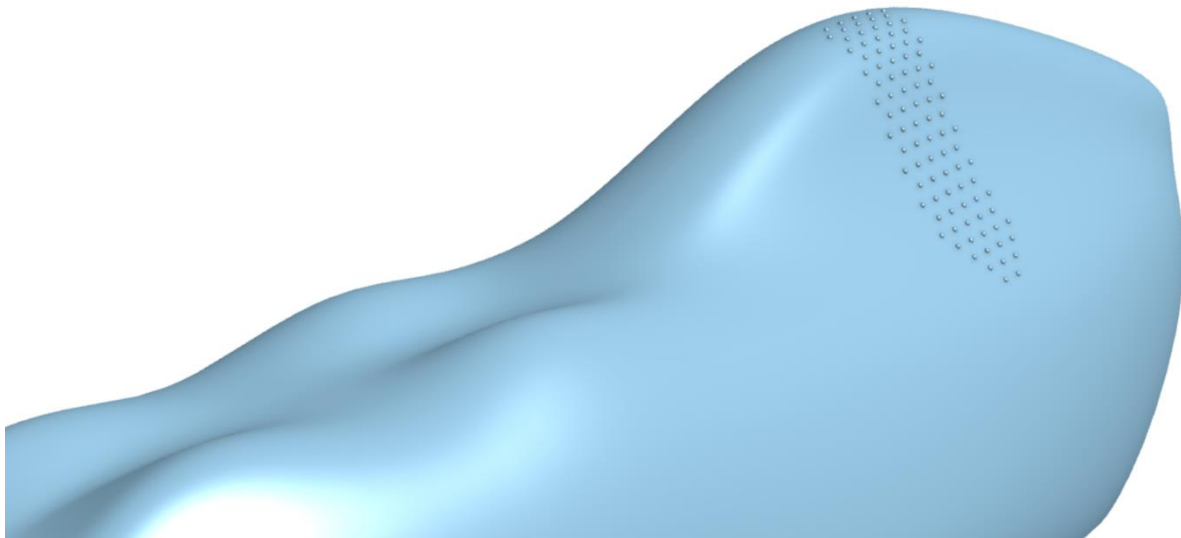*Figure 8.1: **Vortex Generators**: Close-up image to the sphere-like vortex generators on the canopy.*

In a physical prototype the vortex generator can be chosen depending what is more suitable for the manufacturing process and the installation of these devices on the canopy. This is the innovative part which can vary the most, because it is completely an experimental process of proof and error.

9. Conclusion

9.1 Summary of findings

The aerodynamic analysis of the velomobile models under different wind conditions has yielded valuable insights into the flow behaviour and characteristics around the vehicle. Since the primary objectives of this analysis were to find the design flaws of the *Wingvelo*, to redesign it to improve its side aerodynamics and to suggest further improvements to the *Saeta*, the overall results of the Thesis have been conclusive.

The *Wingvelo* design needed modifications in several parts like the nose, the bulges, the width of the vehicle and tail and the tail itself and analysing it under different wind conditions helped visualise in which way was the redesign going to be, to be able to avoid previous design errors, commit new ones and to create a better aerodynamically balanced prototype.

Nevertheless, even if in the design process has been considered every *Wingvelo*'s design flaw, the final results need to be tested to confirm the theory (and then double test it in a wind tunnel and on the street), which is why is paramount to proof the designs suggested in a proper environment with a physical model. Moreover, as explained in the Thesis, the *Saeta* also has its designs flaws which can be solved either by changing the design in those specific parts or to adding aerodynamic control devices.

The final redesign named *Saeta* showed several improvements over the *Wingvelo* such as the modification of the bulges, which have been separated into to pairs of bulges, knee bulges and feet bulges, leaving a space between them to let the air pass through and to keep the vehicle more aerodynamic from a side-wind perspective. The sides' shape has also been rounded, since the flat surface of the *Wingvelo* created a big opposition to the wind, allowing the airflow to surround easily the vehicle and keeping the flow further attached to the windward surface.

Additionally, the tail has also been smoothed, which in comparison to the *Wingvelo*, that has a flat tail, the airflow on the *Saeta* has an easier pass around it, keeping the airflow traveling in the same direction. This small fact is important, since for the *Wingvelo* the air was stalling on the surface due to its flat tail and, since the air on the nose was travelling faster than that at the tail, the wake was redirected to the back of the vehicle even though the initial wind came perpendicular to the fairing.

In overall, the *Saeta* design's purpose is to improve the side- and diagonal-wind aerodynamics from the previous design, which has been accomplished by losing some remarkable front-wind aerodynamic features. However, since the *Saeta* is not a definitive prototype, the useful modifications made in this model can be later implemented in other designs.

9.2 Further recommendations

The observation of the velomobile aerodynamic analyses presented in this bachelor thesis has shed light on crucial factors influencing their performance, particularly with regard to the boundary layer integrity, the drag and lift coefficients and the shape optimisation of the vehicle. The comparative analysis of the Wingvelo and Saeta models has highlighted the nuanced differences in their aerodynamic characteristics, providing valuable insights for future prototype improvements. In this case, one notable consideration for future velomobile design

9. Conclusion

enhancements is the potential adoption of a linear pedal drive mechanism, as opposed to the conventional circular pedal drive. This alteration not only addresses ergonomic concerns related to knee bulges, but also opens up new possibilities for streamlining the fairing by eliminating the protrusions associated with circular pedal drives, with which a sleeker and more aerodynamically efficient velomobile profile can be achieved, potentially reducing drag and enhancing overall performance.

Furthermore, the implementation of aerodynamic control devices, such as vortex generators, emerges as a key recommendation for optimizing velomobile aerodynamics. Vortex generators strategically placed on the velomobile's surface (like the placed mentioned in chapter 8 on the canopy) can manipulate the airflow, forcing the boundary layer to stay more attached to the surface. This modification is crucial in minimising separation of the boundary layer and reducing drag, ultimately contributing to improved stability and efficiency during the driving.

In conclusion, the aforementioned design optimisation opportunities offer promising avenues to enhance the aerodynamic performance of the velomobile across different wind conditions. By thoughtfully implementing these recommendations, the velomobile's drag forces and turbulence can be effectively reduced, and overall efficiency improved, contributing to a more manoeuvrable and efficient transportation solution.

References

[And98]	Anderson, J. D. (1998). A History of Aerodynamics: And Its Impact on Flying Machines. Cambridge University Press.
[Hoe65]	Hoerner, S. F. (1965). *Fluid-dynamic Drag: Practical Information on Aerodynamic Drag and Hydrodynamic Resistance*. Hoerner Fluid Dynamics.
[Dor22]	Dorsch, V. (2022). *Vehicle Dynamics, edition 2.2* [Lecture notes]. Ostfalia University of Applied Sciences.
[Huc87]	Hucho, W. (1987). *Aerodynamics of Road Vehicles: From Fluid Mechanics to Vehicle Engineering*. Butterworth-Heinemann.
[Fra08]	Franchini, S., & López García, Ó. (2008). *Introducción a la ingeniería aeroespacial*.
[Kat96]	Katz, J. (1996b). *Race car Aerodynamics: Designing for speed*. Bentley Publishers, a division of Robert Bentley, Inc.
[Ste22]	Stevanovic, N. (2022). *Entwicklung und Fertigung einer Leichtbaukarosserie mit CAD, CFD und einer 3D-Formen-Fräse* [Unpublished]. Institut für Konstruktion und angewandte Maschinenbau, Ostfalia Hochschule für angewandten Wissenschaften.
[Nie13]	Niedermeyer, P. (2013, December 12). *Automotive History: An Illustrated History of Automotive Aerodynamics – Part 1 (1899 – 1939)*. Curbside Classic.https://www.curbsideclassic.com/automotive-histories/automotive-history-an-illustrated-history-of-automotive-aerodynamics-part-1-1899-1939/
[Ocko]	Ocko, S., & Gacki, A. *Human-Powered Vehicles*. Encyclopedia.com. https://www.encyclopedia.com/environment/encyclopedias-almanacs-transcripts-and-maps/human-powered-vehicles
[WHPVA]	*World Human Powered Vehicle Association*. http://www.whpva.org/
[IHPVA]	*IHPVA - International Human Powered Vehicle Association Official Home Page*. http://ihpva.org/
[NASA22]	NASA Glenn Research Center. (2022, July 28). *Drag Equation - Glenn Research Center	NASA*. Glenn Research Center	NASA. https://www1.grc.nasa.gov/beginners-guide-to-aeronautics/drag-equation/
[NASA23]	NASA Glenn Research Center. (2023, January 21). *Drag - Glenn Research Center	NASA*. Glenn Research Center	NASA. https://www1.grc.nasa.gov/beginners-guide-to-aeronautics/drag/
[Ansys23]	*Ansys Academic*. (2023, April 17). https://www.ansys.com/academic
[Ansys19]	Ansys Inc. (2019, November 19). *Aerodynamics of a Solar Car	Ansys Course*. Ansys Innovation Space. https://courses.ansys.com/index.php/courses/aerodynamics-of-a-solar-car/

References

[ICIL]   Fundación ICIL. *(2010, December 3). Dispositivo aerodinámico de reducción de combustible y emisiones de CO2*. (2010, December 3). FUNDACIÓN ICIL. https://apoyologistico.wordpress.com/2010/12/03/dispositivo-aerodinamico-de-reduccion-de-combustible-y-emisiones-de-co2/

[Kal18]   Kaltwasser, G. & S. (2018). *Mochet-Simple is Beautiful*. Mochet. https://mochet.org/

[Szu22]   Szudarek, M., Piechna, A., Prusiński, P., & Rudniak, L. (2022). *CFD Study of High-Speed Train in Crosswinds for Large Yaw Angles with RANS-Based Turbulence Models including GEKO Tuning Approach. Energies*, *15*(18). https://doi.org/10.3390/en15186549

[San22]   Santamaría, L., Vega, M. I. Á., Pandal, A., González, J., Velarde-Suárez, S., & Oro, J. M. F. (2022). *Aerodynamic Performance of VAWT Airfoils: Comparison between Wind Tunnel Testing Using a New Three-Component Strain Gauge Balance and CFD Modelling. Energies*, *15*(24), 9351. https://doi.org/10.3390/en15249351

[Rum23]   Rumsey, C. (2023, May 1). *Spalart-Allmaras model*. NASA, Langley Research Center. https://turbmodels.larc.nasa.gov/spalart.html

[RaT23]   Ramon Torrens, A. (2023). *Analysis of a Human Powered Vehicle* [Unpublished]. Institut für Konstruktion und angewandte Maschinenbau, Ostfalia Hochschule für angewandten Wissenschaften.

[Haz96]   Hazlewood, R. (1996). *An Investigation of Cavity Vortex Generators in Supersonic Flow*. https://ntrs.nasa.gov/api/citations/19960020422/downloads/19960020422.pdf

[Ons01]   *Onshape Forums*. (2001, August 24). Onshape. https://forum.onshape.com/

[OnLearn]   *Onshape Learning Center*. (n.d.) Onshape Inc. https://learn.onshape.com/

[Onshape]   *Onshape*. (2013) Onshape Inc. https://cad.onshape.com/

[Hep14]   Hephaestus. (2014). *Graeme Obree's Beastie: The Lure of the Linear Pedal Drive*. https://lefthandedcyclist.blogspot.com/2014/07/graeme-obrees-beastie-lure-of-linear.html

[ATools]   *Airfoil Tools*. (n.d.). http://airfoiltools.com/

[BicEv]   Bicycle Evolution (n.d.). *Velomobile size comparison*. https://www.bicycle-evolution.com/index.php/new-home-page/velomobiles-2/velomobile-size-comparison/

[Roa22]   Roadrunner. (2022, June 9). *Velomobil Know How*. Velomobil.blog. https://velomobil.blog/en/about/velomobil-know-how/

[VeloMob]   *Zentrum für Velo-Mobilität*. (n.d.). https://velowerk.info/

[VanEi]   Van Eijk, B. W. &. M. (n.d.). *Velomobiel.nl*. https://en.velomobiel.nl/

References

[Cyc23] *Cycles JV Fenioux*. (2023, July 7). Fabricant de vélomobiles et vélocouchés. https://cycles-jv-fenioux.com/

[Car23] *Car Design Award*. (2023, March 9). https://cardesignaward.org/en/

[Roa18] Road Cycling UK (2018, March 6). *Endura launches "fastest ever" TT skinsuit and accompanying aero road clothing*. https://roadcyclinguk.com/gear/gear-news/endura-launches-drag2zero-aero-clothing-collection-including-encapsulator-time-trial-suit.html

[Fis18] Fisher, S. (2018). *Endura's D2Z Aero Collection texturizes fabrics for improved aerodynamics*. Bikerumor. https://bikerumor.com/enduras-d2z-aero-collection-texturizes-fabrics-for-improved-aerodynamics/

[Mic97] Michaud, J. (1997). *Aerodynamic Fuel Savers*. Airtab. https://www.airtab.com/

[Miro] *Miro | The Visual Workspace for Innovation*. (n.d.). https://miro.com/

[ENE09] ENEAGRID | CRESCO. (2009, January 23). *Spalart-Allmaras Model Theory*. https://www.afs.enea.it/project/neptunius/docs/fluent/html/th/node48.htm

[Chi19] Chicago Architecture Center. *(2019). Discover Design Handbook.* https://discoverdesign.org/handbook

[ART23] Ramon Torrens, Aaron. (November 2023). *Design of the Saeta Velomobile.* https://cad.onshape.com/documents/b9fadd6d8c3c8bb0d59ce54a/w/499259d8691c9c1994b23c49/e/fc632b9a720afab3dfc44cf0?renderMode=0&uiState=65567df07076274882cd0314